DISSERTATION

submitted to the

Combined Faculties for the Natural Sciences and for Mathematics
of the Ruperto-Carola University of Heidelberg, Germany

for the degree of

DOCTOR OF NATURAL SCIENCES

Put forward by

Simon Ralph Hubertus, MSc
born in St. Wendel

Oral examination: 16 October 2019

QUANTITATIVE SUSCEPTIBILITY MAPPING TO MEASURE THE LOCAL TISSUE OXYGENATION

Referees: Prof. Dr. Lothar R. Schad
Prof. Dr. Peter Bachert

Für meinen Papa

ZUSAMMENFASSUNG

Die Magnetresonanztomographie (MRT)-basierte Kartierung der Gewebeoxygenierung wäre für die Behandlung von Patienten mit Hirntumoren äußerst hilfreich. Das Ziel dieser Arbeit war daher die quantitative Suszeptibilitätskartierung (QSM) in die Rekonstruktion des Sauerstoffextraktionsanteils (OEF), des zerebralen Blutflusses (CBF) und der zerebralen Sauerstoffumsatzrate (CMRO2) einzubinden. Im ersten Teil wurde ein kombinierter QSM und quantitativer blutsauerstoffabhängiger (qBOLD) Ansatz für zwei verschiedene MRT Sequenzen, gradientenecho-abgetastetes Spinecho (GESSE) und Multi-Gradientenecho (GRE), in sieben gesunden Probanden und Simulationen verglichen. GESSE ergab eine höhere Parametergenauigkeit in simulierter Grauer Substanz, produzierte aber einen unphysiologischen Kontrast zwischen Grauer und Weißer Substanz im OEF in vivo. GRE ist effizienter und erzeugte homogene OEF Karten in vivo, zeigte aber Ungenauigkeiten in der Simulation. Im zweiten Teil wurde ein künstliches neuronales Netz (ANN) für QSM+qBOLD trainiert und mit dem initialen quasi-Newton (QN) Ansatz verglichen. Das ANN ermöglichte eine schnellere und robustere Rekonstruktion von OEF Karten mit einer geringeren individuellen Variation ($\mathrm{OEF}_{\mathrm{ANN}} = 43.5 \pm 0.8\,\%$ vs $\mathrm{OEF}_{\mathrm{QN}} = 43.8 \pm 5.2\,\%$). Im dritten Teil wurde Clustering, eine Technik aus dem maschinellen Lernen, in den QN-Ansatz der QSM+qBOLD Analyse von GRE Daten integriert und auf acht Patienten mit hochgradigen Gliomen angewendet. Der OEF war innerhalb des Tumors signifikant niedriger als auf der kontralateralen Seite bei Grad III ($\mathrm{OEF}_{\mathrm{tum}} = 12.5 \pm 0.5\,\%$ vs $\mathrm{OEF}_{\mathrm{con}} = 24.5 \pm 2.3\,\%$) und Grad IV ($\mathrm{OEF}_{\mathrm{tum}} = 17.2 \pm 6.1\,\%$ vs $\mathrm{OEF}_{\mathrm{con}} = 24.8 \pm 4.5\,\%$) Gliomen. Der CBF war signifikant höher, allerdings nur bei Grad IV Gliomen ($\mathrm{CBF}_{\mathrm{tum}} = 108.1 \pm 83.3\,\mathrm{ml}/100\,\mathrm{g}/\mathrm{min}$ vs $\mathrm{CBF}_{\mathrm{con}} = 29.1 \pm 21.0\,\mathrm{ml}/100\,\mathrm{g}/\mathrm{min}$). Die CMRO2 zeigte keine signifikanten Unterschiede. Das Nutzen der Phase und Magnitude des gemessenen MRT-Signals und die Einbeziehung maschinellen Lernens für die Rekonstruktion des OEF mittels QSM+qBOLD ist vielversprechend und könnte die Implementierung einer robusten Quantifizierung der Gewebeoxygenierung in der klinischen Routine in Zukunft ermöglichen.

ABSTRACT

Magnetic resonance imaging (MRI)-based mapping of the tissue oxygenation would be highly beneficial for the treatment of patients with brain tumours. Hence, the purpose of this thesis was to incorporate quantitative susceptibility mapping (QSM) into a reconstruction of the oxygen extraction fraction (OEF), cerebral blood flow (CBF) and cerebral metabolic rate of oxygen (CMRO2). In the first part, a joint QSM and quantitative blood oxygenation level-dependent (qBOLD) approach from two different MRI sequences, gradient echo sampling of spin echo (GESSE) and multi-gradient echo (GRE), was compared in seven healthy subjects and simulations. GESSE yielded higher parameter accuracy in simulated grey matter but produced unphysiological grey–white matter contrast in OEF in vivo. GRE is more efficient and generated uniform OEF maps in vivo but revealed biases in simulation. In the second part, an artificial neural network (ANN) was trained for QSM+qBOLD analysis and compared to the initial quasi-Newton (QN) reconstruction. The ANN allowed a faster and more robust reconstruction of OEF maps with lower intersubject variation ($\mathrm{OEF}_{\mathrm{ANN}} = 43.5 \pm 0.8\,\%$ vs $\mathrm{OEF}_{\mathrm{QN}} = 43.8 \pm 5.2\,\%$). In the third part, machine learning-based clustering was incorporated into the QN QSM+qBOLD analysis and applied to eight patients with high-grade gliomas. The OEF was significantly lower inside the tumour compared to the contralateral side in grade III ($\mathrm{OEF}_{\mathrm{tum}} = 12.5 \pm 0.5\,\%$ vs $\mathrm{OEF}_{\mathrm{con}} = 24.5 \pm 2.3\,\%$) and grade IV ($\mathrm{OEF}_{\mathrm{tum}} = 17.2 \pm 6.1\,\%$ vs $\mathrm{OEF}_{\mathrm{con}} = 24.8 \pm 4.5\,\%$) gliomas. The CBF was significantly higher; yet, only in grade IV gliomas ($\mathrm{CBF}_{\mathrm{tum}} = 108.1 \pm 83.3\,\mathrm{ml}/100\,\mathrm{g}/\mathrm{min}$ vs $\mathrm{CBF}_{\mathrm{con}} = 29.1 \pm 21.0\,\mathrm{ml}/100\,\mathrm{g}/\mathrm{min}$). The CMRO2 revealed no significant differences. Exploiting the phase and magnitude of the acquired MRI signal and including machine learning for reconstruction of the OEF with QSM+qBOLD is promising and might facilitate the implementation of a robust quantification of the tissue oxygenation in the clinical routine in the future.

Love and compassion are necessities, not luxuries.
Without them humanity cannot survive.

— Tenzin Gyatso, 14th Dalai Lama

ACKNOWLEDGEMENTS

This work would not have been possible without the help, support and guidance of many people.

First and foremost, I would like to thank Prof. Dr. Lothar Schad for the opportunity to work towards my PhD at his chair, his consistent support and open door policy.

I am also grateful to Prof. Dr. Bachert who acted as referee for this thesis and to Dr. Sebastian Domsch for his supervision at the beginning of my PhD.

Likewise, I want to express my gratitude to Prof. Yi Wang who allowed and helped me to study and work at his Cornell MRI Research Lab. Without my time at Cornell many parts of this work would not exist. In the same breath, I would like to thank Junghun Cho for openly sharing his vast knowledge of QSM and qBOLD with me and helpful discussions, both MRI-related and unrelated, during my stay at New York. This experience abroad was greatly facilitated by the financial support from the German-American Fulbright Commission for which I am deeply thankful.

Furthermore, I gratefully acknowledge the cooperation with our clinical partners at the Medical Faculty Mannheim especially with Dr. Alex Förster and Dr. Bettina Mürle from the Department for Neuroradiology that helped in measuring and assessing one of the glioma patients.

In addition, humble thanks go to Ruomin Hu, Valerie Klein, Irène Brumer and Sebastian Thomas for proofreading this thesis.

Finally, I will forever be indebted to all my colleagues at CKM that took part in my journey over the last 3.5 years. The resulting friendships, the social interactions, the pleasant working atmosphere and the great discussion made my time here unforgettable. In particular, I want to highlight my OEF co-chief Sebastian Thomas. Thank you for the laughs, beers, Scrubs quotes and 21st nights of September we shared. I would like to switch to my native language for the remaining part of these acknowledgements.

Ein großer Dank geht an meine Freunde aus dem Saarland, aus Aachen, London und Mannheim. Ohne euch wäre ich niemals zu der Person geworden, die ich heute bin. Dies gilt natürlich noch viel mehr für meine gesamte Familie, die mir in jeder Lebenssituation den Rücken gestärkt und freigehalten hat. Der größte Dank geht an meine Mama Petra und Schwester Leena, die mich Herzlichkeit und Mitgefühl gelehrt haben und meinen Papa Arno, der mir Selbstlosigkeit vorgelebt hat und bereits lange vor mir wusste, dass ich später in der Medizintechnik landen werde. Zu guter Letzt möchte ich mich bei meiner Freundin Lucia bedanken. Du hast mir bei dieser Arbeit und in den letzten 11 Jahren viel mehr geholfen als du dir vorstellen kannst.

CONTENTS

LIST OF FIGURES

LIST OF TABLES

ACRONYMS

1D	one-dimensional
2D	two-dimensional
3D	three-dimensional
ADC	analogue to digital converter
AIF	arterial input function
ANN	artificial neural network
ASL	arterial spin labelling
BOLD	blood oxygenation level-dependent
CASL	continuous arterial spin labelling
CBF	cerebral blood flow
CBV	cerebral blood volume
CET	contrast-enhancing tumour
cgs	centimetre-gram-second
CMRO2	cerebral metabolic rate of oxygen
CNS	central nervous system
CSF	cerebrospinal fluid
DCE	dynamic contrast enhanced
EPI	echo-planar imaging
FID	free induction decay
fMRI	functional magnetic resonance imaging
FOV	field of view
Gd	gadolinium
GESSE	gradient echo sampling of spin echo
GM	grey matter
GM+WM	combined grey and white matter
GRE	multi-gradient echo

GRAPPA	generalized autocalibrating partial parallel acquisition
Hb	deoxyhaemoglobin
HbO_2	oxyhaemoglobin
Hct	haematocrit
LD	labelling duration
MEDI	morphology enabled dipole inversion
MEDI+0	MEDI with automatic CSF zero reference
MPRAGE	magnetisation-prepared rapid gradient echo
MR	magnetic resonance
MRI	magnetic resonance imaging
MRSE	mean root squared error
MSE	mean squared error
nGM	normal appearing grey matter
NMR	nuclear magnetic resonance
nWM	normal appearing white matter
OED	oedema
OEF	oxygen extraction fraction
PASL	pulsed arterial spin labelling
pCASL	pseudocontinuous arterial spin labelling
PD	proton density
PET	positron emission tomography
PLD	post-labelling delay
ppb	parts per billion
ppm	parts per million
qBOLD	quantitative blood oxygenation level-dependent
QN	quasi-Newton
QSM	quantitative susceptibility mapping
QSM+qBOLD	combined QSM and qBOLD analysis
rCN	relative condition number

RDF	relative difference field
RF	radiofrequency
ROI	region of interest
SE	spin echo
SI	international system of units
SNR	signal to noise ratio
SRF	spatial response function
WHO	World Health Organization
WM	white matter

1 INTRODUCTION

257,000 new cases of cancer in the brain and the central nervous system (CNS) were estimated worldwide in 2012 [Ferlay et al., 2015]. In addition, an expected 187,000 people died from these cancer types in the same year [Ferlay et al., 2015]. With regard to malignant primary brain tumours, glioblastoma multiforme is the most common type comprising around $42-49\,\%$ of new cases each year [Wen and Kesari, 2008]. Due to the aggressive infiltration of the surrounding tissue, the median survival time of glioblastoma patients is only 12 to 15 months [Wen and Kesari, 2008].

Glioblastomas are commonly first surgically resected and subsequently treated with radio- and chemotherapy [Furnari et al., 2007; Buatti et al., 2008]. Due to its strong soft tissue contrast, magnetic resonance imaging (MRI) is the means of choice for imaging brain tumours for diagnosis, treatment planning and assessment of treatment response. Currently, contrast-enhanced T_1-weighted MRI is widely used to assess the morphology of glioblastomas as damages in the blood-brain barrier allow the contrast agent to accumulate inside the tissue. However, this approach is unable to detect tumour infiltration prior to disruption of the blood-brain barrier [Young, 2007].

Functional imaging would be advantageous for this task and the oxygen extraction fraction (OEF) and the cerebral metabolic rate of oxygen (CMRO2) have shown to be promising biomarkers for tissue vitality and viability in numerous diseases, such as stroke [An et al., 2014; Ibaraki et al., 2004], carotid artery stenosis [Kudo et al., 2016], multiple sclerosis [Fan et al., 2014] and obstructive sleep apnea [Rodgers et al., 2016]. Moreover, the knowledge of the tissue oxygenation is highly valuable for radiotherapy treatment of brain tumours since it affects the radiosensitivity of the tissue [Hockel et al., 1996; Vaupel and Mayer, 2007; Rofstad et al., 2000; Wang et al., 2006; Søvik et al., 2009]. Furthermore, tissue oxygenation parameters, such as the OEF, have proven to be even capable of tumour grading [Stadlbauer et al., 2017]. The current gold standard for OEF/CMRO2 measurements is positron emission tomography (PET) with ^{15}O as a tracer. Yet, the half-life of ^{15}O is only around 2 minutes, which renders this method technically demanding and costly as it requires a cyclotron on-site.

MRI-based mapping of the brain oxygenation has been an area of extensive research for over 25 years [Yablonskiy and Haacke, 1994; Christen et al., 2012; Bolar et al., 2011; Zhang et al., 2015]. Several approaches to evaluate the OEF for instance have been proposed over the years, the most prominent being the quantitative blood oxygenation level-dependent (qBOLD) technique [Yablonskiy and Haacke, 1994; Yablonskiy, 1998; He and Yablonskiy, 2007], which models the effects of physiological and oxygenation parameters on the magnitude of the MRI signal. Nevertheless, the qBOLD approach has not yet

been adopted in the clinical routine as the complex tissue model requires an exceedingly high signal to noise ratio (SNR) in order to accurately disentangle its parameters. In 2010, a postprocessing method called quantitative susceptibility mapping (QSM) was proposed [De Rochefort et al., 2010], which reconstructs the magnetic susceptibility from the phase of the MRI signal. Since then, various approaches [Fan et al., 2014; Zhang et al., 2015; Kudo et al., 2016; Zhang et al., 2017, 2018] have been suggested to infer the OEF also from QSM; yet, these methods necessitate some form of vascular challenge [Zhang et al., 2015, 2017], strong physiological approximations [Zhang et al., 2018] or are restricted to large veins [Fan et al., 2014].

Hence, Cho et al. [2018] proposed to combine qBOLD and QSM into one reconstruction, which allows to exploit the full information of the acquired MRI signal, i. e. the magnitude and phase. Moreover, QSM, which shows good repeatability [Feng et al., 2018], can act as an independent measurement to regularise the less robust qBOLD reconstruction. Cho et al. [2018] used a multi-gradient echo (GRE) sequence for their combined approach and applied the qBOLD model of Ulrich and Yablonskiy [2016] for reconstruction. Despite the good performance of the model in grey matter, it was biased in white matter when sampling with short echo times owing to the fast T_2 component associated with myelin [Ulrich and Yablonskiy, 2016; Whittall et al., 1997]. Furthermore, the resulting parameter maps greatly depended on the initial guess of OEF and deoxygenated blood volume ν; thus, requiring a mask of the straight sinus and an additional arterial spin labelling (ASL) acquisition respectively. Lastly, the approach has so far only been tested in healthy volunteers and its performance in pathologies affecting the oxygenation status of the brain is yet unknown.

It is therefore that the overall objective of this thesis was to incorporate QSM into a qBOLD-based reconstruction of the OEF and CMRO2. This method was then optimised with regard to sensitivity and robustness and applied to patients with high-grade gliomas as a first step to facilitate a clinical implementation in the future. This thesis consists of three main parts.

In the first part, the performance of two different MRI sequences for combined QSM and qBOLD analysis (QSM+qBOLD) was compared. The OEF and deoxygenated blood volume ν are strongly coupled in the qBOLD model. Hence, an accurate and precise parameter reconstruction requires the separation of the so-called long-term regime, where the logarithmic signal decays linearly with OEF and the short-term regime, where it decays quadratically. Merely sampling the free induction decay (FID) with GRE restricts the short-term regime to the first few echoes after excitation, making a robust parameter separation difficult [Yablonskiy and Haacke, 1997]. However, including a spin echo (SE) into the acquisition extends the short-term regime to the gradient echoes right before and after the SE; thus, doubling its duration. In addition, it enables longer sampling with echo times between 25 ms and 80 ms so that the fast T_2 component of roughly 15 ms should become negligible [Whittall et al., 1997; Yablonskiy et al., 2013]. For this purpose, Yablonskiy and Haacke [1997] proposed the gradient echo sampling of spin echo (GESSE) sequence

for qBOLD reconstructions in 1997. Here, a method was implemented that uses GESSE data for the qBOLD and GRE data for the QSM reconstruction part and utilises an initial low-resolution data fit instead of a straight sinus mask and ASL acquisition for parameter initialisation. This method was compared to the approach from Cho et al. [2018] solely relying on GRE data with regard to accuracy, precision and robustness to parameter initialisation based on simulations and seven healthy subjects. This study has been published as Hubertus et al. [2019b].

In the second part, an artificial neural network (ANN) was used to perform the QSM+qBOLD analysis. Today, ANNs are widely utilised in various areas of signal processing with a focus on pattern recognition [Bishop, 1995; Nasrabadi, 2007], classification [Lakhani and Sundaram, 2017; Liu et al., 2018; Zöllner et al., 2010] and general image reconstruction problems [Bollmann et al., 2019; Yoon et al., 2018; Hammernik et al., 2018; Schnurr et al., 2019; Maier et al., 2019; Lundervold and Lundervold, 2019]. Nonetheless, they also allow for highly efficient and robust curve-fitting [Bishop and Roach, 1992; Farrell et al., 1992; Hornik, 1991], which has already been exploited in poorly conditioned problems in MRI [Bertleff et al., 2017; Domsch et al., 2018]. Domsch et al. [2018] for example successfully applied an ANN for the first time to fit the qBOLD model to GESSE data. However, the original qBOLD model implemented there neglects the effects of non-blood magnetic susceptibilities. Here, a similar approach to Domsch et al. [2018] was used; yet, QSM was inlcuded into the ANN to obtain a QSM+qBOLD analysis for OEF quantification and it was trained for GRE data. The performance of the ANN was then compared to the original QSM+qBOLD approach [Cho et al., 2018] that utilises traditional quasi-Newton (QN) methods for numerical optimisation. The comparison was done in seven healthy subjects with regard to reconstruction speed and parameter distribution. This study has been published as Hubertus et al. [2019c].

In the third part, QSM+qBOLD analysis was applied to the GRE data of eight patients diagnosed with high-grade gliomas. Machine learning-based clustering was introduced as an intermediate step for the QN least-squares fitting to further increase the robustness of the method. The oxygenation parameters OEF, cerebral blood flow (CBF) and CMRO2 were compared between the tumour and its contralateral side for six glioblastoma and two anaplastic astrocytoma patients. This study has been published as Hubertus et al. [2019a].

2

BASIC PRINCIPLES

This chapter gives a brief overview over the basic theoretical principles, knowledge of which is vital for the understanding of the subsequent work. The topics range from the fundamental process of nuclear magnetic resonance over its application in magnetic resonance imaging to the image postprocessing technique quantitative susceptibility mapping. Moreover, physiological considerations regarding tissue oxygenation and brain tumours are also covered.

2.1 NUCLEAR MAGNETIC RESONANCE

In 1922, Otto Stern and Walther Gerlach discovered a new quantum mechanical property of electrons with their famous Stern-Gerlach experiment. They called the phenomenon *spin* and although it has strong similarities to the angular momentum, it is in fact intrinsic to the particle and has no analogue in classical physics. Therefore, the total angular momentum is the sum of the spin and the orbital angular momentum. A coupling of the electron spin with its orbital angular momentum together with relativistic effects can explain the splitting of energy levels in atoms, which is called the fine structure. In 1891, long before the discovery of Stern and Gerlach, Albert Abraham Michelson detected a further splitting of the atomic spectral lines, which is orders of magnitude smaller. This is referred to as hyperfine structure and was explained only in 1924 by Wolfgang Pauli. He proposed a nuclear spin, which is however three orders of magnitude smaller than that of the electron. Its interaction with the magnetic field of the electrons in the atomic shell is the main contribution to the hyperfine structure. The existence of such a nuclear spin was verified in an experiment by Isidor Isaac Rabi, building on work of Otto Stern, and both were awarded the Nobel Prize in Physics in 1944 and 1943 respectively. Felix Bloch [Bloch, 1946] and Edward Mills Purcell [Purcell et al., 1946] were the first to develop methods to manipulate nuclear spins in solids by resonant absorption of radiofrequency fields and measured the resulting nuclear induction. Both received the Nobel Prize in Physics in 1952 for their work on nuclear magnetic precision measurements and are regarded as the founding fathers of nuclear magnetic resonance (NMR).

The Nobel Prize in Physics 1943*: Otto Stern "for his contribution to the development of the molecular ray method and his discovery of the magnetic moment of the proton".*

The Nobel Prize in Physics 1944*: Isidor Isaac Rabi "for his resonance method for recording the magnetic properties of atomic nuclei".*

The Nobel Prize in Physics 1952 *was awarded jointly to Felix Bloch and Edward Mills Purcell "for their development of new methods for nuclear magnetic precision measurements and discoveries in connection therewith".*

2.1.1 *Nuclear Spin and Magnetic Moment*

Atomic nuclei consist of so-called nucleons, which comprise protons and neutrons. Both particles are fermions with spin quantum number $s = 1/2$. Similar to the atomic shell model, the nuclear shell model approximates the nucleus as an harmonic oscillator with the principal quantum number $n = 1, 2, 3, ...$ denoting discrete energy levels. The corresponding orbital quantum number

Here the hat denotes quantum mechanical operator properties.

is given by $l = n, n-2, ...$ with $l \geq 0$. This means that the total angular momentum of a nucleon is given by the quantum number $j = |l \pm 1/2|$. The total angular momentum of a nucleus $\hat{\vec{I}}$ is obtained by the sum over all nucleons and rather confusingly denoted as nuclear spin.

As an angular momentum operator, $\hat{\vec{I}}$ fulfils the commutator relations

$$\begin{aligned} \left[\hat{I}_i, \hat{I}_j\right] &= \mathrm{i}\hbar\epsilon_{ijk}\hat{I}_k \\ \left[\hat{I}_i, \hat{\vec{I}}^2\right] &= 0 \end{aligned} \tag{2.1}$$

and, therefore, common eigenvectors exist only for $\hat{I}_i$ and $\hat{\vec{I}}^2$. The nuclear spin is a discrete quantity and the eigenvalues of its magnitude and, without loss of generality, its z-component are described by

$$\begin{aligned} \hat{\vec{I}}^2 \left|I, m\right\rangle &= I(I+1)\hbar^2 \left|I, m\right\rangle \\ \hat{I}_z \left|I, m\right\rangle &= m\hbar \left|I, m\right\rangle \end{aligned} \tag{2.2}$$

with the reduced Planck's constant

$$\hbar = \frac{h}{2\pi} = \frac{6.626 \cdot 10^{-34}\,\mathrm{Js}}{2\pi} \tag{2.3}$$

and the nuclear spin quantum number I and magnetic quantum number m. I can be interpreted as the shell of nuclear spin states with m describing the spatial orientation with respect to z

$$\begin{aligned} I &= 0, \frac{1}{2}, 1, \frac{3}{2}, ... \\ m &= -I, -I+1, ..., I-1, I \quad . \end{aligned} \tag{2.4}$$

Without an external magnetic field, the energy of a certain quantum state is defined only by n and I so that each state shows $(2I+1)$-fold degeneration. The nucleus of the hydrogen atom is merely a single proton, i. e. $I = j = s = 1/2$ holds. Hence, $\hat{I}_z$ has two eigenvalues with

$$m = \pm\frac{1}{2} \quad . \tag{2.5}$$

The nuclear spin is always associated with a magnetic moment $\hat{\vec{\mu}}$, which can be expressed as multiples of the nuclear magneton

$$\mu_\mathrm{N} = \frac{e\hbar}{2m_\mathrm{p}} \tag{2.6}$$

with the proton charge $e = 1.602 \cdot 10^{-19}\,\mathrm{C}$ and mass $m_\mathrm{p} = 1.673 \cdot 10^{-27}\,\mathrm{kg}$. Together with the experimentally determined g-factor, the magnetic moment of a nucleus can be calculated as

$$\hat{\vec{\mu}} = \gamma\hat{\vec{I}} = \frac{g\mu_\mathrm{N}}{\hbar}\hat{\vec{I}} \tag{2.7}$$

Table 2.1: Several nuclei present in the human body together with their nuclear spin qauntum number, magnetic moment, gyromagnetic ratio divided by 2π and molar concentration in human grey matter as stated in Haacke et al. [1999].

Nucleus	I	μ/μ_N	γ in MHz/T	c in mol/l
^{1}H	1/2	2.793	42.58	$88 \cdot 10^{0}$
^{23}Na	3/2	2.216	11.27	$80 \cdot 10^{-3}$
^{31}P	1/2	1.131	17.25	$75 \cdot 10^{-3}$
^{17}O	5/2	−1.893	−5.77	$16 \cdot 10^{-3}$
^{19}F	1/2	2.672	40.08	$4 \cdot 10^{-6}$

with the gyromagnetic ratio γ. For protons, the g-factor is

$$g_P = 5.586 \tag{2.8}$$

and, hence, it follows that

$$\gamma = 2\pi \cdot \gamma = 267.513 \cdot 10^6 \,\mathrm{rad/s/T} \quad . \tag{2.9}$$

Table 2.1 lists different nuclei that are present in the human body together with their magnetic properties.

2.1.2 *Zeeman Effect*

It is common nomenclature in NMR and MRI literature to refer to the magnetic flux density $\vec{B}$ as magnetic field. Let us assume there is an external magnetic field that without loss of generality points in z-direction

$$\vec{B}_0 = B_0 \hat{z} \quad . \tag{2.10}$$

$\hat{x}$, $\hat{y}$ and $\hat{z}$ denote the unit vector in each direction and not quantum mechanical operators.

In this case, the energy levels for the nuclear spin states with different m split up and the degeneration is resolved. This phenomenon is called the *Zeeman effect* and is depicted in Figure 2.1. For a proton with $I = 1/2$, the two eigenvectors are denoted spin-up $|1/2, +1/2\rangle = |\uparrow\rangle$, where the spin is 'parallel' to $\vec{B}_0$, and spin-down $|1/2, -1/2\rangle = |\downarrow\rangle$, where the spin is 'anti-parallel' to $\vec{B}_0$. They build an orthonormal basis of the two-dimensional (2D) Hilbert space and

The terms parallel and anti-parallel have to be treated with caution as we will discover later.

$$\begin{aligned}
\hat{\vec{I}}^2 |\uparrow\rangle &= \frac{3}{4}\hbar^2 |\uparrow\rangle \\
\hat{\vec{I}}^2 |\downarrow\rangle &= \frac{3}{4}\hbar^2 |\downarrow\rangle \\
\hat{I}_z |\uparrow\rangle &= \frac{1}{2}\hbar \ |\uparrow\rangle \\
\hat{I}_z |\downarrow\rangle &= -\frac{1}{2}\hbar \ |\downarrow\rangle
\end{aligned} \tag{2.11}$$

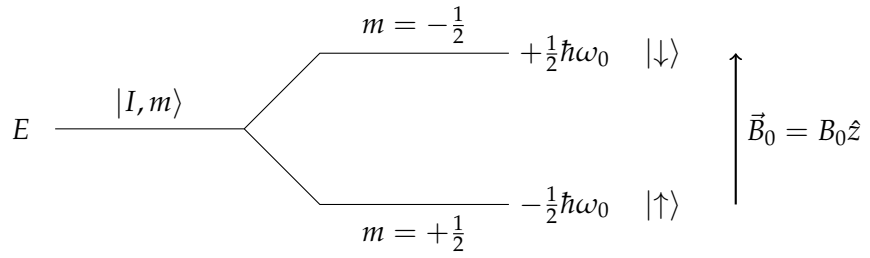

Figure 2.1: Splitting of the Zeeman energy levels for a system with nuclear spin $I = 1/2$ and positive γ, such as a proton, when an external magnetic field $\vec{B}_0 = B_0\hat{z}$ is applied. The state $|\downarrow\rangle$ increases in energy by $\frac{1}{2}\hbar\omega_0$ and the state $|\uparrow\rangle$ decreases in energy by $\frac{1}{2}\hbar\omega_0$. For the former, the spin is 'anti-parallel' and for the latter, it is 'parallel' to $\vec{B}_0$.

are the eigenvalue equations. Using these eigenvectors as a basis, any nuclear spin operator $\hat{\vec{I}}$ can be written in matrix form as

$$\hat{\vec{I}} = \frac{\hbar}{2}\hat{\vec{\sigma}} \tag{2.12}$$

with the Pauli matrices

$$\hat{\sigma}_x = \begin{pmatrix} 0 & 1 \\ 1 & 0 \end{pmatrix}, \quad \hat{\sigma}_y = \begin{pmatrix} 0 & -\mathrm{i} \\ \mathrm{i} & 0 \end{pmatrix}, \quad \hat{\sigma}_z = \begin{pmatrix} 1 & 0 \\ 0 & -1 \end{pmatrix} \quad . \tag{2.13}$$

To calculate the energy of the two states, one has to define the Hamiltonian $\hat{\mathcal{H}}$. The interaction between the nuclear spin of a resting proton and a magnetic field defined by Equation 2.10 can be described by the Hamiltonian

$$\hat{\mathcal{H}} = -\hat{\vec{\mu}} \cdot \vec{B} = -\gamma B_0 \hat{I}_z \quad . \tag{2.14}$$

Since the Hamiltonian is time-independent, the stationary Schrödinger equation

$$\hat{\mathcal{H}} |\psi\rangle = E |\psi\rangle \tag{2.15}$$

can be used to calculate the shifts in energy level $E_\uparrow$ and $E_\downarrow$ of the two nuclear spin states. Inserting Equation 2.14 into 2.15 yields

$$\begin{aligned} E_\uparrow &= -\frac{\hbar}{2}\gamma B_0 \\ E_\downarrow &= +\frac{\hbar}{2}\gamma B_0 \end{aligned} \tag{2.16}$$

and an energy difference of

$$\Delta E = \hbar\gamma B_0 \tag{2.17}$$

for the two states. This means that transitions between the two states are possible by the absorption or transmission of a photon with the so-called Larmor frequency

$$\omega_0 = \gamma B_0 \quad . \tag{2.18}$$

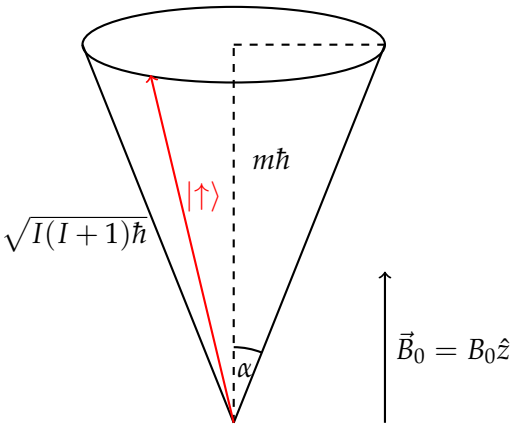

Figure 2.2: Spin-up eigenstate $|\uparrow\rangle$ of the proton nuclear spin operators $\hat{\vec{I}}^2$ and $\hat{I}_z$ with corresponding eigenvalues. Only the squared magnitude and the z-component of $\hat{\vec{I}}$ and not the x- and y-component can be measured sharply at the same time as follows from Equation 2.1. $\alpha = 54.7°$.

Equation 2.18 is called the Larmor equation and describes the basic phenomenon of nuclear magnetic resonance (NMR), which is also the foundation of magnetic resonance imaging (MRI) (see Section 2.2).

2.1.3 *Spin in an External Magnetic Field*

The usual description of 'parallel' and 'anti-parallel' for $|\uparrow\rangle$ and $|\downarrow\rangle$ respectively is actually misleading since, according to Equations 2.11, the eigenstates are tilted by $\alpha \approx 54.7°$ from the z-axis as depicted in Figure 2.2. Moreover, quantum mechanics dictates that the nuclear spin is generally in a superposition of both the spin-up and spin-down state. Hence, it can be represented as

$$|I\rangle = c_\uparrow(t)\,|\uparrow\rangle + c_\downarrow(t)\,|\downarrow\rangle \tag{2.19}$$

with the time-varying probability amplitudes

$$c_{\uparrow,\downarrow}(t) = c_{\uparrow,\downarrow} e^{-iE_{\uparrow,\downarrow}t/\hbar}, \quad c_{\uparrow,\downarrow} \in \mathbb{R}. \tag{2.20}$$

Using this general approach, the expectation values of all three components of the nuclear spin operator can be calculated as

$$\begin{aligned}
\langle \hat{I}_x \rangle &= \frac{\hbar}{2} \langle I|\, \hat{\sigma}_x\, |I\rangle = c_\uparrow c_\downarrow \hbar \cos(\omega_0 t) \\
\langle \hat{I}_y \rangle &= \frac{\hbar}{2} \langle I|\, \hat{\sigma}_y\, |I\rangle = -c_\uparrow c_\downarrow \hbar \sin(\omega_0 t) \\
\langle \hat{I}_z \rangle &= \frac{\hbar}{2} \langle I|\, \hat{\sigma}_z\, |I\rangle = \frac{\hbar}{2}(|c_\uparrow|^2 - |c_\downarrow|^2) \quad .
\end{aligned} \tag{2.21}$$

These expectation values describe a precession of the nuclear spin vector $\hat{\vec{I}}$ about the magnetic field (z-axis) with the Larmor frequency $\omega = \omega_0$. This motion is analogous to a gyroscope precessing about the axis of gravitation.

2.1.4 *Macroscopic Magnetisation*

In NMR one usually deals with imaging volumes in the order of $1\,\mathrm{mm}^3$. For water, such a volume contains approximately $6.68 \cdot 10^{19}$ protons considering a hydrogen nuclei density of 111 M. It is therefore sufficient to consider a macroscopic magnetisation $\vec{M}_0$, defined as the density of all expectation values of the single magnetic moments $\hat{\vec{\mu}}_i$ from N spins inside the unit volume V

$$\vec{M}_0 = \sum_{i=1}^{N} \frac{\langle \hat{\vec{\mu}}_i \rangle}{V} \quad . \tag{2.22}$$

Assuming that the spin system is in thermal equilibrium at temperature T and $\vec{B}_0 = B_0 \hat{z}$, the magnetisation can be described as

$$\vec{M}_0 = \frac{N}{V} \gamma \hbar \sum_{m=-I}^{+I} p_m m \cdot \hat{z} \tag{2.23}$$

with the population probabilities of the Zeeman levels

$$p_m = \frac{1}{Z} \mathrm{e}^{-\frac{E_m}{k_\mathrm{B} T}} \tag{2.24}$$

following a Boltzmann distribution and the state sum

$$Z = \sum_m \mathrm{e}^{-\frac{E_m}{k_\mathrm{B} T}} \quad . \tag{2.25}$$

Here, $k_\mathrm{B} = 1.381 \cdot 10^{-23}\,\mathrm{J/K}$ denotes the Boltzmann constant. For protons, i. e. $I = 1/2$, the ratio of the numbers of spins in the two possible states, parallel $(N_{+1/2})$ and anti-parallel $(N_{-1/2})$, equals

$$\frac{N_{-1/2}}{N_{+1/2}} = \frac{p_{-1/2}}{p_{+1/2}} = \mathrm{e}^{-\frac{1}{2}\frac{\hbar\gamma B_0}{k_\mathrm{B} T}} \cdot \mathrm{e}^{-\frac{1}{2}\frac{\hbar\gamma B_0}{k_\mathrm{B} T}} = \mathrm{e}^{-\frac{\hbar\gamma B_0}{k_\mathrm{B} T}} \quad . \tag{2.26}$$

Considering the human body with a temperature of $T = 310\,\mathrm{K}$ and the commonly used magnetic field strength $B_0 = 3\,\mathrm{T}$, the population ratio is around 0.999997 meaning that the number of spins aligned with the external field exceeds the number of anti-aligned ones only by 3 parts per million (ppm). For the population number difference ΔN, this yields

$$\Delta N = N \tanh\left(\frac{1}{2}\frac{\hbar\gamma B_0}{k_\mathrm{B} T}\right) \tag{2.27}$$

with the total number of states N. From the abovementioned values it follows that $\hbar\gamma B_0 \ll k_\mathrm{B} T$ inside the human body, and therefore the net magnetisation can be approximated as

This is one reason for striving towards higher external magnetic fields in MRI.

$$\vec{M}_0 = \Delta N \cdot \frac{\vec{\mu}}{V} \approx \frac{N\hbar^2\gamma^2}{4Vk_\mathrm{B}} \frac{B_0}{T} \cdot \hat{z} \tag{2.28}$$

using the Taylor expansion of $\tanh(x)$ to the first order. This means that the net magnetisation is approximately proportional to the external magnetic field B_0 and inversely proportional to the temperature T.

2.1.5 *Signal Excitation*

In classical physics, a single magnetic moment $\vec{\mu}$ inside an external magnetic field $\vec{B}_0 = B_0\hat{z}$ experiences a torque that aims at aligning it with $\vec{B}_0$. Its equation of motion can be written as

$$\frac{\mathrm{d}\vec{\mu}}{\mathrm{d}t} = \vec{\mu} \times \gamma\vec{B}_0 \quad . \tag{2.29}$$

It implies that if $\vec{\mu}$ has a component perpendicular to $\vec{B}_0$ (transverse component), $\vec{\mu}$ will start to precess about the axis of the magnetic field (z-axis) with the Larmor frequency $\omega_0 = \gamma B_0$. This is the same motion as predicted by quantum mechanics for a single spin (see Equation 2.21).

However, the net magnetisation $\vec{M}$ from the spin ensemble in thermal equilibrium points only in z-direction with no magnetisation in the x-y-plane. This is due to the fact that the single magnetic moments $\vec{\mu}_i$ have no phase coherence and, thus, their transverse components sum to 0. Hence, to be able to measure any signal from the net magnetisation, $\vec{M}$ has to be tipped away from $\vec{B}_0$. This can be realised by applying radiofrequency (RF) fields perpendicular to the magnetic field axis. To properly understand their impact on the magnetisation, one usually switches to a rotating reference frame denoted with a prime. Generally, if one switches from a resting frame to one that rotates with angular velocity $\vec{\omega}$, the time derivative of a function $\vec{F}$ transforms to

$$\frac{\mathrm{d}\vec{F}}{\mathrm{d}t} = \frac{\partial\vec{F}}{\partial t} + \vec{\omega} \times \vec{F} \quad . \tag{2.30}$$

Applying this to Equation 2.29 yields

$$\begin{aligned} \frac{\partial\vec{M}}{\partial t} &= \vec{M} \times \gamma\left(\vec{B}_0 + \frac{\vec{\omega}}{\gamma}\right) \\ &= \vec{M} \times \gamma\vec{B}_{\mathrm{eff}} \end{aligned} \tag{2.31}$$

where the magnetisation does not precess about $\vec{B}_0$ any longer but rather about an effective magnetic field $\vec{B}_{\mathrm{eff}} = \vec{B}_0 + \vec{\omega}/\gamma$.

Assuming a magnetic field in z-direction $\vec{B}_0 = B_0\hat{z}$ and a left circularly polarised RF field with frequency ω_1 in the x-y-plane

$$\vec{B}_1 = \begin{pmatrix} B_1\cos(\omega_1 t) \\ -B_1\sin(\omega_1 t) \\ 0 \end{pmatrix} \tag{2.32}$$

gives

$$\begin{aligned} \frac{\mathrm{d}\vec{M}}{\mathrm{d}t} &= \vec{M} \times \gamma(\vec{B}_0 + \vec{B}_1) \\ &= \vec{M} \times \gamma(B_1\cos(\omega_1 t)\hat{x} - B_1\sin(\omega_1 t)\hat{y} + B_0\hat{z}) \end{aligned} \tag{2.33}$$

for the magnetisation in the resting frame. Transforming into a frame that rotates with angular velocity $-\omega_1$ around the z-axis yields

$$\frac{\mathrm{d}\vec{M}}{\mathrm{d}t} = \vec{M} \times \gamma \left(B_1 \hat{x}' + \left(B_0 - \frac{\omega_1}{\gamma} \right) \hat{z}' \right) \tag{2.34}$$

$$= \vec{M} \times \gamma \left(B_1 \hat{x}' + \left(B_0 - \frac{\omega_1}{\gamma} \right) \hat{z} \right) \quad . \tag{2.35}$$

According to this equation, the z-component of the total magnetic field will vanish if the RF field $\vec{B}_1$ is applied with the Larmor frequency $\omega_1 = \omega_0$, leaving an effective magnetic field only in $\hat{x}'$. In this case, $\vec{M}$ precesses about the $\hat{x}'$-axis leading to the creation of a measurable transverse magnetisation.

By adapting the RF pulse duration τ and magnitude B_1, the magnetisation can be tipped into the transverse plane with a certain flip angle α. In general, the flip angle can be calculated according to

$$\alpha = \gamma \int_{t}^{t+\tau} B_1(t') \, \mathrm{d}t' \quad . \tag{2.36}$$

However, for rectangular RF pulses and small flip angles, the formula

$$\alpha = \gamma B_1 \tau \tag{2.37}$$

is also commonly utilised.

2.1.6 *Relaxation and Bloch Equation*

When the magnetisation is excited, i. e. tipped away from the z-axis, it can be separated into a longitudinal component M_z and a transverse one $\vec{M}_\perp$. Yet, as soon as the excitation process stops, the magnetisation relaxes back to its original alignment as that represents the state of lowest energy. The main contribution to this relaxation are dipole-dipole interactions between the nuclear spins and the surrounding medium. These interactions can be either between protons and protons or protons and electrons with the latter being more effective due to the stronger magnetic moment of the electron (see Equation 2.51). The actual efficiency of the interaction depends on the relative motion of the nuclear spins and the atoms or molecules of the medium especially on the rotational motion. If the latter rotate or 'tumble' at the frequency ω_{tum}, the local dipolar field associated with them also fluctuates with ω_{tum}. The higher ω_{tum}, the more 'free' a medium is considered (small atoms/molecules, liquids). On the other hand, the lower ω_{tum}, the more 'bound' a medium is considered (large molecules, solids). A detailed explanantion of the physics of relaxation in NMR is given in Bloembergen et al. [1948].

SPIN-LATTICE RELAXATION The relaxation of the longitudinal magnetisation M_z back to its initial value M_0 in thermal equilibrium is owing to the transfer of energy from the spin system to the surrounding medium in form of heat. As the medium was commonly a solid in the early days of NMR, this

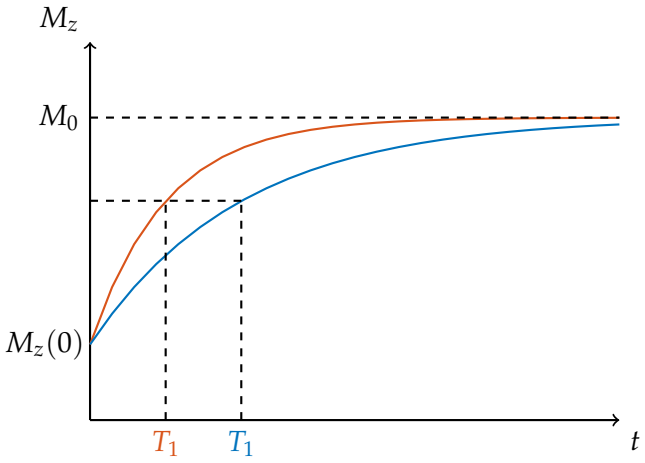

Figure 2.3: Exponential regrowth of longitudinal magnetisation M_z to initial value M_0 as described by Equation 2.39 for two different longitudinal relaxation times T_1.

is usually referred to as spin-lattice relaxation. It can be described by an exponential regrowth and is governed by the longitudinal relaxation time T_1 according to

$$\frac{\mathrm{d}M_z}{\mathrm{d}t} = \frac{1}{T_1} \cdot (M_0 - M_z) \quad . \tag{2.38}$$

A solution of this differential equation is given by

$$M_z(t) = M_z(0) \cdot \mathrm{e}^{-t/T_1} + M_0 \cdot \left(1 - \mathrm{e}^{-t/T_1}\right) \tag{2.39}$$

with the longitudinal magnetisation immediately after the end of the RF pulse $M_z(0)$. An exemplary signal evolution is depicted in Figure 2.3. T_1 depends on the efficiency of the energy transport from the spin system to the lattice and, therefore, differs in various materials and human tissues as can be gathered from Table 2.2. If the tumbling rate ω_{tum} is far away from the Larmor frequency, i. e. off-resonant, the energy transport is inefficient. On the other hand, a resonant ω_{tum} leads to an efficient energy transport. The former would result in a long T_1, the latter in a short T_1. The tumbling rate of freely diffusible water, for example, is much higher than the Larmor frequency usually encountered in MRI. However, restricted water as commonly found in biological tissue, has a lower tumbling rate closer to the Larmor frequency. Moreover, T_1 is affected by the magnetic field strength B_0 as it changes the Larmor frequency of the spins.

SPIN-SPIN RELAXATION The transverse magnetisation $\vec{M}_\perp = M_x\hat{x} + M_y\hat{y}$ also decays with time; yet, this is not due to the energy exchange with the lattice but rather the dipole-dipole interaction among neighbouring spins. Due to random fluctuations in the Brownian motion, each spin observes a slightly different magnetic field and, thus, precession frequency. This in turn leads to an irreversible loss of coherence and, therefore, a dephasing of the spins

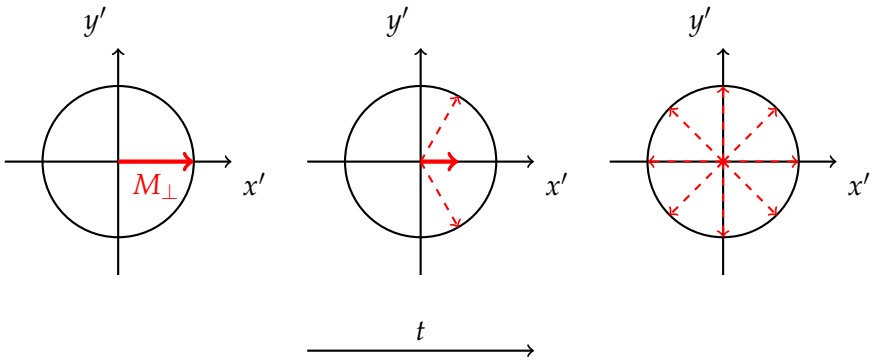

Figure 2.4: Decay of transverse magnetisation $M'_\perp = |\vec{M}'_\perp|$ (thick red arrow) due to dephasing of single spins or magnetic moments (dashed red arrows). The spins lose their coherence because each experiences a slightly different Larmor frequency owing to microscopic inhomogeneities from Brownian motion and dipole-dipole interactions. The dephasing is depicted in the rotating frame of reference.

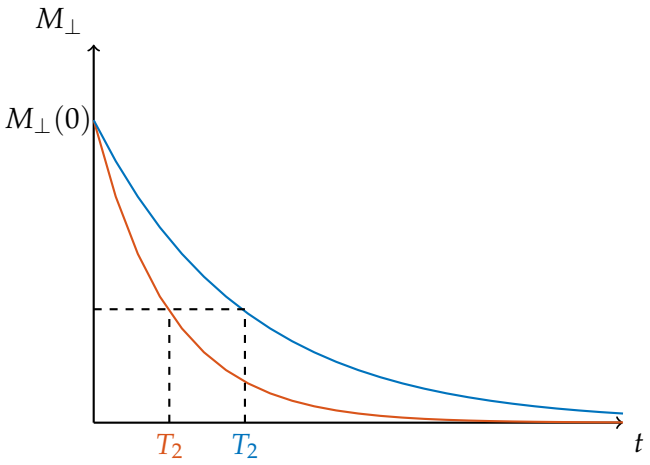

Figure 2.5: Exponential decay of transverse magnetisation $M_\perp = |\vec{M}_\perp|$ as described by Equation 2.41 for two different transverse relaxation times T_2.

(see Figure 2.4). Similar to the spin-lattice relaxation, this phenomenon can be described by an exponential decay of the magnitude of the transverse magnetisation $M_\perp = |\vec{M}_\perp|$ governed by the so-called spin-spin relaxation time T_2. The equation of motion in the rotating reference frame is

$$\frac{\mathrm{d}\vec{M}'_\perp}{\mathrm{d}t} = -\frac{1}{T_2} \cdot \vec{M}'_\perp \tag{2.40}$$

with the solution

$$\vec{M}'_\perp(t) = \vec{M}'_\perp(0) \cdot \mathrm{e}^{-t/T_2} \quad . \tag{2.41}$$

An exemplary signal evolution is depicted in Figure 2.5. With decreasing ω_{tum}, the dipolar field of the medium can be considered more and more static. This means that nuclear spins at different positions accumulate a significantly different phase, i. e. they loose their coherence more rapidly. With increasing

ω_{tum} on the other hand, neighbouring nuclear spins experience the same dipolar field on average. Hence, T_2 in more solid materials is lower than in more liquid media. In contrast to T_1 however, T_2 is approximately independent of B_0 in the range of interest for NMR and MRI. T_1 relaxation automatically reduces the coherence of the transverse magnetisation, i. e. it always entails T_2 relaxation. Yet, T_2 relaxation can also occur independently of T_1 relaxation. Approximate values for T_2 in human tissues are given in Table 2.2

Table 2.2: Approximate longitudinal (T_1) and transverse (T_2) relaxation times of hydrogen in various human tissues at $B_0 = 1.5\,\text{T}$ and body temperature $T = 310\,\text{K}$. Table adopted from Haacke et al. [1999].

Tissue	T_1 in ms	T_2 in ms
Grey matter (GM)	950	100
White matter (WM)	600	80
Cerebrospinal Fluid (CSF)	4500	2200
Fat	250	60
Muscle	900	50
Arterial blood	1200	200
Venous blood	1200	100

RELAXATION TIME T_2^* The spin-spin relaxation time T_2 is an intrinsic property of the tissue. Yet, external inhomogeneities also contribute to the dephasing of the spins and, hence, to the transverse relaxation. It is therefore that the total transverse relaxation time T_2^* was introduced, which is defined as

$$\frac{1}{T_2^*} = \frac{1}{T_2} + \frac{1}{T_2'} \tag{2.42}$$

with the irreversible transverse relaxation time T_2 and the reversible transverse relaxation time T_2'. Using the corresponding relaxation rates yields

$$R_2^* = R_2 + R_2' \quad . \tag{2.43}$$

It is common nomenclature to denote the reversible transverse relaxation rate with a prime. This does not refer to the rotating frame of reference here.

Real-life measurements of the transverse magnetisation in Equation 2.41 will therefore always be governed by T_2^* and are referred to as free induction decay (FID). The impact of T_2' however, can be removed by the utilisation of a so-called spin echo (see Subsection 2.1.8).

BLOCH EQUATIONS Felix Bloch derived the general equation of motion for $\vec{M}$ after excitation in an external magnetic field $\vec{B}$ in 1946. The so-called Bloch equation is valid in homogeneous media and can be written as

$$\frac{\mathrm{d}\vec{M}}{\mathrm{d}t} = \gamma\vec{M} \times \vec{B} + \frac{1}{T_1}(M_0 - M_z)\hat{z} - \frac{1}{T_2}\vec{M}_\perp \tag{2.44}$$

with the three components

$$\begin{aligned}\frac{\mathrm{d}M_x}{\mathrm{d}t} &= \gamma\left(\vec{M}\times\vec{B}\right)_x - \frac{M_x}{T_2}\\ \frac{\mathrm{d}M_y}{\mathrm{d}t} &= \gamma\left(\vec{M}\times\vec{B}\right)_y - \frac{M_y}{T_2}\\ \frac{\mathrm{d}M_z}{\mathrm{d}t} &= \gamma\left(\vec{M}\times\vec{B}\right)_z - \frac{M_0 - M_z}{T_1} \quad .\end{aligned} \tag{2.45}$$

In the case of $\vec{B} = B_0\hat{z}$, Equations 2.45 break down to

$$\begin{aligned}\frac{\mathrm{d}M_x}{\mathrm{d}t} &= \omega_0 M_y - \frac{M_x}{T_2}\\ \frac{\mathrm{d}M_y}{\mathrm{d}t} &= -\omega_0 M_x - \frac{M_y}{T_2}\\ \frac{\mathrm{d}M_z}{\mathrm{d}t} &= \frac{M_0 - M_z}{T_1} \quad .\end{aligned} \tag{2.46}$$

Equation 2.39 is a solution of the z-component. The x- and y-components are usually combined into the complex representation

$$M_+(t) = M_x(t) + \mathrm{i}M_y(t) \tag{2.47}$$

leading to the differential equation

$$\frac{\mathrm{d}M_+}{\mathrm{d}t} = -\left(\mathrm{i}\omega_0 + \frac{1}{T_2}\right)\cdot M_+ \quad . \tag{2.48}$$

The general solution for the complex representation is

$$M_+(t) = M_+(0)\cdot \mathrm{e}^{-\mathrm{i}(\omega_0 t + \varphi_0) - t/T_2} \quad . \tag{2.49}$$

Especially MRI is commonly only concerned with the magnitude of the NMR signal. Hence, M_+ is rewritten as

$$M_+(t) = |M_+(t)|\cdot \mathrm{e}^{\mathrm{i}\varphi(t)} = M_\perp(t)\cdot \mathrm{e}^{\mathrm{i}\varphi(t)} \tag{2.50}$$

with the magnitude

$$M_\perp(t) = M_\perp(0)\cdot \mathrm{e}^{-t/T_2} \tag{2.51}$$

and the phase

$$\varphi(t) = \omega_0 t + \varphi(0) \tag{2.52}$$

in the resting frame of reference.

2.1.7 *Signal Reception*

The net magnetisation $\vec{M}$ in thermal equilibrium points along the external field in z-direction; however, it is orders of magnitude smaller than the external field (see Section 2.3). By tipping $\vec{M}$ into the x-y-plane, it obtains a

transverse component $M_\perp$ that can be easily separated from the external field. Coils placed with their symmetry axis perpendicular to the z-axis can be utilised to measure the precessing transverse magnetisation using Faraday's Law of Induction. This law can be derived from the fundamental Maxwell equations and states that every change of magnetic flux ϕ through a coil with area $\vec{S}$ induces a voltage in the coil according to

$$U_{\text{ind}} = -\frac{\mathrm{d}}{\mathrm{d}t} \int\limits_{S_{\text{coil}}} \vec{B} \cdot \mathrm{d}\,\vec{S} = -\frac{\mathrm{d}\phi}{\mathrm{d}t} \quad . \tag{2.53}$$

To determine the received signal in NMR and MRI, it is convenient to consider the current density $\vec{j}$ defined as

$$\vec{j}(\vec{r}, t) = \vec{\nabla} \times \vec{M}(\vec{r}, t) \quad . \tag{2.54}$$

The vector potential $\vec{A}$ from such a source current and the corresponding magnetic field $\vec{B}$ can be calculated as

$$\vec{A}(\vec{r}) = \frac{\mu_0}{4\pi} \int \frac{\vec{j}(\vec{r})}{|\vec{r} - \vec{r}\,'|} \mathrm{d}^3\,\vec{r}\,' \tag{2.55}$$

The prime does not refer to the rotating frame of reference here but merely denotes the integration variable.

and

$$\vec{B} = \vec{\nabla} \times \vec{A} \tag{2.56}$$

with the vacuum permeability $\mu_0 = 4\pi \times 10^{-7}$. Exploiting Stokes' Theorem gives

$$\phi = \int\limits_{S_{\text{coil}}} \vec{B} \cdot \mathrm{d}\,\vec{S} = \oint \mathrm{d}\,\vec{l} \cdot \vec{A} \tag{2.57}$$

With the help of the vector identity $\vec{A} \cdot (\vec{B} \times \vec{C}) = -(\vec{A} \times \vec{C}) \cdot \vec{B}$, the magnetic flux for a precessing magnetisation $\vec{M}$ can be calculated using integration by parts

$$\begin{aligned}
\phi_M &= \oint \mathrm{d}\,\vec{l} \cdot \left[\frac{\mu_0}{4\pi} \int \mathrm{d}^3\,\vec{r}\,' \frac{\vec{\nabla}' \times \vec{M}(\vec{r}\,')}{|\vec{r} - \vec{r}\,'|} \right] \\
&= \frac{\mu_0}{4\pi} \int \mathrm{d}^3\,\vec{r}\,' \oint \mathrm{d}\,\vec{l} \cdot \left[\left(-\vec{\nabla}' \frac{1}{|\vec{r} - \vec{r}\,'|} \right) \times \vec{M}(\vec{r}\,') \right] \\
&= \frac{\mu_0}{4\pi} \int \mathrm{d}^3\,\vec{r}\,' \vec{M}(\vec{r}\,') \cdot \left[\vec{\nabla}' \times \left(\oint \frac{\mathrm{d}\,\vec{l}}{|\vec{r} - \vec{r}\,'|} \right) \right] \\
&= \int \mathrm{d}^3\,\vec{r}\,' \vec{M}(\vec{r}\,') \cdot \vec{B}^-(\vec{r}\,') \quad .
\end{aligned} \tag{2.58}$$

Here, $\vec{B}^-(\vec{r})$ is the receive field of the coil at position $\vec{r}$, which according to the Law of Reciprocity corresponds to the magnetic field per unit current I created by the coil at this position

$$\vec{B}^-(\vec{r}) = \frac{\vec{B}(\vec{r})}{I} = \vec{\nabla} \times \left(\frac{\mu_0}{4\pi} \oint \frac{\mathrm{d}\,\vec{l}}{|\vec{r} - \vec{r}\,'|} \right) \quad . \tag{2.59}$$

The voltage induced into the coil from the precessing magnetisation inside the sample is

$$U_{\text{ind}}(t) = -\frac{\mathrm{d}}{\mathrm{d}t} \int\limits_{\text{sample}} \mathrm{d}^3\,\vec{r}\,'\vec{M}(\vec{r}\,',t) \cdot \vec{B}^{-}(\vec{r}\,') \quad . \tag{2.60}$$

As only the transverse magnetisation is of interest, the reception coils are placed with their normal perpendicular to the main magnetic field so that $\vec{B}^{-} \approx \vec{B}^{-}_{\perp}$. Two coupled orthogonal coils with a set 90° phase shift are utilised to receive a complex magnetic resonance (MR) signal (Equation 2.51 and 2.52). The signal is then demodulated with a reference sine and cosine signal oscillating at the Larmor frequency. The amplitude of the transverse magnetisation at $t = 0$ is proportional to the spin density $\rho(\vec{r})$ and the initial signal phase $\varphi(0)$ is usually set to 0. This gives

$$S(t) = S_0 \cdot \int\limits_{V} \rho(\vec{r}\,')\mathrm{d}\vec{r}\,' \cdot \mathrm{e}^{-\mathrm{i}\gamma B_0 t} \cdot \mathrm{e}^{-\frac{t}{T_2}} \tag{2.61}$$

for the received NMR signal in a sample volume V. Here, S_0 is the factor of proportionality between the spin density and the received signal. Equation 2.61 is the basic equation for signal reception in NMR and MRI and can be used to determine the effects of inhomogeneities in B_0 for instance.

2.1.8 *Spin Echo*

As mentioned in Subsection 2.1.6, the transverse magnetisation decays in the FID with the time constant T_2^*. The reversible component of the transverse signal decay has to be removed in order to obtain a tissue specific signal. This can be achieved by applying an additional 180° RF pulse between the excitation pulse and signal acquisition. Such a pulse is called refocusing pulse. When applying the refocusing pulse at $t = \mathrm{TE}/2$ after the excitation along an arbitrary axis in the x-y-plane, the single dephased spins are mirrored at this axis and, thus, will be in phase again at the echo time TE. Refocusing the single spins with such a pulse is termed *spin echo*. The behaviour of the magnetisation and the corresponding received NMR signal is depicted in Figure 2.6 and Figure 2.7 respectively.

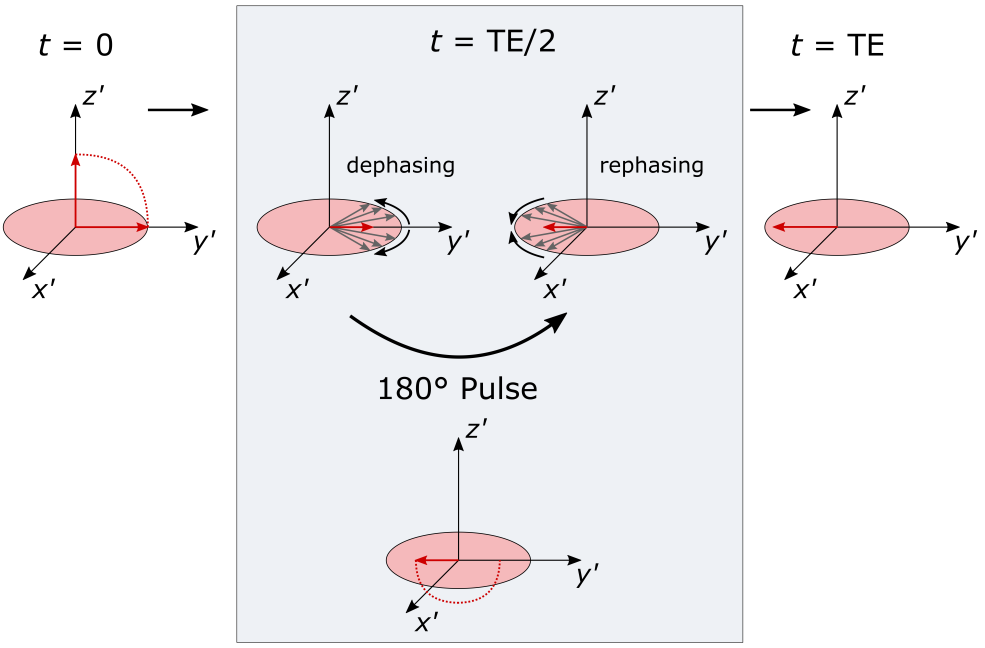

Figure 2.6: Behaviour of the net magnetisation (red arrow) with dephasing and rephasing around 180° refocusing RF pulse applied along the x'-axis. Spin echo, i.e. perfect rephasing of single spins, occurs at the echo time TE if the refocusing pulse is applied at TE/2. The phenomenon is shown in the rotating frame of reference without spin-lattice relaxation for simplicity.

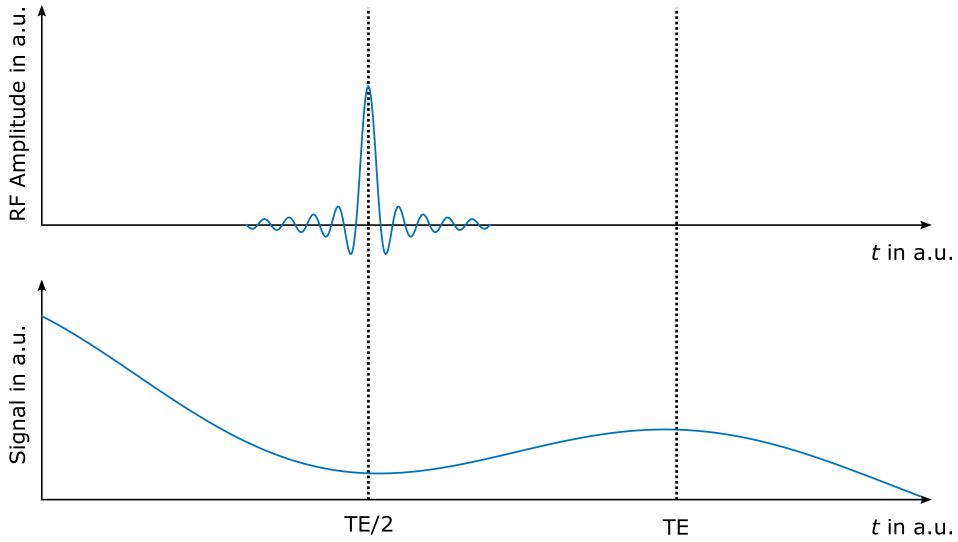

Figure 2.7: RF pulse and signal decay for spin echo creation. 180° refocusing RF pulse at $t = \mathrm{TE}/2$ creates spin echo at echo time TE. Excitation pulse at $t = 0$ is not plotted.

2.2 MAGNETIC RESONANCE IMAGING

It took several decades until it was appreciated that the NMR phenomenon could have a medical application with tremendous impact. In 1971 the physician Raymond V. Damadian was the first person to realise that healthy and cancer cells had different relaxation times. With this in mind, he built the first MR scanner and even took a whole body image in 1977. He achieved spatial localisation by using a saddle-shaped magnetic field that was resonant only at one voxel and by manually moving the subject within the scanner. Such a single point imaging technique was, however, too slow for any clinical application. To overcome this issue, the chemist Paul C. Lauterbur and the physicist Sir Peter Mansfield both came up with schemes to accelerate the signal acquisition for the now called magnetic resonance imaging (MRI) in 1973. Lauterbur applied a magnetic field gradient to measure several one-dimensional (1D) NMR signal projections and back-projected them to a 2D tomographic image. Mansfield on the other hand proposed a linear magnetic field gradient during excitation in order to excite the signal on a slice-by-slice basis and further refined his approach to a line-scan technique in 1977. This line-scan method is already very similar to today's standard spatial encoding in MRI, which will be covered in detail in Subsection 2.2.1. Both Paul C. Lauterbur and Sir Peter Mansfield received the Nobel Prize in Physiology or Medicine in 2003; yet, Raymond V. Damadian was not honoured.

The Nobel Prize in Physiology or Medicine 2003*: Paul C. Lauterbur and Sir Peter Mansfield "for their discoveries concerning magnetic resonance imaging"*

2.2.1 *Spatial Encoding and k-Space*

To create an MR image, the NMR signal has to be localised in space. This process is called spatial encoding and is enabled by additional magnetic field gradients. According to Equation 2.18, the precession frequency ω of the magnetisation depends linearly on the external magnetic field $\vec{B} = B_0\hat{z}$. Hence, by superimposing a linear magnetic field gradient

$$\vec{G} = \left(\frac{\partial B_0}{\partial x}, \frac{\partial B_0}{\partial y}, \frac{\partial B_0}{\partial z}\right) = (G_x, G_y, G_z) \tag{2.62}$$

the precession frequency becomes spatially dependent

$$\omega(\vec{r}) = \gamma B(\vec{r}) = \gamma(B_0 + \vec{G} \cdot \vec{r}) \quad . \tag{2.63}$$

By applying Fourier analysis to the acquired NMR signal, the spatial information encoded in the frequency can be reconstructed. In 2D MRI three spatial encoding steps are distinguished. They are called slice selection, frequency encoding and phase encoding and each is applied in one spatial direction.

SLICE SELECTION For *slice selection*, a gradient in z-direction G_z is applied at the same time as the excitation RF pulse. This makes the precession frequency dependent on the position in z

$$w(z) = \gamma(B_0 + G_z \cdot z) \tag{2.64}$$

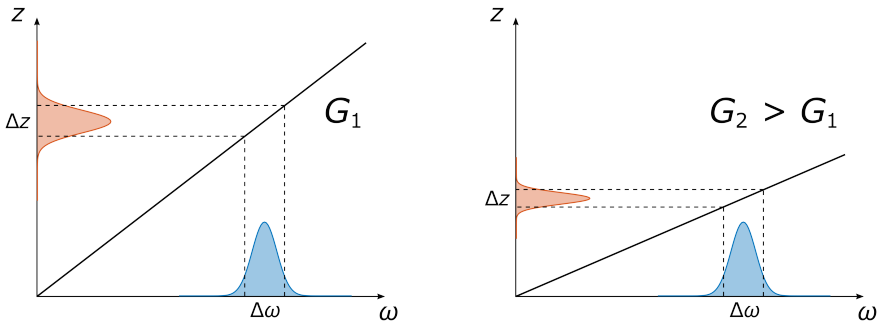

Figure 2.8: Interplay of excitation bandwidth $\Delta\omega$, gradient in z-direction G_z and thickness of excited slice Δz. The larger G_z, the thinner Δz for a given $\Delta\omega$.

and thus leaves only the magnetisation at a certain z at the resonant frequency. If the RF pulse was of infinite length, i. e. contained a single frequency, only an infinitesimally thin slice exactly at the resonance would be excited. However, every excitation pulse has a certain bandwidth $\Delta\omega$ due to its finite length. Hence, the excitation takes place in a slice with thickness

$$\Delta z = \frac{\Delta\omega}{\gamma G_z} \quad . \tag{2.65}$$

This process and the effect of G_z on the slice thickness is schematically illustrated in Figure 2.8.

The exact slice profile depends on the frequency distribution $P(\omega)$ of the RF pulse, which can be easily calculated from the temporal excitation signal via the Fourier transform. A sinc pulse is commonly applied in order to excite a rectangular slice. Owing to time constraints the sinc pulse is, however, cut off after several side lobes; thus, creating only imperfect slice profiles. The resulting slice profile for two distinct sinc pulse lengths is depicted in Figure 2.9. If the application of G_z is centred around the RF pulse and if one assumes that the magnetisation is flipped instantaneously at the RF peak, then the resulting transverse magnetisation is dephasing due to the second half of G_z. For a gradient duration τ, the gradient moment

$$M_G = \int_{t+\frac{\tau}{2}}^{t+\tau} G_z(t')\,\mathrm{d}t' \tag{2.66}$$

therefore induces a distinct phase $\varphi = \gamma \cdot M_G \cdot z$ that depends on the position z within the slice. Hence, a so-called rephasing gradient lobe is usually applied directly after the slice selection gradient with the same gradient strength G_z but in opposite direction and with only half the duration. This leaves the magnetisation within the whole slice in phase. If the gradient in z is omitted during the excitation, the magnetisation is excited independent of the position. This approach is called global excitation and is particularly applied in three-dimensional (3D) MRI.

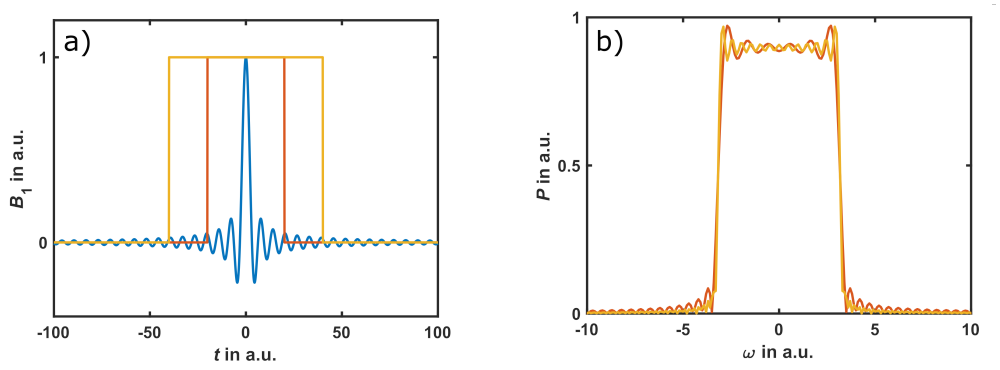

Figure 2.9: Sinc-shaped RF pulse (a) with corresponding frequency distribution $P(\omega)$ (b). Two different durations of the RF pulse are used to calculate the frequency profile with the Fourier transform. One was cut off after three (orange), the other one after six lobes (yellow).

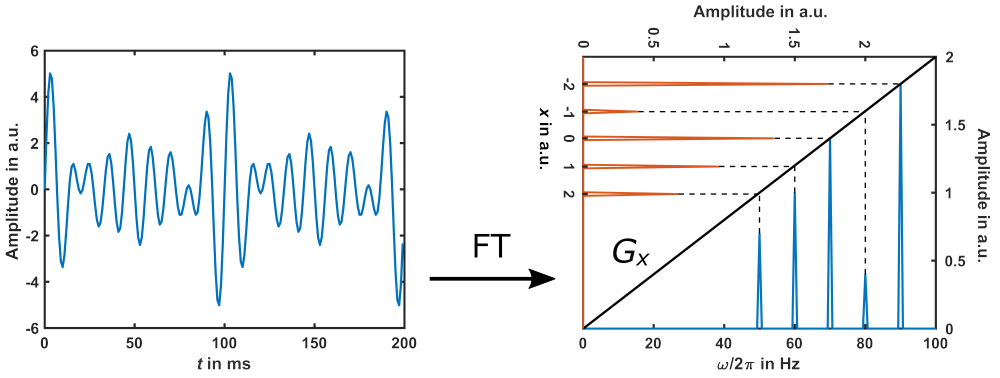

Figure 2.10: Schematic frequency encoding. Superimposed time signal from five different frequencies (left) together with corresponding Fourier transform (FT). The Fourier transform reconstructs the amplitudes of the single frequency components, which can then be located on the x-axis according to Equation 2.67.

FREQUENCY ENCODING The slice selection reduces the spatial encoding to a 2D problem. The NMR signal in one dimension can be easily localised by again applying a linear magnetic field gradient, e. g. G_x in x-direction, but this time during the readout of the signal. This makes the precession frequency of the magnetisation dependent on the spatial position x according to

$$\omega(x) = \gamma(B_0 + G_x \cdot x) \quad . \tag{2.67}$$

Hence, the received signal is a combination of single signals with different frequencies. By applying a 1D Fourier transform, the amplitudes of each signal frequency can be recovered. These frequency amplitudes can then be assigned to the positions along the x-axis where they originated from according to Equation 2.67 (Figure 2.10). It is therefore that this localisation is called *frequency encoding*. When the gradient G_x is applied for a time τ_x, the transverse

magnetisation acquires an additional time-dependent phase and thus the received MR signal can be calculated via

$$S(t, G_x) = S(t) \int \mathrm{e}^{-\mathrm{i}\gamma \int_0^t G_x(t')x\mathrm{d}t'} \mathrm{d}x \tag{2.68}$$

with $S(t)$ given by Equation 2.61.

PHASE ENCODING Even with frequency encoding along the x-axis, the detected signal amplitude is still only a projection along the y-axis. However, simultaneous frequency encoding in x- and y-direction is not possible as the received signal will always be only a projection perpendicular to the total applied gradient. Hence, the magnetisation along the y-axis has to be encoded before the actual readout of the signal. This is achieved by applying a gradient G_y in y-direction for a duration τ_y between signal excitation and reception. During that time the magnetisation along y precesses at different frequencies, resulting in a distinct phase at the signal readout, which depends on the y-position. This means that the acquired signal is a superposition of separate signals along y that have the same frequency but not phase. If this step is repeated N times while G_y is incremented from $-G_{y,\max}$ to $G_{y,\max}$, there are N signal measurements, each consisting of a different superposition of single signals with different phases along the y-axis. The position in y of N signal amplitudes can then be calculated from this set of linear equations. Analogous to Equation 2.68, the received NMR signal can be expressed as

$$S(t, \tau_y, G_y) = S(t) \int \mathrm{e}^{-\mathrm{i}\gamma \int_0^{\tau_y} G_y(t')y\mathrm{d}t'} \mathrm{d}y \quad . \tag{2.69}$$

Despite the similarity of Equation 2.68 and 2.69, this approach for spatial localisation is referred to as *phase encoding* since the frequencies along the y-axis are all the same during readout. This is also why the phase has no explicit time dependency.

In 3D MRI no slice selection is performed but rather phase encoding is applied both in y- and z-direction.

K-SPACE Assuming a rephased excited slice of thickness Δz and neglecting relaxation effects in Equation 2.68 and 2.69, the total received signal in 2D MRI (compare to Equation 2.61) can be written as

$$S(t, \vec{G}) = S_0 \int \int \rho(x, y) \mathrm{e}^{-\mathrm{i}\gamma \left(\int_0^t G_x(t')x\mathrm{d}t' + \int_0^t G_y(t')y\mathrm{d}t' \right)} \mathrm{d}x\mathrm{d}y \quad . \tag{2.70}$$

The integrals in the exponent correspond to a wave number k, which can be defined according to

$$\begin{aligned} k_x &= \frac{\gamma}{2\pi} \int_0^t G_x(t')\mathrm{d}t' \\ k_y &= \frac{\gamma}{2\pi} \int_0^t G_y(t')\mathrm{d}t' \quad . \end{aligned} \tag{2.71}$$

This simplifies Equation 2.70 to

$$\begin{aligned} S(\vec{k}) &= S_0 \int\int \rho(x,y) \mathrm{e}^{-\mathrm{i}\left(2\pi k_x \cdot x + 2\pi k_y \cdot y\right)} \mathrm{d}x\mathrm{d}y \\ &= S_0 \int \rho(\vec{r}) \mathrm{e}^{-2\pi \mathrm{i} \vec{k} \cdot \vec{r}} \mathrm{d}^2\vec{r} \\ &= S_0 \cdot (\mathcal{F}\rho)(\vec{r}) \end{aligned} \tag{2.72}$$

with the Fourier transform $\mathcal{F}$ and an implicit time dependence of the signal $S(\vec{k}) = S(\vec{k}(t))$. Equation 2.72 can be interpreted as sampling spatial frequencies $\vec{k}$ in Fourier space, which is usually referred to as *k-space* in MRI. By changing the gradient moment (Equation 2.66), different wave numbers can be reached, i. e. different points in k-space can be sampled. The actual transverse magnetisation, i. e. the complex MR image, can be retrieved from $S(\vec{k})$ by applying an inverse Fourier transform

$$M_\perp(\vec{r}) = S_0 \cdot \rho(\vec{r}) = \int S(\vec{k}) \mathrm{e}^{2\pi \mathrm{i} \vec{k} \cdot \vec{r}} \mathrm{d}^2\vec{k} \quad . \tag{2.73}$$

In practice, $S(\vec{k})$ is measured discretely for different $\vec{k}$ by adapting the gradient moments and RF pulses in order to follow a certain k-space trajectory. So-called sequence diagrams can be used to visualise and facilitate the understanding of these trajectories with three examples being presented in Subsection 2.2.3 (Figure 2.13, 2.14 and 2.15). The effects of the discrete signal sampling on the resulting image parameters will be covered in the following Subsection 2.2.2.

2.2.2 *Discrete Data Sampling and Image Parameters*

In Equation 2.72 and 2.73, it is assumed that the signal is sampled continuously throughout the whole k-space; however, this is not feasible in practice. The most common sampling technique is Cartesian with k-space increments Δk_x in frequency encoding and Δk_y in phase encoding direction. For frequency encoding, a constant gradient G_x is applied for a time t_x and only N_x data points with a time increment of $\Delta t_x = \frac{t_x}{N_x}$ are sampled by an analogue to digital converter (ADC). For phase encoding, the gradient is applied for a constant time t_y but with varying amplitude from $-G_{y,\max}$ to $G_{y,\max}$ in N_y steps of increment $\Delta G_y = \frac{2G_{y,\max}}{N_y}$. This yields

$$\Delta k_x = \frac{\gamma}{2\pi} G_x \Delta t_x \tag{2.74}$$

$$\Delta k_y = \frac{\gamma}{2\pi} \Delta G_y t_y \quad . \tag{2.75}$$

To take into account the discrete sampling of k-space and to study the resulting effects on the image parameters, one can multiply the k-space signal $S(\vec{k})$ with a 2D sampling function, the so-called Dirac comb or Shah function III, which is defined as

$${}^1\mathrm{III}_{\Delta k_x}(k_x) = \sum_{l=-\infty}^{\infty} \delta(k_x - l\Delta k_x) \tag{2.76}$$

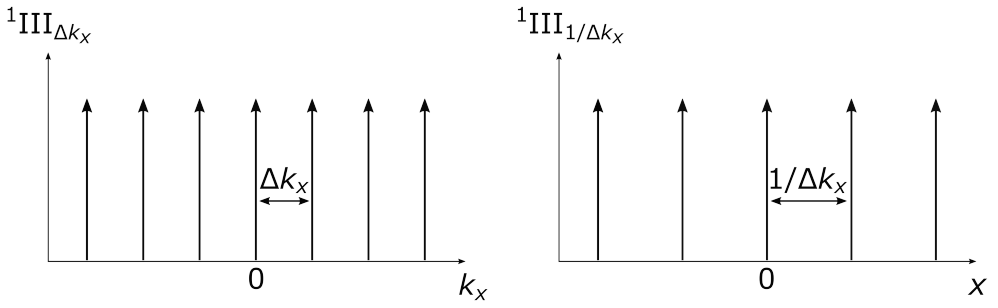

Figure 2.11: One-dimensional Dirac comb or Shah function in k-space (left) and spatial domain (right) representing discrete and equally distributed sampling using delta distributions.

in 1D and as

$$^2\mathrm{III}_{\Delta k_{x,y}}(k_x, k_y) = {}^1\mathrm{III}_{\Delta k_x}(k_x) \cdot {}^1\mathrm{III}_{\Delta k_y}(k_y) \tag{2.77}$$

in 2D. This function represents the discrete sampling in k-space by a sequence of Dirac delta distributions with distance Δk and a schematic drawing of the 1D case is depicted in Figure 2.11. For simplicity, it is still assumed that an infinite amount of samples is acquired. The discretely sampled signal in k-space can thus be written as

$$S_\mathrm{s}(\vec{k}) = S(\vec{k}) \cdot {}^2\mathrm{III}_{\Delta k_{x,y}}(k_x, k_y) \tag{2.78}$$

According to the convolution theorem, the multiplication of $S(\vec{k})$ and $^2\mathrm{III}(\vec{k})$ in k-space leads to a convolution $(*)$ of the inverse Fourier transforms in image space. The inverse Fourier transform of III in 1D is also given by a Dirac delta comb

$$\begin{aligned}\left(\mathcal{F}^{-1}\,{}^1\mathrm{III}_{\Delta k_x}\right)(x) &= \frac{1}{\Delta k_x}\,{}^1\mathrm{III}_{\frac{1}{\Delta k_x}}(x) \\ &= \frac{1}{\Delta k_x}\sum_{m=-\infty}^{\infty}\delta\left(x - \frac{m}{\Delta k_x}\right) \quad .\end{aligned} \tag{2.79}$$

Hence, the resulting transverse magnetisation in image space is calculated according to

$$\begin{aligned}M_\perp^\mathrm{s}(\vec{r}) &= \left(\mathcal{F}^{-1}S_\mathrm{s}\right)(\vec{r}) \\ &= \left(\mathcal{F}^{-1}S\right)(\vec{r}) * \left(\mathcal{F}^{-1}\,{}^2\mathrm{III}_{\Delta k_{x,y}}\right)(\vec{r}) \\ &= M_\perp(\vec{r}) * \frac{1}{\Delta k_x}\sum_{m=-\infty}^{\infty}\delta\left(x - \frac{m}{\Delta k_x}\right) * \frac{1}{\Delta k_y}\sum_{n=-\infty}^{\infty}\delta\left(y - \frac{n}{\Delta k_y}\right) \\ &= \frac{1}{\Delta k_x \Delta k_y}\sum_{m,n=-\infty}^{\infty} M_\perp\left(\frac{m}{\Delta k_x}, \frac{n}{\Delta k_y}\right) \quad .\end{aligned} \tag{2.80}$$

According to Equation 2.78, all sampled spatial frequencies are integer multiples of the k-space increments Δk_x and Δk_y. This means, however, that the

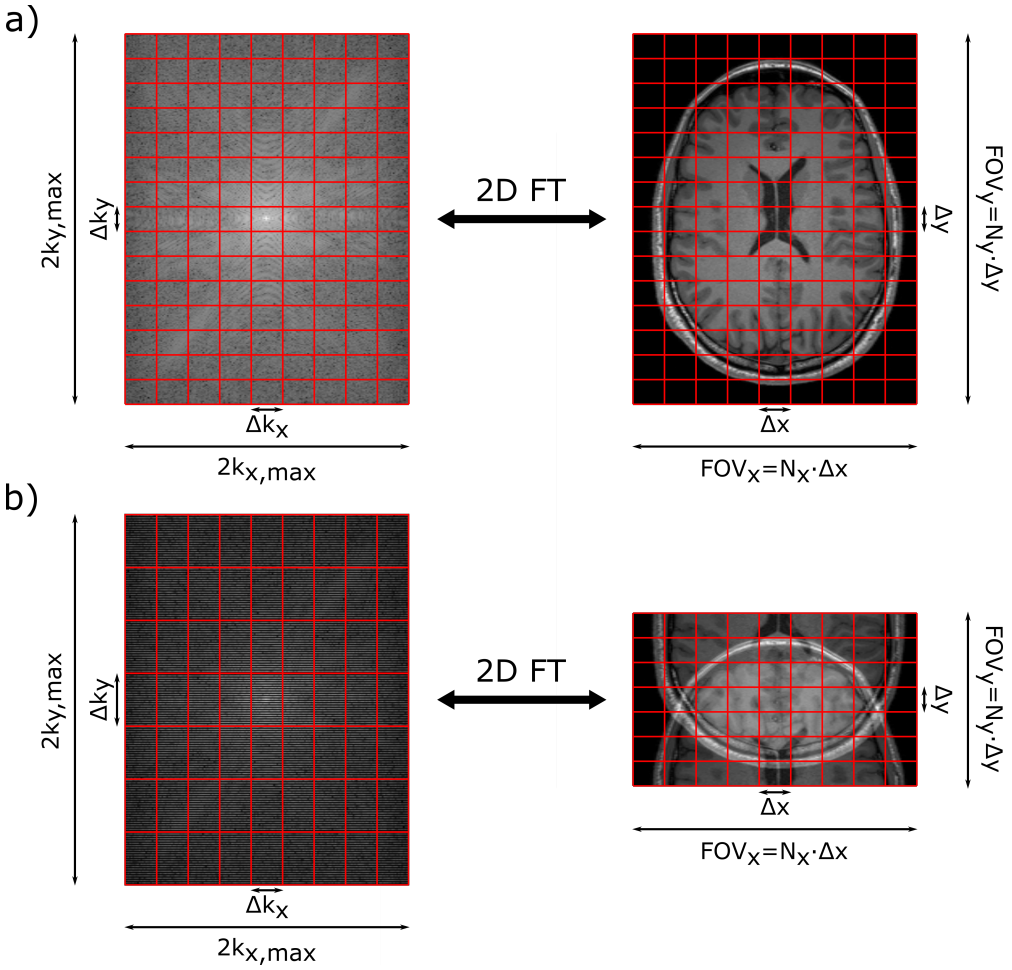

Figure 2.12: Discrete k-space sampling (left) and corresponding image (right) connected by a discrete Fourier transform (FT) (a). Larger increments Δk in phase encoding direction lead to a smaller field of view (FOV), which can result in wrapping artefacts (b). The resolution is defined by the maximum k reached and thus the same in both cases.

signal in image space will be periodic with $\frac{1}{\Delta k}$. Hence, the so-called field of view (FOV) is defined as

$$\mathrm{FOV}_x = \frac{1}{\Delta k_x} \tag{2.81}$$

$$\mathrm{FOV}_y = \frac{1}{\Delta k_y} \quad . \tag{2.82}$$

The increments in k-space have to be chosen such that the resulting FOV covers the whole object. Parts of the object that are outside the FOV will wrap back into the opposite side otherwise (Figure 2.12) due to the periodicity. This artefact is known as *aliasing*. Owing to the properties of the discrete Fourier transform, the signal in image space also consists of $N_x \times N_y$ pixels. The

distance between the pixels and thus the in-plane spatial resolution of the MR image can be calculated as

$$\Delta x = \frac{\mathrm{FOV}_x}{N_x} = \frac{1}{\gamma G_x \Delta t_x N_x} \tag{2.83}$$

$$\Delta y = \frac{\mathrm{FOV}_y}{N_y} = \frac{1}{\gamma \Delta G_y t_y N_y} \quad . \tag{2.84}$$

Increasing the gradient strength or duration while keeping the number of sample points constant will increase the resolution in frequency encoding direction by decreasing the FOV. The same holds true for the gradient increments and duration in phase encoding direction. Taking into account Equations 2.74, 2.75 and 2.81, 2.82, one can determine the sampling requirements

$$\Delta t_x \leq \frac{1}{\gamma G_x N_x \Delta x} \tag{2.85}$$

$$\Delta G_y \leq \frac{1}{\gamma t_y N_y \Delta y} \quad . \tag{2.86}$$

Equation 2.85 and 2.86 represent the Nyquist sampling theorem for MRI stating that the frequency of the signal sampling must be at least twice the maximum occurring frequency in order to be able to exactly reconstruct the signal.

Another important image parameter in MRI is the so-called signal to noise ratio (SNR). It is commonly defined as the ratio of the mean signal within a voxel containing tissue and the standard deviation of the signal within a voxel containing no tissue and thus only noise. Sufficient SNR in an MR image is mandatory for further processing and in order to draw any medical conclusion from it. The SNR can be increased for instance by either acquiring N_{acq} single acquisitions and averaging them or by increasing the voxel size $V = \Delta x \cdot \Delta y \cdot \Delta z$

$$\mathrm{SNR} \propto \sqrt{N_{\mathrm{acq}}} \cdot V \quad . \tag{2.87}$$

2.2.3 *Imaging Sequences*

SPIN ECHO SEQUENCES The sequence diagram of a 2D spin echo sequence together with the corresponding k-space trajectory is depicted in Figure 2.13. After the slice selective excitation using a 90° RF pulse and a concurrent slice selection gradient in z-direction (I), the transverse signal is in phase and, thus, in the centre of k-space. It can be approximated that the spins flip instantaneously in the middle of the RF pulse leading to a dephasing of spins along the z-direction inside the excited slice in the second half of the slice selection gradient. An additional gradient in z-direction with the opposite sign and half the moment of the slice selection gradient is sufficient to rephase theses spins again. After that, a positive dephasing gradient in x and a positive phase encoding gradient in y-direction are applied moving to the upper right corner of k-space (II). A 180° refocusing RF pulse that is simultaneously

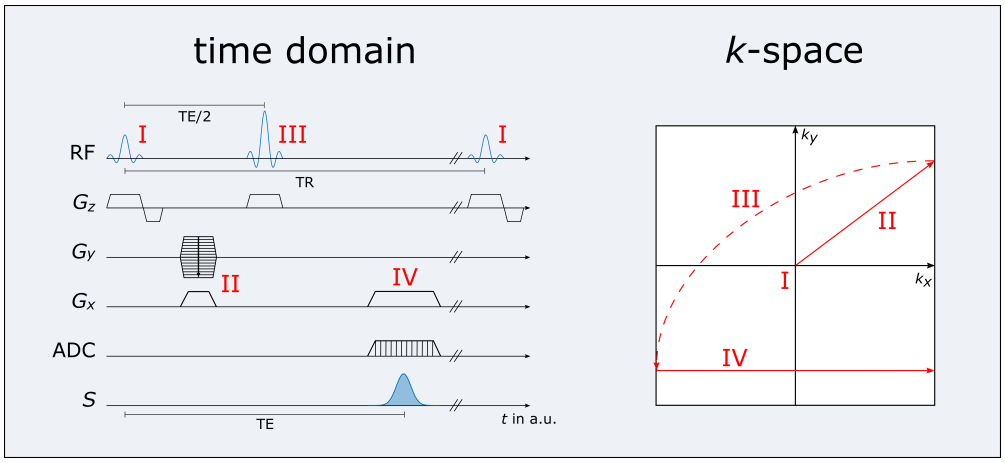

Figure 2.13: 2D spin echo sequence diagram and k-space trajectory.

applied with yet another slice selective gradient at $t = \mathrm{TE}/2$ flips the magnetisation inside the excited slice yielding a reflection at the centre of k-space (III). No rephasing gradient in z-direction is necessary in this case as the 180° flip in the middle of the RF pulse has the same effect as changing the sign of the slice selective gradient. A positive readout gradient in x-direction together with the actual readout by an ADC with its centre at $t = \mathrm{TE}$ leads to the sampling of the spin echo by acquiring a full line in k-space (IV). After the so-called repetition time TR, the whole process is repeated with a reduced phase encoding gradient in y-direction until the desired amount of k-space is sampled.

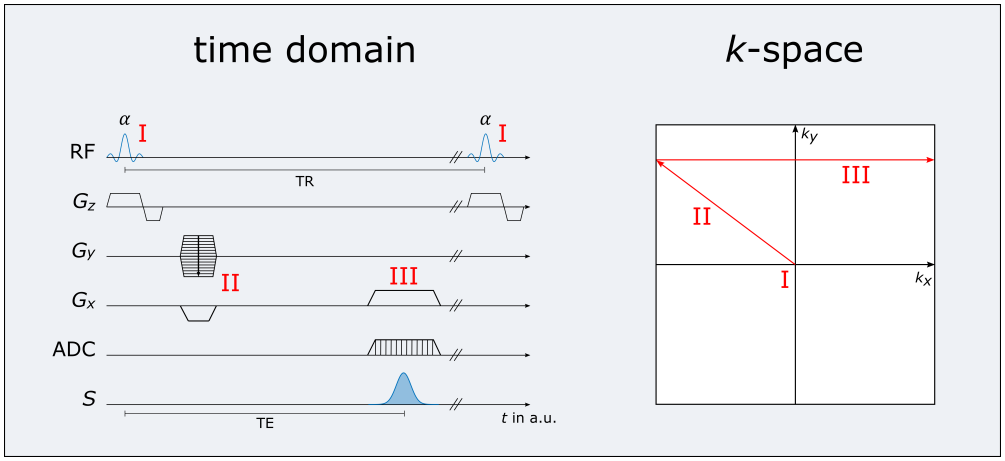

Figure 2.14: 2D gradient echo sequence diagram and k-space trajectory.

GRADIENT ECHO SEQUENCES The sequence diagram of a 2D gradient echo sequence together with the corresponding k-space trajectory is illustrated in Figure 2.14. In contrast to a spin echo sequence, the magnetisation is initially flipped by an angle $\alpha \leq 90°$ and the dephasing gradient in x is applied with

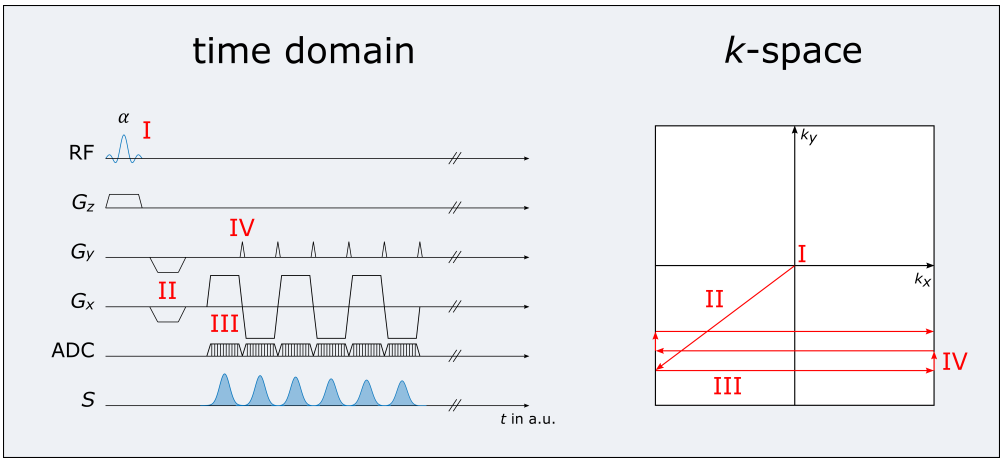

Figure 2.15: 2D echo-planar imaging sequence diagram and k-space trajectory.

the opposite sign moving to the upper left corner of k-space instead. Without any intermediate refocusing pulse, the gradient echo is read at $t = \mathrm{TE}$ with the same readout gradient and ADC sampling a full line of k-space. Likewise, the whole procedure is repeated after one TR. Yet, omitting the refocusing pulse and having lower flip angles allows for much shorter repetition times. For short TR, it is possible that not all the magnetisation relaxes back into thermal equilibrium. The remaining transverse magnetisation can either be rewound, i. e. all applied gradients are reversed, thus moving back to the centre of k-space, or spoiled, i. e. strong gradients are applied in x- and y-direction in order to maximally dephase the remaining transverse magnetisation. The flip angle α has to be chosen appropriately in order to maximize the signal after repeated excitation and relaxation during TR. For spoiled gradient echo sequences, the flip angle that gives maximum signal for a tissue with longitudinal relaxation time T_1 is given by the Ernst angle

Jens Frahm won the European Inventor Award in 2018 for the development and his further work on gradient echo sequences [Haase et al., 1986] that paved the way for accelerated MRI.

$$\alpha_\mathrm{E} = \arccos\left(\mathrm{e}^{-\frac{\mathrm{TR}}{T_1}}\right) \quad . \tag{2.88}$$

By choosing short repetition times with the corresponding Ernst angles, the gradient echo sequence allows sampling k-space with much higher efficiency leading to shorter scan times or higher resolution images.

ECHO PLANAR IMAGING SEQUENCES If even shorter acquisition times are needed, echo-planar imaging (EPI) sequences can be utilised (Figure 2.15). Negative gradients are applied in x- and y-direction after excitation and slice selection in order to jump to the lower left corner of k-space (I and II). Then, a gradient echo is acquired by applying a strong positive readout gradient in x and sampling one line in k-space with the ADC (II). After that, a small positive phase encoding gradient, a so-called 'blip' (IV) is applied in y-direction to jump to the next higher line in k-space. This line is read again with an ADC and readout gradient in x, the latter having a negative sign this time however. This succession of readout gradients with alternating signs and phase

encoding blips is applied in such a rapid fashion that the whole k-space can be sampled after only one excitation. This sampling technique requires fast switching of strong gradients and, thus, is rather demanding for the hardware and also prone to artefacts. Yet, it enables fast image acquisition mandatory for applications, such as functional magnetic resonance imaging (fMRI).

2.2.4 *Image Contrasts*

MRI is a powerful imaging modality due to its strong soft tissue contrast. Generally, this contrast is caused by differences in the relaxation times T_1, T_2 and the proton density (PD). The contribution of one single parameter to the observed contrast, however, can be manipulated by choosing the sequence parameters appropriately. For instance, by selecting short TE, the transverse magnetisation does not have much time to dephase before the signal is acquired, thus, limiting the contrast owing to T_2 (compare to Figure 2.5). Long TR on the other hand allows the longitudinal magnetisation to fully relax back to equilibrium yielding the same signal magnitude for subsequent excitations independent of T_1 (compare to Figure 2.3). It is therefore that short TE and TR generally promote T_1 contrast, i. e. the image would be called T_1-weighted, whereas long TE and TR promote T_2 contrast, i. e. the image would be called T_2-weighted. A combination of short TE and long TR suppresses contrast owing to relaxation times leaving the fundamental proton density as the only difference, which yields a PD-weighted image. Long TE and short TR does not generate any physiological contrast. Optimal contrast is achieved when TE and TR are in the order of T_2 and T_1 respectively. Figure 2.16 shows an exemplary brain slice from a spin echo sequence depicting the three distinct contrasts together with the corresponding TR and TE. Tissues with long T_1 and T_2, such as cerebrospinal fluid (CSF), generally appear darker on T_1-weighted and brighter on T_2-weighted images. T_1-weighting is usually preferred for imaging of the anatomy whereas T_2-weighting is advantageous for pathology as it is more sensitive to oedema.

Short and long TR and TE are always with regard to the corresponding relaxation times T_1 and T_2.

2.2.5 *Dynamic Contrast Enhanced Imaging*

Dynamic contrast enhanced (DCE) imaging is a technique that measures time-resolved T_1-weighted MR images during the pass of an injection of a gadolinium-based contrast agent. It allows to infer information about haemodynamic parameters, such as the blood flow or volume, from the temporal evolution of the signal magnitude $S(t)$ in every voxel. The analysis of DCE data consists of two distinct steps: First, the concentration of the contrast agent over time $c(t)$ has to be derived from $S(t)$ and second, tracer-kinetic theory has to be applied to $c(t)$ in order to quantify haemodynamic parameters.

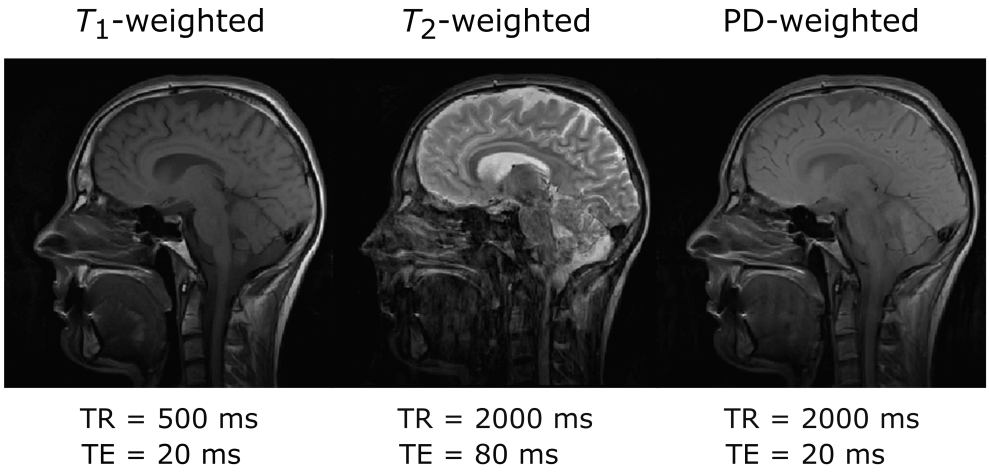

Figure 2.16: Exemplary sagittal brain slice from a spin echo sequence depicting a T_1- T_2- and PD-weighted image together with the corresponding TR and TE.

One possibility to estimate $c(t)$ is to use the relative signal enhancement, i. e. to normalise the signal to the baseline before contrast agent injection S_0 according to

$$c(t) = \frac{R_{10}}{r_1} \frac{S(t) - S_0}{S_0} \quad . \tag{2.89}$$

Here, R_{10} is the longitudinal relaxation rate of the tissue prior to the injection of contrast agent and r_1 is the relaxivity of the contrast agent itself. However, this approach assumes that the signal is always linear with the concentration of contrast agent, which is not necessarily given.

With respect to tracer-kinetic theory, all DCE approaches assume linear and stationary systems [Sourbron and Buckley, 2011]. This means that the tissue concentration $c_t(t)$ is proportional to the convolution of a residue function $R(t)$ and the concentration in an artery $c_a(t)$ supplying blood to the region of interest (ROI)

$$c_t(t) = f_p \cdot R(t) * c_a(t) \quad . \tag{2.90}$$

The factor of proportionality f_p is the plasma flow carrying contrast agent into the ROI and $c_a(t)$ is usually called the arterial input function (AIF). f_p can be directly inferred from Equation 2.90 by deconvolution; yet, by applying tracer-kinetic modelling, additional haemodynamic parameters can be reconstructed from the temporal evolution of $R(t)$. A good overview of different models and general DCE is given by Sourbron and Buckley [2011] and Ingrisch and Sourbron [2013].

2.2.6 *Arterial Spin Labelling*

Arterial spin labelling (ASL) is a non-invasive MRI technique to measure tissue perfusion using the water in arterial blood itself as an endogenous and freely-diffusible tracer. The method and similar concepts were proposed by Detre

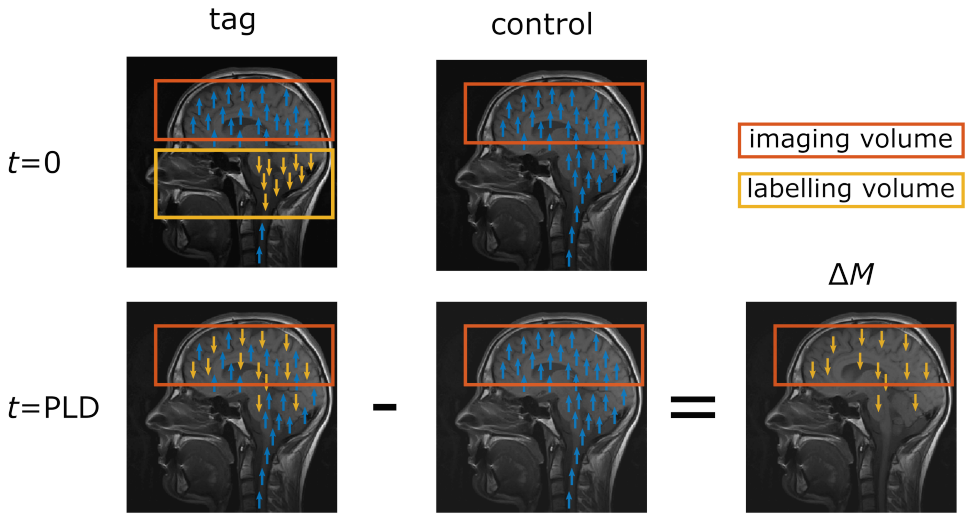

Figure 2.17: Schematic process of arterial spin labelling in the brain. The magnetisation of the inflowing arterial blood is inverted prior to imaging for the 'tag' image whereas it is left untouched for the 'control' image. The difference image ΔM = tag − control is perfusion-weighted.

Recently, ASL has been brought more and more into focus owing to the findings that some gadolinium-based MR contrast agents revealed significant tissue accumulation [Ramalho et al., 2016].

et al. [1992], Williams et al. [1992] and Kwong et al. [1992] in 1992. The general concept of ASL is that two images are acquired, one 'tag' and one 'control' image. For the 'tag' image, incoming arterial blood is labelled proximal to the tissue of interest first, usually by inverting the magnetisation. Then the image is acquired after allowing the labelled blood water to travel from the labelling to the imaging site and exchange with the tissue water during the so-called post-labelling delay (PLD). Caution has to be exerted to label the blood water in vessels that actually feed the tissue that is being imaged. The 'control' image is a mere image without any preparation of magnetisation. Assuming that the static components are the same in both images, the difference image ΔM = tag − control is a measure of the tissue perfusion, thus also called perfusion-weighted. The process is shown schematically in Figure 2.17 for an application in the brain. One major issue in ASL is that the perfusion signal makes up only approximately 1% of the total tissue signal leaving the ΔM image with very poor SNR. Hence, several pairs of 'tag' and 'control' image are usually acquired and averaged for ASL.

The readout of the actual images can be chosen freely, for example a 3D-EPI; however, three types of ASL are commonly distinguished depending on their approach for labelling the blood water (see Figure 2.18).

CONTINUOUS ARTERIAL SPIN LABELLING The ASL method originally proposed by Detre et al. [1992] and Williams et al. [1992] employs a continuous RF irradiation proximal to the imaging FOV for labelling, hence it is called continuous arterial spin labelling (CASL). When a magnetic field gradient is simultaneously applied along the flow direction of the arterial blood, the magnetisation experiences a slow variation of resonance frequency lead-

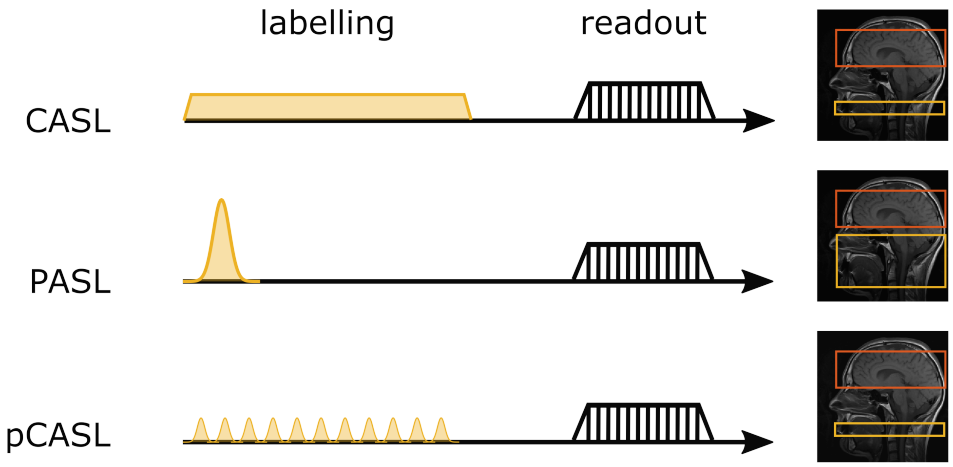

Figure 2.18: Different labelling techniques as applied in continuous arterial spin labelling (CASL), pulsed arterial spin labelling (PASL) and pseudocontinuous arterial spin labelling (pCASL). CASL uses continuous RF irradiation labelling the magnetisation in a thin slice by flow-driven adiabatic inversion. PASL utilises a short 180° RF pulse to invert the magnetisation inside a thick slab. pCASL employs flow-driven adiabatic inversion in a thin slice similar to CASL; however, it mimics the effect of continuous RF irradiation by a train of very short pulses. The labelling volume is depicted in yellow, the imaging volume is depicted in orange.

ing to an effective inversion while the blood flows through the thin labelling slice. The RF irradiation is typically kept up 2-4 s for this so-called flow-driven adiabatic inversion.

PULSED ARTERIAL SPIN LABELLING The longer the RF irradiation, the more energy is deposited in the tissue. Moreover, the RF hardware is not optimised for continuous but rather pulsed irradiation. Hence, Edelman et al. [1994] proposed to use a short (10-20 ms) 180° RF pulse to invert the magnetisation of the blood water inside a thick slab proximal to the imaging volume. This so-called pulsed arterial spin labelling (PASL), has higher labelling efficiency, however, it suffers from strongly varying arrival times of the labelled blood in the imaging volume due to the thick labelling slab. This leads to a varying amount of T_1 relaxation and, thus, introduces a bias into the perfusion estimates.

PSEUDOCONTINUOUS ARTERIAL SPIN LABELLING To exploit the advantages of both techniques, Wu et al. [2007] and Dai et al. [2008] proposed to combine CASL and PASL by using a flow-driven adiabatic inversion inside a thin labelling slice, yet, employing a train of very short ($\approx$ 1 ms) RF pulses. This approach is called pseudocontinuous arterial spin labelling (pCASL).

If the difference image ΔM is corrected for biases, for instance from T_1 relaxation, and referenced to a PD-weighted image, the actual perfusion values can be quantified. The perfusion parameter in the brain is called cerebral blood flow (CBF) and usually given in ml/100 g/min, i. e. referenced to 100 g tissue. Typical values are in the order of 60 ml/100 g/min in grey matter and 20 ml/100 g/min in white matter [Günther et al., 2005]. A good overview of perfusion quantification using ASL is given by the consensus paper from Alsop et al. [2015].

2.3 MAGNETIC SUSCEPTIBILITY

The volume magnetic susceptibility of a material describes its capability to become macroscopically magnetised in an external magnetic field with strength $\vec{H}$. In general, it can be defined as a tensor of rank 2 with the following equation

$$\vec{M} = \overline{\overline{\chi}}_{V,\mathrm{m}}(\vec{H})\vec{H} \tag{2.91}$$

where $\vec{M}$ is the magnetisation. The indices are sometimes stated to distinguish it from the molar and mass magnetic susceptibility as well as from the electric susceptibility; however, they will be omitted from now on. In most materials, especially in human tissue, the magnetic susceptibility is independent of the applied magnetic field strength. Furthermore, most of the human tissues can be approximated as isotropic, which leaves us with a scalar magnetic susceptibility and the linear relationship

$$\vec{M} = \chi\vec{H} \quad . \tag{2.92}$$

For the magnetic flux density $\vec{B}$, this means

$$\begin{aligned} \vec{B} &= \mu_0(\vec{H} + \vec{M}) \\ &= \mu_0\frac{1+\chi}{\chi}\vec{M}(\chi) \end{aligned} \tag{2.93}$$

with the vacuum permeability $\mu_0 = 4\pi \cdot 10^{-7}$.

χ is a dimensionless quantity and can range from -1 to infinity. This is, however, only true in the international system of units (SI) since χ has to be divided by a factor of 4π if one switches to the still often used centimetre-gram-second (cgs) system. Materials are generally divided into three categories: diamagnetic ($\chi < 0$), paramagnetic ($\chi > 0$) and ferromagnetic ($\chi \gg 0$). In the special case of $\chi = -1$, any external magnetic field is perfectly compensated inside the material, thus, the substance is superconductive. Water and, hence, also human tissue is slightly diamagnetic with χ only in the range of -10^{-6}. Because of this, χ is often stated in parts per million (ppm). Although there are also para- and ferromagnetic materials in the body, especially iron, their concentration is always so low that all human tissues have a negative susceptibility. It is therefore that tissue susceptibility is often given relative to χ_{water}, i. e. it is said to be either more dia- or paramagnetic than water. Table 2.3 shows the absolute magnetic susceptibility of different materials.

Table 2.3: Volume magnetic susceptibilities in SI units of different materials taken from Schenck [1996] and Jain et al. [2012].

Material	χ in ppm
Bismuth	-164
Fully oxygenated blood	-9.15
Water†	-9.05
Magnesium	11.7
Stainless steel (non-magnetic, austentic)	$3520 - 6700$

† For $T = 37^\circ\,\mathrm{C}$, $\rho = 993.3\,\mathrm{kg/m^3}$, $m_{\mathrm{mol}} = 18.015\,\mathrm{g/mol}$

2.3.1 *Lorentz Approach*

Assuming a static external field $\vec{B}_{\mathrm{ext}}(\vec{r}) = \vec{B}_0 + \vec{B}_{\mathrm{inhom}}$ of an MRI scanner, which itself already consists of the static homogeneous main field $\vec{B}_0$ and the static hardware-related inhomogeneous field $\vec{B}_{\mathrm{inhom}}$. If a material with a certain χ is placed in $\vec{B}_{\mathrm{ext}}(\vec{r})$, it will become magnetised and, thus, create an additional perturbation or demagnetisation field $\vec{B}_{\mathrm{p}}(\vec{r})$. This perturbation is mainly generated by the magnetic field of the moving electrons in the atoms of the material, neglecting the contribution of the nucleus. Using the first non-zero term of the multipole expansion yields a dipole field

$$\vec{b}_{\mathrm{p}}(\vec{r}, \vec{m}) = \mu_0 \cdot \begin{cases} \frac{3\hat{r}(\vec{m}\cdot\hat{r}) - \vec{m}}{4\pi ||\vec{r}||_2^3} & , \vec{r} \neq 0 \\ \frac{2}{3}\vec{m} & , \vec{r} = 0 \end{cases} \tag{2.94}$$

with the unit vector $\hat{r}$ in the direction $\vec{r}$ and the magnetic moment of the electron $\vec{m}$.

Assuming that the field is observed at a point $\vec{r}$ that is far away from the atom itself compared to its spatial extent, a dipole approximation can be used, which states that the macroscopic perturbation field can be calculated by merely summing over all dipole moments $\vec{m}_i$ at positions $\vec{r}_i$

$$\vec{B}_{\mathrm{p}}(\vec{r}) = \sum_i \vec{b}_{\mathrm{p}}(\vec{r} - \vec{r}_i, \vec{m}_i) \quad , \vec{r} \neq \vec{r}_i \quad . \tag{2.95}$$

When dealing with macroscopic samples like in MRI, however, carrying out this summation is generally not practicable. To circumvent this issue, the Lorentz approach can be applied, which divides the area around $\vec{r}$ into a near region V_{near} and distant region V_{dist}. In the near region V_{near}, the magnetic moments are considered discrete and, thus, the summation has to be conducted. In V_{dist} on the other hand, the magnetic moments become continuous and, hence, can be represented by a magnetic moment density, i. e.

magnetisation $\vec{M}(\vec{r})$. This simplifies the summation process to an integration. Taking this into account, the overall magnetic field may be written as

$$\begin{aligned}\vec{B}(\vec{r}) &= \vec{B}_{\text{ext}}(\vec{r}) + \sum_d \vec{b}_{\text{p}}(\vec{r}-\vec{r}_d, \vec{m}_d) \\ &= \vec{B}_{\text{ext}}(\vec{r}) + \mu_0 \int\limits_{V_{\text{dist}}(\vec{r})} \left\langle \sum_i \frac{3\hat{l}(\hat{m}_i \cdot \hat{l}) - \hat{m}_i}{4\pi||\vec{r}-\vec{r}\,'||_2^3} ||\vec{m}_i||_2 \delta(\vec{r}\,' - \vec{r}_i) \right\rangle \mathrm{d}^3\vec{r}\,' \\ &\quad + \sum_j \vec{b}_{\text{p}}(\vec{r}-\vec{r}_j, \vec{m}_j) \\ &= \vec{B}_{\text{ext}}(\vec{r}) + \mu_0 \int\limits_{V_{\text{dist}}(\vec{r})} \frac{3\hat{l}(\hat{M}(\vec{r}\,') \cdot \hat{l}) - \hat{M}(\vec{r}\,')}{4\pi||\vec{r}-\vec{r}\,'||_2^3} ||\vec{M}(\vec{r}\,')||_2 \, \mathrm{d}^3\vec{r}\,' \\ &\quad + \vec{B}_{\text{near}}(\vec{r}) \\ &= \vec{B}_{\text{ext}}(\vec{r}) + \vec{B}_{\text{dist}}(\vec{r}) + \vec{B}_{\text{near}}(\vec{r})\end{aligned} \tag{2.96}$$

Again, the prime does not refer to the rotating frame of reference here but merely denotes the integration variable.

with the unit vector $\hat{l}$ pointing along $\vec{r}-\vec{r}\,'$ and Dirac's delta distribution $\delta(\vec{r})$. Here, i is summed for all $\vec{r}_i \in V_{\text{dist}}$ and j for all $\vec{r}_j \in V_{\text{near}}$. The brackets $\langle\rangle$ shall denote the proper averaging process that is necessary to obtain the macroscopic magnetisation $\vec{M}(\vec{r})$ from the microscopic magnetic moments $\vec{m}_i$, which is explained in Hu [2000]. One has to bear in mind that the magnetic field is not only determined by the distribution of the single magnetic moments but also by the chemical environment of the atoms and molecules themselves. It is therefore that additional parameters, such as magnetic shielding of the electron shell and paramagnetic effects of second order, can be incorporated into the so-called chemical shift σ, leading to

$$\vec{B}(\vec{r}) = (1-\sigma) \cdot \left(\vec{B}_{\text{ext}}(\vec{r}) + \vec{B}_{\text{dist}}(\vec{r}) + \vec{B}_{\text{near}}(\vec{r}) \right) \quad . \tag{2.97}$$

In MRI, it is known that the chemical shift plays a significant role only in fat tissue and, hence, is usually neglected in brain imaging, for example. The form of V_{near} can be chosen arbitrarily as long as its size still allows the assumption of a magnetic moment density in V_{dist}. Generally, it is said that the size should be microscopically large but macroscopically small. Assuming that $\vec{B}_{\text{ext}}(\vec{r}) = B_{\text{ext}}\hat{z}$ and $|\chi| \ll 1$ as it is common in MRI, a first-order approximation of Equation 2.93 can be used for the distance field in Equation 2.96

$$B_{\text{dist}}(\vec{r}) = B_{\text{ext}}(\vec{r}) \int\limits_{V_{\text{dist}}(\vec{r})} \chi_{\text{app}}(\vec{r}\,') \cdot b_\chi(\vec{r}-\vec{r}\,') \, \mathrm{d}^3\vec{r}\,' \tag{2.98}$$

with the macroscopic unit dipole function

$$b_\chi(\vec{r}) = \frac{3\hat{r}(\hat{z}\cdot\hat{r}) - \hat{z}}{4\pi||\vec{r}||_2^3} \cdot \hat{z} = \frac{3\cos^2\theta - 1}{4\pi||\vec{r}||_2^3} \quad , \vec{r} \neq 0 \tag{2.99}$$

and the apparent magnetic susceptibility

$$\chi_{\text{app}} = \hat{z}^{\text{T}} \cdot \overline{\overline{\chi}} \cdot \hat{z} \quad . \tag{2.100}$$

By redefining the macroscopic unit-dipole function to

$$\breve{b}_\chi(\vec{r}) = \begin{cases} b_\chi(\vec{r}) & ,\vec{r} \neq 0 \\ \breve{b}_{\chi,0} & ,\vec{r} = 0 \end{cases} \tag{2.101}$$

and extending the integral in Equation 2.98 to the full space, one obtains a convolution integral describing the classical macroscopic field and a compensation integral over V_{near}

$$\begin{aligned} B_{\text{dist}}(\vec{r}) = B_{\text{ext}}(\vec{r}) \Bigg(& \int \chi_{\text{app}}(\vec{r}\,') \cdot \breve{b}_\chi(\vec{r} - \vec{r}\,') \, \mathrm{d}^3\vec{r}\,' \\ & - \int\limits_{V_{\text{near}}(\vec{r})} \chi_{\text{app}}(\vec{r}\,') \cdot \breve{b}_\chi(\vec{r} - \vec{r}\,') \, \mathrm{d}^3\vec{r}\,' \Bigg) \quad . \end{aligned} \tag{2.102}$$

The actual value of the dipole function at $\vec{r} = 0$ is not important for $B_{\text{dist}}(\vec{r})$ as it is present in both integrals. Assuming that the variation of $\chi_{\text{app}}(\vec{r})$ is negligible within V_{near}, gives

$$\begin{aligned} B(\vec{r}) = {} & B_{\text{ext}}(\vec{r}) + B_{\text{ext}}(\vec{r}) \cdot \{\chi_{\text{app}}(\vec{r}) * \breve{b}_\chi(\vec{r})\} \\ & + \left(B_{\text{near}}(\vec{r}) - B_{\text{ext}} \cdot \chi_{\text{app}} \int\limits_{V_{\text{near}}(\vec{r})} \breve{b}_\chi(\vec{r} - \vec{r}\,') \, \mathrm{d}^3\vec{r}\,' \right) \end{aligned} \tag{2.103}$$

for the total field with the 3D convolution operator $*$.

A further approximation, which is commonly used in MRI, is that the magnetic moments are randomly distributed. In this case, the summation over all dipoles inside V_{near} and, hence, $\vec{B}_{\text{near}}$ equals 0 when V_{near} is spherical (Lorentz sphere). This approximation is reasonable in most tissues; yet, it does not necessarily hold in highly anisotropic tissues, such as brain white matter. However, the near field also vanishes in the case of random Brownian motion of the hydrogen nuclei within a steadfast distribution of dipoles [Durrant et al., 2003]. Assuming a Lorentz sphere and exploiting the mean-value theorem of harmonic functions [Hu, 2000] simplifies the rightmost integral in Equation 2.103 to

$$\int\limits_{V_{\text{near}}(\vec{r})} \breve{b}_\chi(\vec{r} - \vec{r}\,') \, \mathrm{d}^3\vec{r}\,' = \breve{b}_{\chi,0} \quad . \tag{2.104}$$

As mentioned before, $\breve{b}_{\chi,0}$ can be chosen arbitrarily without affecting $B(\vec{r})$ and, thus, one obtains the source to field equation

$$B(\vec{r}) = B_{\text{ext}}(\vec{r}) + B_{\text{ext}}(\vec{r}) \cdot \{\chi_{\text{app}}(\vec{r}) * \breve{b}_\chi(\vec{r})\} \tag{2.105}$$

by setting $\breve{b}_{\chi,0} = 0$.

2.4 TISSUE OXYGENATION

The main amount of energy created inside living cells at rest is due to the oxidation of glucose as part of the aerobic metabolism according to

$$C_6H_{12}O_6 + 6\,O_2 \rightarrow 6\,CO_2 + 6\,H_2O + \Delta E \quad . \tag{2.106}$$

Especially brain tissue needs a constant amount of oxygen to work properly, a phenomenon called autoregulation. Both the delivery of oxygen and glucose and other nutrients to the tissue and the removal of the metabolic waste, such as CO_2, is executed by the blood.

2.4.1 *Properties of Blood*

The affinity of binding oxygen depends inversely on the blood acidity and CO_2 concentration. This is known as the Bohr effect.

Human blood comprises blood cells that are suspended in a liquid phase called blood plasma. Blood plasma makes up approximately 55 % of the total blood volume and consists, apart from proteins and dissolved glucose, hormones, mineral ions and carbon dioxide for example, mainly of water ($\approx$ 90 %). The blood cells on the other hand are subdivided into red (erythrocytes) and white blood cells (leukocytes) as well as platelets (thrombocytes). The platelets play a vital role in the clotting of blood and the main function of the white blood cells is the immune defence. The red blood cells make up the largest part ($\approx$ 96 %) of blood cells and mainly function as carrier for oxygen. The volume fraction of the red blood cells with regard to the total blood volume is called haematocrit (Hct) and is usually around 45 % in healthy humans though the exact number varies from person to person and depends on gender and other factors. Red blood cells mainly consist of haemoglobin, a molecule that itself comprises four metalloproteins as subunits. These subunits have the coordination complex haem, which is built around a central Fe^{2+} ion, as a prosthetic group. Each Fe^{2+} can bind one O_2 molecule as additional ligand allowing a maximum of four O_2 molecules per haemoglobin. The oxygen-bound state is referred to as oxyhaemoglobin (HbO_2) whereas the unbound state is called deoxyhaemoglobin (Hb). The oxygen saturation of the blood Y is defined as the relative concentration of HbO_2 with regard to the total haemoglobin concentration

After binding the first O_2 molecule, the haemoglobin undergoes conformational changes, making the subsequent oxygen binding easier.

$$Y = \frac{[HbO_2]}{[HbO_2] + [Hb]} \quad . \tag{2.107}$$

One usually distinguishes between arterial and venous oxygen saturation denoted as Y_a and Y_v or SaO_2 and SvO_2 respectively.

Furthermore, binding oxygen alters the magnetic properties of the iron ion in haemoglobin. Free Fe^{2+} has six valence electrons distributed across five 3d-orbitals leaving four electrons unpaired. These five energy levels are, however, degenerated. In deoxyhaemoglobin, Fe^{2+} experiences a weak ligand field leading to a splitting into three lower and two higher energy levels. Yet, it remains energetically favourable for the electrons to stay unpaired. Only when oxygen is bound in oxyhaemoglobin, the energy difference due to the

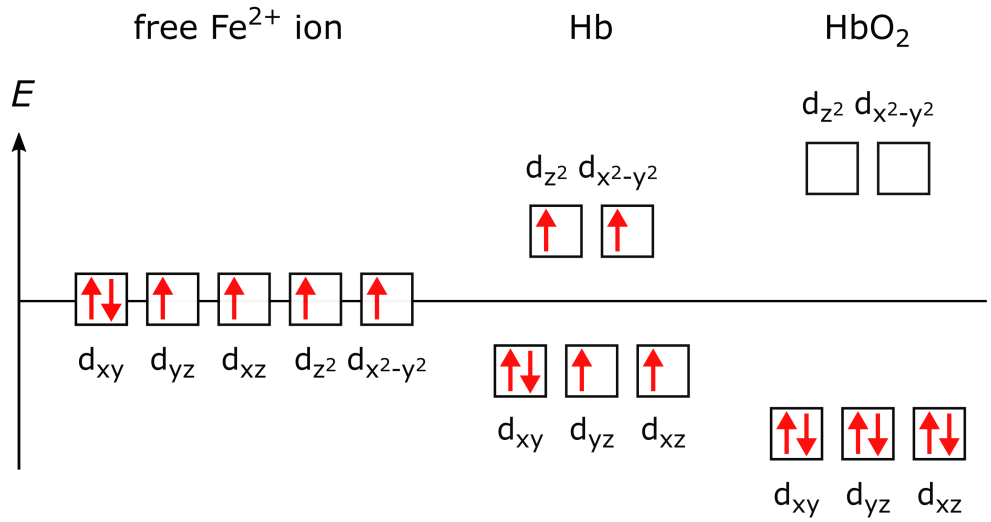

Figure 2.19: Free Fe^{2+} ions have six valence electrons distributed across five d-orbitals. These energy states are degenerated without external ligand field. The weak ligand field present in deoxyhaemoglobin (Hb) leads to a splitting into two higher and three lower energy states. However, it is still favourable to keep four unpaired electrons maintaining the total spin quantum number $S = 2$. Only in the strong ligand field present for oxyhaemoglobin (HbO_2), the splitting becomes large enough for the two higher energy electrons to pair with the lower energy ones yielding $S = 0$. Hence, Hb is paramagnetic whereas HbO_2 is diamagnetic.

now strong ligand field becomes high enough for the electrons inside the two higher energy levels to fall down and pair with the lower energy level ones. Hence, the paramagnetic deoxyhaemoglobin with total spin quantum number $S = 2$ turns into the diamagnetic oxyhaemoglobin with $S = 0$ (see Figure 2.19). This difference in magnetic susceptibility between Hb and HbO_2 is the reason for the blood oxygenation level-dependent (BOLD) effect, which is the basis of fMRI for instance.

Assuming that only red blood cells (χ_{rbc}) and plasma (χ_{plasma}) have significant contributions, the macroscopic magnetic susceptibility of blood can be calculated according to Weisskoff and Kiihne [1992]

$$\chi_{\text{blood}} = \text{Hct} \cdot \chi_{\text{rbc}} + (1 - \text{Hct}) \cdot \chi_{\text{plasma}} \quad . \tag{2.108}$$

The magnetic susceptibility of the red blood cells has a contribution from both fully oxygenated (χ_{oxy}) and deoxygenated erythrocytes (χ_{deoxy})

$$\chi_{\text{rbc}} = Y \cdot \chi_{\text{oxy}} + (1 - Y) \cdot \chi_{\text{deoxy}} \quad . \tag{2.109}$$

Combining Equation 2.108 and 2.109 yields

$$\frac{\chi_{\text{blood}} - \chi_{\text{plasma}}}{\text{Hct}} = (1 - Y) \cdot (\chi_{\text{deoxy}} - \chi_{\text{oxy}}) + \chi_{\text{oxy}} - \chi_{\text{plasma}} \quad . \tag{2.110}$$

Assuming $\chi_{\text{plasma}} \approx \chi_{\text{water}}$ [Schenck, 1996] and defining $\Delta\chi_{\text{do}} = \chi_{\text{deoxy}} - \chi_{\text{oxy}}$ and $\Delta\chi_x = \chi_x - \chi_{\text{water}}$ simplifies the equation to

$$\frac{\Delta\chi_{\text{blood}}}{\text{Hct}} = (1 - Y) \cdot \Delta\chi_{\text{do}} + \Delta\chi_{\text{oxy}} \quad . \tag{2.111}$$

Equation 2.111 allows to quantify the venous oxygen saturation Y_{v} from the magnetic susceptibility of venous blood. $\Delta\chi_{\text{do}}$ has been estimated to be 2.26 ppm by Weisskoff and Kiihne [1992] but Spees et al. [2001] measured a value of 3.39 ppm. Moreover, one has to keep in mind that the Hct in small vessels can be lower by up to 15 % compared to larger vessels.

2.4.2 *Oxygenation Parameters*

The absolute consumption of oxygen in mol per tissue mass and time is given by the metabolic rate of oxygen or by the cerebral metabolic rate of oxygen (CMRO2) in case of brain tissue. Typical values in the healthy brain are 120-180 µmol/100 g/min in grey matter and 40-80 µmol/100 g/min in white matter [Leenders et al., 1990; Ito et al., 2004]. The ratio of oxygen consumption and delivery is defined as the oxygen extraction fraction (OEF) and can also be considered as the relative change of oxygen saturation as the blood travels through the capillary network from the arterial to the venous side

$$\text{OEF} = \frac{[\text{HbO}_2]_{\text{a}} - [\text{HbO}_2]_{\text{v}}}{[\text{HbO}_2]_{\text{a}}} = 1 - \frac{Y_{\text{v}}}{Y_{\text{a}}} \quad . \tag{2.112}$$

Owing to the autoregulation, the OEF should be uniform and homogeneous throughout the healthy brain at rest and is usually around 40 % [Gusnard and Raichle, 2001]. However, the OEF can become of interest in pathologies, such as brain tumours, where both oxygen delivery and consumption can undergo changes. CMRO2 and OEF are connected via the cerebral blood flow (CBF) with

$$\text{CMRO2} \propto \text{OEF} \cdot \text{CBF} \quad . \tag{2.113}$$

2.5 TUMOURS OF THE BRAIN AND CENTRAL NERVOUS SYSTEM

According to the World Cancer Report from 2014 [Stewart and Wild, 2014], primary tumours of the brain and central nervous system (CNS) account for only 2 % of all cancer types globally. Nonetheless, some types reveal a disproportionally high mortality [Wen and Kesari, 2008]. One possible classification of brain and CNS tumours is by the tissue of origin with examples shown in Table 2.4. Another commonly used classification scheme is the grading system of the World Health Organization (WHO) [Louis et al., 2007, 2016]. Grades range from I to IV, indicating the aggressiveness of each tumour type and, thus, also treatment outcome. An overview of the different grades, corresponding characteristics and exemplary tumour types is given in Table 2.5. Grades I and II are considered low-grade, whereas III and IV are considered high-grade tumours.

Table 2.4: Examples of different types of tumours of the brain and CNS with the corresponding tissues of origin [American Association of Neurological Surgeons, 2019b].

Tissue of origin	Tumour types	
Astrocytes	Astrocytoma	} Glioma
Oligodendrocytes	Oligodendroglioma	
Ependyma	Ependymoma	
Neurons	Medulloblastoma	
Meningens	Meningioma	

Glioma make up approximately 80 % of all malignant primary brain tumours [Ostrom et al., 2017] with the glioblastoma multiforme, a grade IV astrocytoma, being the most frequent [Ostrom et al., 2017; Wen and Kesari, 2008]. Due to the high aggressiveness and extensive infiltration, patients with glioblastoma multiforme have a median survival time of only 12 to 15 months despite optimal treatment [Wen and Kesari, 2008]. In addition, glioblastoma multiforme often reveal areas of extensive microvascular proliferation, especially in the periphery of the tumour [Wen and Kesari, 2008]. In spite of this increased perfusion, the tumour often grows so rapidly that it eventually cuts off its own blood supply, leading to necrosis in the tumour centre [Wen and Kesari, 2008]. Moreover, the so-called *Warburg effect* can occur, which means that the cancer cells start favouring metabolism by the less efficient anaerobic glycolysis rather then the standard oxidative phosphorylation. This, however, leads to a lower oxygen content inside the cells, i. e. hypoxia, and to an increased production of metabolic waste. The reasons for the onset of the Warburg effect in cancer are still debated among oncologist, especially since it also occurs when enough oxygen is supplied to the cancer cells [Strickland and Stoll, 2017].

In general, glioblastoma multiforme usually show a heterogeneously enhancing mass with a large peritumoural oedema in standard MRI. Strong enhancement in the periphery of the tumour is often seen in T_1-weighted MRI with a gadolinium (Gd) contrast agent indicating a disruption of the blood-brain barrier. Unfortunately, treatment of high-grade glioma, especially of glioblastoma multiforme, is still challenging due to the strong heterogeneity of the tumour and infiltration of the surrounding tissue. Commonly, the tumour is delineated with T_1-weighted MRI + Gd and then surgically resected as much as possible. Surgery is usually followed by radio- and/or chemotherapy to treat possible tumour residue that has infiltrated the surrounding tissue [Wen and Kesari, 2008].

Table 2.5: WHO grading of brain and CNS tumours including corresponding tissue characteristics and tumour types [American Association of Neurological Surgeons, 2019a].

WHO grade		Characteristics	Tumour types
Low	I	• Least malignant (benign) • Possibly curable by surgery alone • Non-infiltrative • Long-term survival • Slow growing	• Pilocytic astrocytoma
	II	• Relatively slow growing • Somewhat infiltrative • Might recur as higher grade	• 'Diffuse' astrocytoma
High	III	• Malignant • Infiltrative • Tend to recur as higher grade	• Anaplastic astrocytoma • Anaplastic oligodendroglioma • Anaplastic ependymoma
	IV	• Most malignant • Rapid growth, aggressive • Widely infiltrative • Rapid recurrence • Necrosis prone	• Glioblastoma multiforme • Medulloblastoma

3

MATERIALS AND METHODS

This chapter covers all materials and methods used in this thesis from patient and data acquisition to general image processing ending with the quantification of tissue oxygenation using quantitative susceptibility mapping and quantitative blood oxygenation level-dependent techniques. Parts of this work have been published in [Hubertus et al., 2019b] and [Hubertus et al., 2019c] and the description of the corresponding methods is replicated here.

3.1 MR IMAGE ACQUISITIONS

3.1.1 *Volunteers and Patients*

MR images of seven healthy volunteers (three female, four male, age 27 ± 3 years) and one female patient with a histopathologic diagnosis of glioblastoma multiforme (WHO grade IV) were acquired at the Medizinische Fakultät Mannheim. The study had been approved by the local institutional ethics committee (Medizinische Ethikkommission II der Medizinischen Fakultät Mannheim) and has therefore been performed in accordance with the ethical standards laid down in the 1964 Declaration of Helsinki and its later amendments. Written informed consent had been given prior to the measurements. In addition, clinical MRI data of five patients (one female, four male) with a histopathologic diagnosis of glioblastoma multiforme (WHO grade IV) and two patients (one female aged 26, one male aged 38) with anaplastic astrocytoma (WHO grade III) has been analysed retrospectively. This data had been acquired at Weill Cornell Medical College in New York and the study had been approved by the local institutional review board. The age averaged over all six glioblastoma multiforme patients was 58 ± 15 years. The glioblastoma multiforme will from now on be referred to as glioblastoma and the anaplastic astrocytoma as astrocytoma. Both tumour types are considered as high-grade glioma.

3.1.2 *Scanners*

The healthy volunteers and one glioblastoma patient were scanned with a clinical 3 T MAGNETOM Trio system using a 32-channel head coil (Siemens Healthcare GmbH, Erlangen, Germany) at the Medizinische Fakultät Mannheim. A picture of the scanner and the coil is shown in Figure 3.1. Three of the remaining tumour patients had been scanned with a clinical 1.5 T and the other four with a 3 T scanner (Siemens Healthcare GmbH, Erlangen, Germany; GE Healthcare, Chicago, USA) at Weill Cornell Medical College.

Figure 3.1: 3 T MAGNETOM Trio system with 32-channel head coil from Siemens Healthcare GmbH (Erlangen, Germany), which was used for volunteer measurements.

3.1.3 *Sequences*

MULTI-GRADIENT ECHO Knowledge of the MR phase evolution with time is necessary for QSM analysis. Hence, the FID of the MR signal has to be sampled with multiple gradient echoes. For this purpose, a 3D multi-gradient echo (GRE) sequence was acquired. The sequence parameters for the volunteer measurements were: TR = 61 ms; TE_1 = 4.5 ms; ΔTE = 5.5 ms; 8 echoes; matrix size = 256 x 192 x 72; voxel size = 0.9 x 0.9 x 1.4 mm^3; flip angle = 15°; GRAPPA factor = 2 [Griswold et al., 2002]; unipolar readout; acquisition time = 7:51 min. The raw complex MRI data was saved.

The sequence parameters for the clinical patient measurements varied in the range: TR = 49 − 69 ms; TE_1 = 4.5 − 11 ms; ΔTE = 4.1 − 10.3 ms; 6 − 11 echoes; matrix size = 256 − 512 x 192 − 512 x 16 − 34; voxel size = 0.5 − 0.9 x 0.5 − 0.9 x 1.4 − 3 mm^3; flip angle = 15 − 20°. The magnitude and phase images were saved.

PSEUDOCONTINUOUS ARTERIAL SPIN LABELLING Unbalanced axial 2D pseudocontinuous arterial spin labelling (pCASL) data with an EPI readout was acquired in all healthy volunteers and one glioblastoma patient to determine CBF. The sequence parameters were: TR = 5000 ms; TE = 16 ms; labelling duration (LD) = 1500 ms; post-labelling delay (PLD) = 1500 ms; matrix size = 80 x 80; 28 slices; voxel size = 3 x 3 x 3 mm^3; distance factor = 20%; flip angle = 90°; GRAPPA factor = 2 [Griswold et al., 2002]; phase partial Fourier = 7/8 [Feinberg et al., 1986]; 20 averages; acquisition time = 3:45 min. As suggested by Alsop et al. [2015], the labelling plane was placed perpendicular to the arteries in the neck and roughly 80 mm inferior of the line connecting the anterior and posterior commissure.

DYNAMIC CONTRAST ENHANCED MRI Seven of the high-grade glioma patients had received a T_1-weighted 3D dynamic contrast enhanced (DCE) acquisition with contrast agent injection (1 ml/10 kg body weight of Gadobutrol) in order to estimate perfusion parameters. The parameters varied in the range: TR $= 3.5 - 5.8$ ms; $TE_1 = 1.2 - 1.3$ ms; temporal resolution $= 5.6 - 10.2$ ms; $24 - 40$ time points; matrix size $= 256 \times 256 \times 48 - 72$; voxel size $= 0.9 \times 0.9 \times 5$ mm^3; flip angle $= 13 - 25°$.

GRADIENT ECHO SAMPLING OF SPIN ECHO The gradient echo sampling of spin echo (GESSE) sequence was proposed by Yablonskiy and Haacke [1997] in order to generate both T_2- and T_2^*-weighted images by sampling a spin echo with several additional gradient echoes both during re- and subsequent dephasing. All seven healthy volunteers were scanned with an axial 2D GESSE sequence for qBOLD analysis with the following parameters: TR $= 2780$ ms; $TE_1 = 29$ ms; $\Delta TE = 2$ ms; 32 echoes; spin echo (SE) at 10th echo; matrix size $= 128 \times 96$; 25 slices; voxel size $= 2 \times 2 \times 2$ mm^3; distance factor $= 33\%$; flip angle $= 90°$; phase partial Fourier $= 7/8$ [Feinberg et al., 1986]; unipolar readout; 3 averages; acquisition time $= 10{:}00$ min.

MAGNETISATION-PREPARED RAPID GRADIENT ECHO 3D magnetisation-prepared rapid gradient echo (MPRAGE) [Mugler III and Brookeman, 1990] data was acquired in all seven healthy volunteers and one glioblastoma patient to have a T_1-weighted morphological reference. The parameters were: TR $= 1900$ ms; TE $= 2.4$ ms; inversion time $= 900$ ms; matrix size $= 256 \times 256 \times 176$; voxel size $= 1 \times 1 \times 1$ mm^3; flip angle $= 9°$; GRAPPA factor $= 2$ [Griswold et al., 2002]; acquisition time $= 4{:}18$ min.

Available T_1- or T_2-weighted images were used as anatomical reference for the remaining seven high-grade glioma patients.

3.2 IMAGE REGISTRATION AND SEGMENTATION

Image registration among sequences was performed with the statistical parametric mapping software SPM12 (Wellcome Trust Centre for Neuroimaging, London, UK) using the default values. SPM12 was also utilised to segment the MPRAGE data into binary grey matter (GM), white matter (WM) and cerebrospinal fluid (CSF) masks applying a probability threshold of 0.5. All post-processing was done with MATLAB R2017a (MathWorks, Natick, MA, USA).

3.3 PERFUSION ESTIMATION

3.3.1 *pCASL*

Both the control (M_c) and tag (M_t) images from the pCASL sequence were averaged and together with the PD-weighted image (M_{PD}) were used to calcu-

late the CBF in ml/100 g brain tissue/min according to the recommendations from Alsop et al. [2015] as

$$\mathrm{CBF} = \frac{6000 \cdot \lambda \cdot (M_\mathrm{c} - M_\mathrm{t}) \cdot \exp(\mathrm{PLD}/T_{1,\mathrm{blood}})}{2\alpha \cdot T_{1,\mathrm{blood}} \cdot M_\mathrm{PD} \cdot (1 - \exp(-\mathrm{LD}/T_{1,\mathrm{blood}}))} \quad . \tag{3.1}$$

Here, $\lambda = 0.9\,\mathrm{ml/g}$ is the blood-brain partition coefficient [Herscovitch and Raichle, 1985], $T_{1,\mathrm{blood}} = 1650\,\mathrm{ms}$ is the longitudinal relaxation time of arterial blood at 3 T [Lu et al., 2004] and $\alpha = 0.86$ is the labelling efficiency [Aslan et al., 2011]. The cerebral blood volume (CBV) in % was estimated from the CBF in ml/100 g brain tissue/min according to the empirical relationship found by linear regression of the combined grey and white matter data from Leenders et al. [1990]

$$\mathrm{CBV} = 0.0723 \cdot \mathrm{CBF} + 1.144 \quad . \tag{3.2}$$

3.3.2 *DCE*

In order to estimate the CBF and CBV, a two-compartment exchange model was fitted to the DCE data using the ROCKETSHIP framework [Barnes et al., 2015]. The exchange model is the most general two-compartment model assuming a plasma compartment with a plasma flow f_p in ml/100 g brain tissue/min and a plasma volume v_p in % relative to the total volume. The second compartment is the interstitial fluid that occupies the extracellular volume v_e also in %. The permeability-surface area product PS is the exchange rate between the two compartments and is considered the same in both directions. A schematic overview of the model is illustrated in Figure 3.2. Without decay of the contrast agent, the differential equations governing the tracer-kinetics can be written as

$$\begin{aligned} v_\mathrm{e}\frac{\mathrm{d}c_\mathrm{e}}{\mathrm{d}t}(t) &= \mathrm{PS} \cdot (c_\mathrm{p}(t) - c_\mathrm{e}(t)) \\ v_\mathrm{p}\frac{\mathrm{d}c_\mathrm{p}}{\mathrm{d}t}(t) &= \mathrm{PS} \cdot (c_\mathrm{e}(t) - c_\mathrm{p}(t)) + f_\mathrm{p} \cdot (c_\mathrm{a}(t) - c_\mathrm{p}(t)) \quad . \end{aligned} \tag{3.3}$$

These yield a residue function $R(t)$ in Equation 2.90 that has a bi-exponential form in the parameters f_p, v_p, v_e and PS [Ingrisch and Sourbron, 2013; Barnes et al., 2015]. To quantify concentration curves, the temporal DCE signal was corrected for T_1 decay assuming $T_{1,\mathrm{blood}} = 1664\,\mathrm{ms}$ for a large vessel haematocrit Hct = 0.42 [Lu et al., 2004] and a relaxivity $r_1 = 4.6\,\mathrm{s^{-1}mM^{-1}}$ at 1.5 T and $r_1 = 4.5\,\mathrm{s^{-1}mM^{-1}}$ at 3 T for Gadobutrol [Shen et al., 2015]. A ROI was manually placed inside the superior sagittal sinus as proposed by Keil et al. [2017] and a bi-exponential fit to the averaged signal within was conducted in order to establish the AIF $c_\mathrm{a}(t)$. Temporal smoothing with a moving average filter was applied to the data before the final deconvolution. CBF in ml/100 g brain tissue/min and CBV in % were calculated according to

$$\mathrm{CBF} = f_\mathrm{p}/(1 - \mathrm{Hct}) \tag{3.4}$$

$$\mathrm{CBV} = v_\mathrm{p}/(1 - \mathrm{Hct}) \tag{3.5}$$

again with the large vessel haematocrit Hct = 0.42 [Lu et al., 2004].

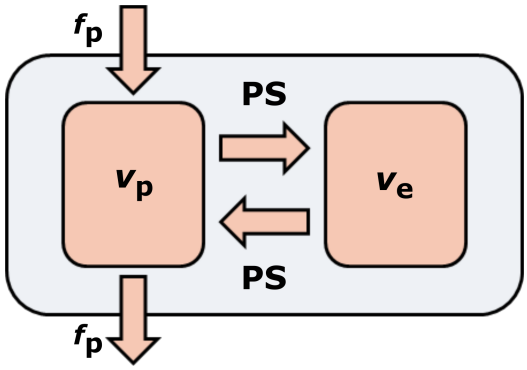

Figure 3.2: Schematic illustration of the two-compartment exchange model with a plasma (p) and extracellular (e) compartment. Parameters of the model are the plasma flow f_p, plasma volume v_p, extracellular volume v_e and permeability-surface area product PS. The exchange rate PS is assumed to be the same in both directions.

3.4 QUANTITATIVE SUSCEPTIBILITY MAPPING

Quantitative susceptibility mapping (QSM) is an image processing technique that aims at quantifying the magnetic susceptibility χ from its effect on MRI phase data [De Rochefort et al., 2008; Liu et al., 2009; Kressler et al., 2010; Wang and Liu, 2015; Schweser et al., 2016].

Equation 2.105 has to be inverted in order to determine χ from the magnetic field. This deconvolution problem is called the field to source inversion. Convolutions are most effectively executed in Fourier space owing to the Fourier convolution theorem. Thus, by defining the relative difference field (RDF) as

$$\mathrm{RDF}(\vec{r}) = \frac{B(\vec{r}) - B_{\mathrm{ext}}(\vec{r})}{B_{\mathrm{ext}}(\vec{r})} \tag{3.6}$$

one obtains the handy equation

$$\mathcal{F}(\mathrm{RDF})(\vec{r}) = \mathcal{F}(\chi)(\vec{r}) \cdot \mathcal{F}(\breve{b}_\chi)(\vec{r}) \quad . \tag{3.7}$$

Solving Equation 3.7 for χ is one of the main tasks in QSM. This is not straightforward as the problem is ill-posed or more specifically underdetermined due to the unit dipole function $\breve{b}_\chi(\vec{r})$. Its Fourier transform is defined as

$$\breve{b}_\chi(\vec{k}) = \mathcal{F}(\breve{b}_\chi)(\vec{r}) = \frac{1}{3} - \frac{k_z^2}{||\vec{k}||_2^2} = \frac{1}{3} - \cos^2\theta \tag{3.8}$$

with the azimuthal angle θ and, therefore, zero on a conical surface at the so-called magic angle $\theta_m = 54.74°$ (see Figure 3.3). This makes a simple inversion impossible. A detailed overview over all approaches to tackle these two and other general issues in QSM is given in Wang and Liu [2015] and Schweser et al. [2016].

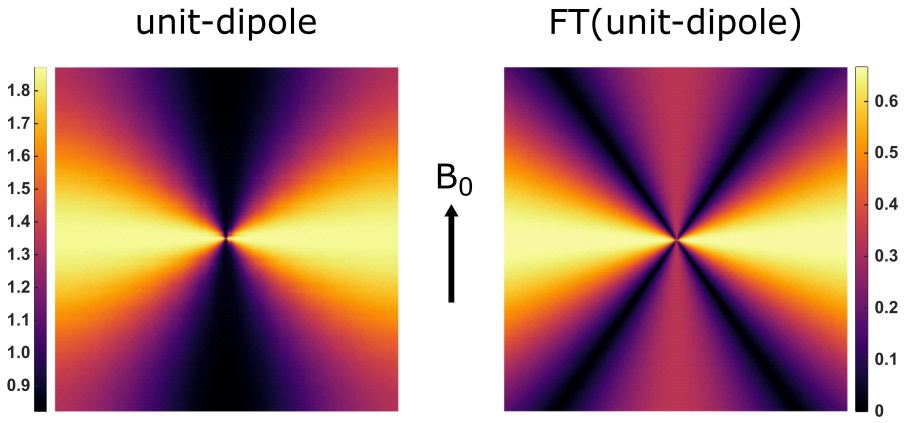

Figure 3.3: Central slice through the field pattern of a unit-dipole function given by Equation 2.99 (left) and through its Fourier transform (FT) given by Equation 3.8 (right). The amplitude is given in a.u.. The Fourier transform of the dipole is zero on a cone surface with opening angle $\theta_m = 54.74°$. B_0 indicates the direction of the magnetic field.

The RDF in Equation 3.6 is defined with the magnetic field itself; however, in MRI one usually measures the relative Larmor frequency $\Delta f_{MR}(\vec{r})$. It can be approximated as

$$\Delta f_{MR}(\vec{r}) \approx -\frac{\gamma}{2\pi}[B_b(\vec{r}) + B_0 \cdot (\chi(\vec{r}) * \breve{b}_\chi(\vec{r}))] \tag{3.9}$$

with the macroscopic unit dipole function $\breve{b}_\chi(\vec{r})$ as defined in Equation 2.101 and the static inhomogeneous or so-called background field $B_b(\vec{r})$ that combines all hardware-related field offsets. A more detailed derivation with all assumptions made, such as neglecting the chemical shift, can be found in Schweser et al. [2016]. Assuming a constant susceptibility within one voxel, the frequency offset in this voxel can also be expressed as signal phase depending on the echo time TE according to

$$\varphi(\mathrm{TE}) = \varphi_0 + 2\pi \cdot \Delta f_{MR} \cdot \mathrm{TE} = \varphi_0 + \Delta\varphi(\mathrm{TE}) \tag{3.10}$$

with the time-independent phase φ_0 at $t = 0$ owing to transmit and receive processes. This means, by evaluating the MR signal phase, the frequency offsets and, thus, the RDF can be determined by combining Equation 3.9 and 3.10. Yet, another main task in QSM is to accurately disentangle the frequency offsets induced by the static inhomogeneities $(B_b(\vec{r}))$ and by the magnetic susceptibility $(\chi(\vec{r}))$. This is a crucial step as any remaining contribution of $B_b(\vec{r})$ to the RDF will introduce biases into the final χ maps.

The toolbox can be downloaded from `http://pre.weill.cornell.edu/mri/pages/qsm.html`

The QSM analysis comprises a full processing pipeline to get from the initial phase and magnitude GRE images to the final map of the magnetic susceptibility χ (see Figure 3.4) and each step is described in this section. Most of the image processing for QSM implemented for this work is based on the MEDI toolbox, which is openly available from Cornell MRI Research Lab at Weill Cornell Medical College.

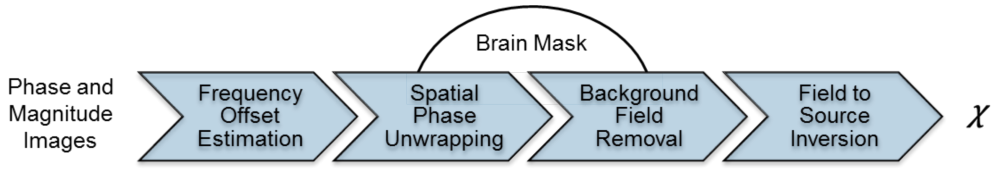

Figure 3.4: Schematic visualisation of the QSM processing pipeline from phase and magnitude images to the final χ map. The background field removal requires a mask of the brain parenchyma.

3.4.1 *MR Image Reconstruction*

Due to a phase reconstruction issue of the VB19 software installed on the MAGNETOM Trio system (Siemens Healthcare GmbH, Erlangen, Germany) at the Medizinische Fakultät Mannheim, the raw complex MRI data of the GRE sequence was reconstructed manually off-line. This was done according to Robinson et al. [2017]. The magnitude images from all 32 channels at the nth TE were combined to one magnitude image M_n by sum-of-squares

$$M_n = \sqrt{\sum_{j=1}^{32} M_{n,j}^2} \quad . \tag{3.11}$$

The phase image at TE_1 was subtracted from all subsequent phase images for each channel separately in order to remove channel-dependent phase offsets. Afterwards, the phase images at the nth TE were combined to one phase image φ_n by exponential addition weighted with the magnitude images

$$\varphi_n = \angle \left[\sum_{j=1}^{32} M_{n,j}^2 \cdot \mathrm{e}^{-\mathrm{i}\left(\varphi_{n,j} - \varphi_{1,j}\right)} \right] \quad . \tag{3.12}$$

The magnitude and phase images of the GRE sequences acquired at Weill Cornell Medical College were correctly reconstructed by the scanner and were used directly without further processing.

3.4.2 *Brain Mask Generation*

A binary mask of the brain parenchyma was generated in order to exclude the background and skull from subsequent postprocessing. First, a threshold was applied to the magnitude image averaged over all echoes. Second, the biggest connected component of this initial mask was then refined by the morphological operations opening and closing. Finally, the resulting mask was eroded with a spherical kernel of radius $r = 5\,\mathrm{mm}$.

The masks for the brain tumour patients acquired at Weill Cornell Medical College were created with the brain extraction tool [Smith, 2002] from the FMRIB software library followed by an erosion with a spherical kernel of radius $r = 3\,\mathrm{mm}$.

3.4.3 *Frequency Offset Estimation*

The frequency offset Δf represented as phase increment per echo $\Delta\varphi = 2\pi \cdot \Delta f \cdot \Delta\mathrm{TE}$ was estimated by fitting the model

$$S_\mathrm{c}(n) = M_n \cdot \mathrm{e}^{\mathrm{i}(\Delta\varphi\cdot(n-1)+\varphi_0)} \tag{3.13}$$

to the complex MRI data by a weighted least-squares optimisation. n is the echo number and M_n is the magnitude image at the nth echo so that only $\Delta\varphi$ and φ_0 remain as fitting parameters. The complex data rather than merely the phase data was utilised for fitting owing to the beneficial Gaussian noise distribution of the former [De Rochefort et al., 2008; Kressler et al., 2010; Liu et al., 2013].

3.4.4 *Spatial Phase Unwrapping*

The phase increments reconstructed in Subsection 3.4.3 are only defined in the range of $[-\pi, \pi]$ so that spatial unwrapping of the phase maps is required. This was either done by Laplacian operations [Schofield and Zhu, 2003] or by a region growing algorithm [Cusack and Papadakis, 2002]. The latter starts unwrapping areas with high SNR where the data can be considered reliable and continues into areas with lower and lower SNR. Which algorithm worked best strongly depended on the input data and hence was determined individually.

3.4.5 *Background Field Removal*

In order to correctly estimate the tissue magnetic susceptibility, the phase contribution from non-tissue sources, the so-called background field, had to be removed from $\Delta\varphi$. Here, two different algorithms were utilised for background field removal. Both either directly or indirectly exploit the fact that the z-component of the background field $\vec{B}_\mathrm{b}$ is harmonic, i. e. solves Laplace's equation $\nabla^2 B_\mathrm{b} = 0$, whereas the z-component of the local field originating from inside the brain $\vec{B}_\mathrm{loc}$ is non-harmonic, i. e. $\nabla^2 B_\mathrm{loc} \neq 0$. The mask of the brain parenchyma generated in Subsection 3.4.2 was used as ROI from which the local field is assumed to be generated. Everything outside the brain mask was considered background.

PROJECTION ONTO DIPOLE FIELDS (PDF) This algorithm assumes that any unit dipole field originating within the ROI is orthogonal to all possible unit dipole fields originating in the background. Hence, the contribution of the background field to the total measured field can be extracted by taking the inner product, i. e. projecting the total field onto a combination of all possible unit dipole fields from the background. The local brain field can then be reconstructed by subtracting the projection from the total measured field. This approach has been proposed and validated by Liu et al. [2011] and was applied to the healthy volunteer data.

LAPLACIAN BOUNDARY VALUE (LBV) This algorithm solves $\nabla^2 B_b = 0$ with boundary conditions directly using a finite difference scheme. As the magnitude of B_b is usually at least one order of magnitude larger than of B_{loc}, the background field is approximated as the total measured field at the brain boundary [Zhou et al., 2014]. This approach was applied to the tumour patient data.

After removal of the background field, the signal contribution of the RDF was defined as

$$S_{RDF} = e^{iRDF} = e^{i\Delta\varphi_{loc}/(\omega_0 \Delta TE)} \tag{3.14}$$

with the Larmor frequency ω_0.

3.4.6 *Field to Source Inversion*

The last step in the QSM pipeline is solving the ill-posed field to source inversion. In this work, the morphology enabled dipole inversion (MEDI) algorithm [Liu et al., 2012, 2013] was applied for this purpose. MEDI tackles the underdetermined problem by adding an L1 regularisation term to the least-squares minimisation that promotes solutions of χ that have consistent edges with the corresponding magnitude image. Specifically, it solves the minimisation problem

$$\chi^* = \text{argmin}_\chi \left\| \boldsymbol{m}_g \circ (g\chi) \right\|_1 + \lambda_1 \left\| \boldsymbol{W} \circ (\exp(i\boldsymbol{D} * \chi) - \boldsymbol{S}_{RDF}) \right\|_2^2 \quad . \tag{3.15}$$

Boldfaced variables refer to 3D matrices.

Here, χ is the 3D matrix of the magnetic susceptibility, $\boldsymbol{S}_{RDF}$ is the 3D matrix of the signal contribution of the relative difference field from Equation 3.14, $\boldsymbol{W} \propto 1/\sigma^2$ is a 3D weighting matrix with σ being the error estimation of $\Delta\varphi$ from the fit in Equation 3.13 and $g = \partial/\partial x + \partial/\partial y + \partial/\partial z$ is a gradient operator. The norms can be considered generalised vector norms defined as

$$\|\boldsymbol{A}\|_p = \left(\sum_{i=1}^{q} \sum_{j=1}^{r} \sum_{k=1}^{s} |a_{i,j,k}| \right)^{1/p} \tag{3.16}$$

for a matrix $\boldsymbol{A}$ of size $q \times r \times s$ and $*$ is the convolution operator and $\circ$ is the Hadamard product.

$$\boldsymbol{m}_g = \begin{cases} 0 & , ||g\boldsymbol{M}|| \geq \mu \\ 1 & , ||g\boldsymbol{M}|| < \mu \end{cases} \tag{3.17}$$

is a 3D binary matrix, which excludes edges from the GRE magnitude $\boldsymbol{M}$ data using a threshold μ that depends on the image noise. λ_1 is a scalar weighting factor that was set to 1000. Equation 3.15 was solved with a conjugate gradient method in an iterative fashion by tayloring the cost-function to the first order and calculating its gradient in every step. The added L1 regularisation in Equation 3.15 sparsifies the solution with regard to edges in the

final χ that are not present in the original magnitude $\boldsymbol{M}$. As $\check{b}_\chi(\vec{0})$ in Equation 3.8 is not well defined, the susceptibility maps from QSM have always to be referenced to a certain tissue. We chose CSF here as a water surrogate since the fundamental equation (2.111) that links blood oxygen saturation and blood magnetic susceptibility requires the susceptibility to be referenced to water. The magnetic susceptibility of CSF was manually averaged across the CSF mask generated in Subsection 3.4.1 and subtracted from the reconstructed map for the healthy volunteers.

The field to source inversion for the glioma patients was done with MEDI with automatic CSF zero reference (MEDI+0) [Liu et al., 2018]. MEDI+0 further penalises solutions with heterogeneous magnetic susceptibilities inside the CSF by adding the L2 regularisation term

$$\mathrm{reg}_{\mathrm{L2}} = \lambda_2 \left\| \boldsymbol{m}_{\mathrm{CSF}} \circ (\chi - \overline{(\boldsymbol{m}_{\mathrm{CSF}} \circ \chi)}) \right\|_2^2 \tag{3.18}$$

to Equation 3.15. Here, $\boldsymbol{m}_{\mathrm{CSF}}$ is a 3D binary matrix of the ventricles, which is automatically generated by fitting R_2^* to the magnitude data $\boldsymbol{M}$, applying a threshold to the resulting maps and by exploiting connectivity in the central brain region [Liu et al., 2018]. $\overline{(\boldsymbol{m}_{\mathrm{CSF}} \circ \chi)}$ is the mean value of the magnetic susceptibility within $\boldsymbol{m}_{\mathrm{CSF}}$ and is subtracted from the final χ map. Voxels inside the tumour masks were excluded from $\boldsymbol{m}_{\mathrm{CSF}}$. The weighting factor λ_2 was set to 100.

3.5 QUANTITATIVE BLOOD OXYGENATION LEVEL-DEPENDENT APPROACH

3.5.1 *Tissue Model*

In 1994, Yablonskiy and Haacke [1994] developed a tissue model that describes the MR signal behaviour in the presence of static magnetic field inhomogeneities created by the blood vessel network. They called it quantitative blood oxygenation level-dependent (qBOLD) model and assumed one compartment each for tissue and blood vessels with a different magnetic susceptibility. Approximating the blood vessel network as infinitely long and randomly oriented cylinders, they found

$$S(t) = S_0 \cdot \exp\left(-\nu \cdot f\left(\delta\omega \cdot t\right) - R_2 \cdot t\right) \tag{3.19}$$

for the signal decay in a gradient echo experiment. The characteristic frequency shift due to the presence of the blood vessel network is given by

$$\delta\omega = \frac{1}{3} \cdot \gamma \cdot B_0 \cdot [\mathrm{Hct} \cdot \Delta\chi_0 \cdot (1 - Y)] \tag{3.20}$$

with the susceptibility difference between fully de- and oxygenated red blood cells $\Delta\chi_0$ in SI units. $f\left(\delta\omega \cdot t\right)$ can be represented as a generalised hypergeometric function [Sukstanskii and Yablonskiy, 2001]

$$f\left(\delta\omega \cdot t\right) = {}_1^1F_2\left(\left\{-\frac{1}{2}\right\}; \left\{\frac{3}{4}, \frac{5}{4}\right\}; -\frac{9}{16}(\delta\omega \cdot t)^2\right) - 1 \quad . \tag{3.21}$$

This leaves the initial signal S_0, the transverse relaxation rate R_2, the deoxygenated blood volume ν and the venous oxygen saturation Y as parameters of the model. Equation 3.19 can be separated in two distinct regimes, the so-called short and long term regime, in which the signal decay can be approximated as

$$S(t) = S_0 \cdot \exp\left(-0.3 \cdot \nu \cdot (\delta\omega \cdot t)^2 - R_2 \cdot t\right) \quad , \quad |\delta\omega \cdot t| < 1.5 \tag{3.22}$$

$$S(t) = S_0 \cdot \exp\left(-\nu \cdot (\delta\omega \cdot t - 1) - R_2 \cdot t\right) \quad , \quad |\delta\omega \cdot t| \geq 1.5 \tag{3.23}$$

respectively. This means that the logarithmic signal decays linearly with t and $\delta\omega$ in the long term regime; yet it decays quadratically with t and $\delta\omega$ in the short term regime. Hence, a proper separation of the qBOLD parameters requires the sampling of both domains. When sampling the FID with standard gradient echo sequences however, the short term regime is restricted to the first few echoes. It is therefore that Yablonskiy and Haacke [1997] proposed the gradient echo sampling of spin echo (GESSE) sequence in order to sample the short term regime both before and after the spin echo (SE). In this case, Equation 3.19 becomes

$$S(t) = S_{\mathrm{SE}} \cdot \exp\left(-\nu \cdot f\left(\delta\omega \cdot \tau\right) - R_2 \cdot \tau\right) \tag{3.24}$$

with $\tau = t - t_{\mathrm{SE}}$ being referenced to the time of the spin echo t_{SE} and the signal magnitude at the spin echo S_{SE}.

The qBOLD model assumes that the system is in the so-called static dephasing regime, i. e. the characteristic time for a proton to diffuse a distance equal to the radius of the vessels is longer than $t_{\mathrm{c}} = 1/\delta\omega$. This approximation is generally accepted in high-field MRI. In addition, Equation 3.20 assumes that there is no frequency shift between the tissue compartment and fully oxygenated blood inside the vessel network. In general, the qBOLD model aims at disentangling the effects of the microscopic (much smaller than the voxel size) field inhomogeneities described by R_2 from mesoscopic (in the order of the voxel size) field inhomogeneities, which are mainly caused by the different susceptibility of the blood vessels. However, there are also macroscopic (much larger than the voxel size) field inhomogeneities, for example from non-uniform B_0 and B_1 fields, which have to be removed before the model can be applied.

3.5.2 *Correction for Macroscopic Field Inhomogeneities*

The magnitude signal $S(t)$ of the GRE and GESSE sequence was corrected for macroscopic inhomogeneities [Dickson et al., 2010; Hernando et al., 2012] using the frequency offset of the background field $\omega_{\mathrm{b}} = \gamma \cdot B_{\mathrm{b}}$ created during the background field removal step (Subsection 3.4.5) of the QSM reconstruction. For this, the scaling

$$S(t) \rightarrow \frac{S(t)}{S_{\mathrm{b}}(t)} \cdot S_{\mathrm{b}}\left(0\right) \tag{3.25}$$

was applied with

$$S_{\mathrm{b}}(t) = \prod_{j=1}^{3} \int_{-\infty}^{\infty} \exp\left(-\mathrm{i} \cdot k_j \cdot x_j\right) \cdot \mathrm{SRF}_j(x_j - x_{j,0}) \mathrm{d}x_j \tag{3.26}$$

and

$$k_j = \frac{\mathrm{d}}{\mathrm{d}x_j} \omega_{\mathrm{b}} \cdot t \cdot \Delta x_j \quad . \tag{3.27}$$

Here, the macroscopic background field was approximated to the first order and the image voxel size $\Delta x = (\Delta x_1, \Delta x_2, \Delta x_3)$ and the spatial response function (SRF) for a voxel centred around $x_{j,0}$ was used. The SRF differs for frequency/phase encoding and slice selection [Hernando et al., 2012] leading to a distinct correction for the 3D GRE and 2D GESSE. The SRF for frequency/phase encoding can be represented by a normalised sinc function restricted to its central lobe by a boxcar function $R(x)$ of width 1 centred around 0 [Dickson et al., 2010]

$$\mathrm{SRF}(x) = \sin(\pi x)/(\pi x) \cdot R(x) \quad . \tag{3.28}$$

Combining Equation 3.26 and 3.28 and exploiting the Fourier convolution theorem yields

$$S_{\mathrm{b,GRE}}(t) = \prod_{j=1}^{3} \int_{k_j - \pi}^{k_j + \pi} \mathrm{sinc}\left(\frac{k}{2}\right) \mathrm{d}k \tag{3.29}$$

for correction of the GRE magnitude. The correction is the same in all three dimensions as the sequence utilises only frequency/phase encoding. For 2D acquisitions however, the SRF in the direction of slice selection is given by a mere boxcar function with the slice thickness as width [Hernando et al., 2012]. This simplifies the integral in Equation 3.26 for the third dimension yielding

$$S_{\mathrm{b,GESSE}}(t) = \mathrm{sinc}\left(\frac{k_3}{2}\right) \cdot \prod_{j=1}^{2} \int_{k_j - \pi}^{k_j + \pi} \mathrm{sinc}\left(\frac{k}{2}\right) \mathrm{d}k \tag{3.30}$$

for the overall correction of the GESSE magnitude.

3.6 TISSUE OXYGENATION: QSM+qBOLD

In order to assess the brain tissue oxygenation of the seven healthy volunteers, a combined QSM and qBOLD analysis (QSM+qBOLD) based on Cho et al. [2018] was carried out for the GESSE and GRE data and the results from both acquisitions were compared. This study has been published as [Hubertus et al., 2019b] and the description of the methods presented in this section follows named publication.

3.6.1 *GESSE Analysis*

OEF in % and CMRO2 in µmol/100 g/min were reconstructed as

$$\mathrm{OEF} = 1 - \frac{Y}{Y_\mathrm{a}} \tag{3.31}$$

$$\mathrm{CMRO2} = \mathrm{CBF} \cdot \mathrm{OEF} \cdot [\mathrm{H}]_\mathrm{a} \quad . \tag{3.32}$$

Assuming an arterial oxygenation of $Y_\mathrm{a} = 0.98$ and a haematocrit of $\mathrm{Hct} = 0.357$ [Sakai et al., 1985] gives an oxygenated haeme molar concentration in arterioles of $[\mathrm{H}]_\mathrm{a} = 7.377\,\mu\mathrm{mol/ml}$ [Cho et al., 2018], leaving the venous oxygenation Y as an unknown. Additional unknowns were the deoxygenated blood volume ν, the transverse relaxation rate R_2, the signal at the spin echo of the GESSE S_0 and the non-blood susceptibility χ_nb. The latter was introduced to account for possible frequency shifts between fully oxygenated blood and tissue caused by iron deposition for instance. QSM and qBOLD data were combined into one minimisation term culminating in the cost function [Cho et al., 2018]

$$\begin{aligned} Y^*, \nu^*, {R_2}^*, {S_0}^*, {\chi_\mathrm{nb}}^* = \mathrm{argmin}_{Y,\nu,R_2,S_0,\chi_\mathrm{nb}} \Bigg\{ & \\ & \sum_\mathrm{TE} \left\| S_\mathrm{GESSE}\left(\mathrm{TE}\right) - F_\mathrm{qBOLD}\left(Y,\nu,R_2,S_0,\chi_\mathrm{nb},\mathrm{TE}\right)\right\|_2^2 \\ & + w \cdot \left\| \chi - F_\mathrm{QSM}\left(Y,\nu,\chi_\mathrm{nb}\right)\right\|_2^2 \Bigg\} \\ = \mathrm{argmin}_{Y,\nu,R_2,S_0,\chi_\mathrm{nb}} & \left\{ E_\mathrm{qBOLD} + w \cdot E_\mathrm{QSM} \right\} \quad . \end{aligned} \tag{3.33}$$

The QSM function F_QSM was defined as

$$\begin{aligned} F_\mathrm{QSM}\left(Y,\nu,\chi_\mathrm{nb}\right) = & \left[\frac{\chi_\mathrm{ba}}{\alpha} + \psi_\mathrm{Hb} \cdot \Delta\chi_\mathrm{Hb} \cdot \left(\frac{1-(1-\alpha)\cdot Y_\mathrm{a}}{\alpha} - Y \right) \right] \cdot \nu \\ & + \left(1 - \frac{\nu}{\alpha}\right) \cdot \chi_\mathrm{nb} \end{aligned} \tag{3.34}$$

with the fully oxygenated blood susceptibility in SI units $\chi_\mathrm{ba} = -0.1082\,\mathrm{ppm}$ [Zhang et al., 2017], the deoxygenated fraction of the total blood volume α set to 0.77 [An and Lin, 2002b], the haemoglobin volume fraction $\psi_\mathrm{Hb} = 0.0909$ [Zhang et al., 2015; Savicki et al., 1984] and the susceptibility difference between de- and oxyhaemoglobin $\Delta\chi_\mathrm{Hb} = 12.522\,\mathrm{ppm}$ [Cho et al., 2018] also in SI units.

The qBOLD function F_qBOLD was adapted to describe the GESSE signal behaviour [Yablonskiy and Haacke, 1994; Yablonskiy, 1998] according to

$$F_\mathrm{qBOLD}\left(Y,\nu,R_2,S_0,\chi_\mathrm{nb},t\right) = S_0 \cdot \exp\left(-\nu \cdot f\left(\delta\omega\cdot\tau\right) - R_2\cdot\tau\right) \tag{3.35}$$

with $\tau = t - t_\mathrm{SE}$ being referenced to the time of the spin echo SE and the generalised hypergeometric function $f\left(\delta\omega\cdot\tau\right)$ as defined in Equation 3.21.

$\delta\omega$ is the frequency shift [Cho et al., 2018] due the presence of deoxygenated blood inside the tissue and given by

$$\delta\omega\left(Y,\chi_{\mathrm{nb}}\right)=\frac{1}{3}\cdot\gamma\cdot B_0\cdot\left[\mathrm{Hct}\cdot\Delta\chi_0\cdot\left(1-Y\right)+\chi_{\mathrm{ba}}-\chi_{\mathrm{nb}}\right] \tag{3.36}$$

with the susceptibility difference between fully de- and oxygenated red blood cells in SI units $\Delta\chi_0 = 3.481\,\mathrm{ppm}$ [Jain et al., 2012]. Equation 3.21 was approximated by a Taylor expansion up to the 60th order to reduce the computational cost of the optimisation.

Since the qBOLD function in Equation 3.33 is highly sensitive to SNR and initial parameter values, the starting values were estimated on a low resolution data set, i. e. with a reduction of the in-plane resolution by a factor of 4. The starting values for this initial minimisation were $Y = 60\,\%$, $\nu = 3\,\%$, $R_2 = 12\,\mathrm{Hz}$, $S_0 = S_{\mathrm{GESSE}}(t_{\mathrm{SE}})$ and $\chi_{\mathrm{nb}} = \chi_{\mathrm{ba}}$. These maps of initial values were scaled up to the original data size and the fitting parameters were normalised as $x_{\mathrm{norm}} \rightarrow x/\overline{x}$ with the mean $\overline{x}$ of the starting value maps in order to have a similar weighting for all five unknowns. Equation 3.33 was solved using a MATLAB R2017a (MathWorks, Natick, MA, USA) implementation of the limited-memory projected quasi-Newton (L-BFGS) algorithm [Schmidt, 2008; Schmidt et al., 2009] with both energy terms E_{qBOLD} and E_{QSM} being normalised to their starting value. The optimisation was stopped when the relative change of the minimisation function was less than 0.005 for a total of 100 iterations. When no physiological $(0 \leq \{Y,\nu\} \leq 1)$ or logical $(0 \leq R_2, S_0)$ constraints were available, $|x_{\mathrm{norm}}| < 4$ was enforced. The weighting factor $w \in \left\{10^{-2}, 10^{-1}, \ldots, 10^{6}\right\}$ was determined with an L-curve approach [Hansen and O'Leary, 1993].

3.6.2 *GRE Analysis*

The main difference to the GESSE analysis is the qBOLD function [Ulrich and Yablonskiy, 2016]

$$\begin{aligned}F_{\mathrm{qBOLD}}\left(Y,\nu,R_2,S_0,\chi_{\mathrm{nb}},t\right)=S_0\cdot\exp\left(-R_2\cdot t\right)\cdot\Bigg(1-\frac{\nu}{1-\nu}\cdot f\left(\delta\omega\cdot t\right)\\ +\frac{1}{1-\nu}\cdot f\left(\nu\cdot\delta\omega\cdot t\right)\Bigg)\end{aligned} \tag{3.37}$$

and the initial parameter guess. Equation 3.37 is merely an approximated solution of the qBOLD model, which, however, has been considered beneficial for parameter separation in GRE data when using least-squares optimisations [Ulrich and Yablonskiy, 2016]. The starting value for Y was estimated from the straight sinus assuming a haematocrit ratio of 0.759 between large vessels and brain tissue, a large vessel $\psi_{\mathrm{Hb}} = 0.1197$, $\chi_{\mathrm{nb}} = 0$ and $\nu = 100\,\%$. The straight sinus was manually segmented by a neuroradiologist with 7 years of experience. Approximating the deoxygenated with the total CBV, the initial values for ν in % (ml blood/100 ml brain) were estimated from the CBF maps in ml/100 g/min according to Equation 3.2 and assuming a brain density of

1 g/ml. The initial value of χ_{nb} was set to χ_{ba}. Accounting for Y, ν and χ_{nb} in Equation 3.37, the starting values for S_0 and R_2 were determined by fitting a single exponential function to the remaining signal decay. Equation 3.33 was directly solved for the high resolution data without intermediate steps.

3.6.3 *Statistics*

Mean values and standard deviations of OEF, ν, R_2, χ_{nb}, CBF and CMRO2 for every subject were averaged across combined grey and white matter (GM+WM) as well as for grey matter (GM) and white matter (WM) separately. The five most inferior slices from the GESSE acquisition were not taken into account as most of them revealed obvious artefacts for OEF and ν. The means from all subjects were combined to an intersubject mean with standard deviation. Student's t-test was performed to determine significant differences ($p < 0.05$) between the means from the GESSE and GRE data. The same comparison was carried out for the means from GM and WM within each acquisition type.

3.6.4 *Conditioning*

The relative condition number (rCN) of Equation 3.35 and 3.37 with respect to Y and ν was determined according to

$$\mathrm{rCN} = \frac{|J_{Y,\nu}|^{\mathrm{m}}}{\left\|F_{\mathrm{qBOLD}}(Y,\nu)\right\|_2 / \|(Y,\nu)\|_2} \tag{3.38}$$

with the matrix norm $|J|^{\mathrm{m}} = \max_{||x||=1} ||Jx||$ and the Jacobian matrix

$$J_{Y,\nu} = \begin{pmatrix} \frac{\partial F_{\mathrm{qBOLD}}(Y,\nu,\mathrm{TE}_1)}{\partial Y} & \frac{\partial F_{\mathrm{qBOLD}}(Y,\nu,\mathrm{TE}_1)}{\partial \nu} \\ \vdots & \vdots \\ \frac{\partial F_{\mathrm{qBOLD}}(Y,\nu,\mathrm{TE}_{\mathrm{end}})}{\partial Y} & \frac{\partial F_{\mathrm{qBOLD}}(Y,\nu,\mathrm{TE}_{\mathrm{end}})}{\partial \nu} \end{pmatrix} . \tag{3.39}$$

Y and ν were varied in the range $Y = 30, 35, ..., 70\,\%$, $\nu = 1, 1.5, ..., 5\,\%$ and the other parameters were fixed to $R_2 = 11.5\,\mathrm{Hz}$, $\chi_{nb} = \chi_{ba} + 100\,\mathrm{ppb}$ and $S_0 = 1000\,\mathrm{a.u.}$ with TE taken from the two clinical sequences respectively.

3.6.5 *Simulation*

A full brain single- and multi-compartment simulation was based on the Zubal head phantom [Zubal et al., 1994]. A 256 x 256 x 128 data set of GESSE and GRE signal as well as the corresponding magnetic susceptibility was modelled according to Equation 3.35, 3.37 and 3.34 respectively. The ground truth parameters were $Y = 60\,\%$, $\nu = 4\,\%$, $R_2 = 11.5\,\mathrm{Hz}$, $\chi_{nb} = -40\,\mathrm{ppb}$, $S_0 = 1000\,\mathrm{a.u.}$ for grey matter, $Y = 60\,\%$, $\nu = 2\,\%$, $R_2 = 13.0\,\mathrm{Hz}$, $\chi_{nb} = -50\,\mathrm{ppb}$, $S_0 = 800\,\mathrm{a.u.}$ for white matter and TE as above. Gaussian noise was added to the data sets to have an SNR = 100 at the GESSE spin echo and first GRE echo, which is in accordance with the clinical acquisitions. The ground truth

OEF value and ν distribution were used for initialisation of the GRE fit and the reconstruction was carried out with the same approach as for the clinical GRE data. The simulated GESSE data was reconstructed twice: first, initialised with the ground truth OEF and the mean value of the ground truth ν distribution using the same approach as for the clinical GESSE data; and second, initialised with the ground truth OEF and ν distribution using the same approach as for the clinical GRE data. In all three cases, the reconstructed values were compared to the ground truth using the mean root squared error $\text{MRSE} = \overline{((x - x_{\text{true}})/x_{\text{true}})^2}$ over the full data set to determine accuracy.

The multi-compartment simulation modelled three compartments in white matter: a CSF compartment with $R_{2,\text{CSF}} = 4\,\text{Hz}$, a tissue compartment with $R_{2,\text{t}} = 13\,\text{Hz}$ and a myelin compartment with $R_{2,\text{m}} = 67\,\text{Hz}$. The corresponding weights were $w_{\text{CSF}} = 5\,\%$, $w_{\text{t}} = 84\,\%$ and $w_{\text{m}} = 11\,\%$. Grey matter was simulated with only two compartments $R_{2,\text{CSF}} = 4\,\text{Hz}$ and $R_{2,\text{t}} = 11.5\,\text{Hz}$ and weights $w_{\text{CSF}} = 5\,\%$, $w_{\text{t}} = 95\,\%$ [Whittall et al., 1997; Yablonskiy et al., 2013]. An additional frequency offset $\Delta f_{\text{CSF}} = 5\,\text{Hz}$ with no initial phase difference was assumed for the CSF compartment in both cases [He and Yablonskiy, 2007]. $R_{2,\text{t}}$ was considered as ground truth regarding the accuracy of R_2.

3.7 TISSUE OXYGENATION: ARTIFICIAL NEURAL NETWORKS

An ANN was trained for combined QSM+qBOLD analysis of the GRE data from all seven healthy volunteers and compared to the results of the conventional least-squares approach in Subsection 3.6.2 that used quasi-Newton (QN) optimisation. This study has been published as [Hubertus et al., 2019c] and the description of the methods presented in this section follows named publication.

3.7.1 *Network Architecture and Model*

The feed-forward network was implemented using the Neural Network Toolbox from MATLAB R2017a (MathWorks, Natick, MA, USA) similarly to Domsch et al. [2018]. It consisted of one input layer, one hidden layer with 10 nodes and one output layer. A schematic diagram of an arbitrary feed-forward network is illustrated in Figure 3.5.

The network emulated the exact solution of the qBOLD model for the FID [Yablonskiy and Haacke, 1994; Yablonskiy, 1998]

$$S_{\text{ANN}}(Y, \nu, R_2, S_0, \chi_{\text{nb}}, t) = S_0 \cdot \exp\left(-\nu \cdot f(\delta\omega \cdot t) - R_2 \cdot t\right) \tag{3.40}$$

with the generalised hypergeometric function f (Equation 3.21) and the frequency shift $\delta\omega$ (Equation 3.36). The remaining constants are the same as in Subsection 3.6.1. Similarly, the magnetic susceptibility $\chi_{\text{ANN}}(Y, \nu, \chi_{\text{nb}})$ was modelled according to Equation 3.34.

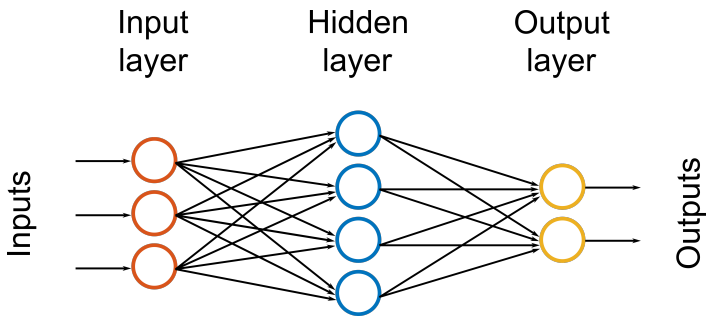

Figure 3.5: Schematic diagram of a feed-forward neural network with one input, hidden and output layer. The number of inputs, hidden nodes and outputs are chosen arbitrarily.

3.7.2 *Network Training*

10^7 parameter sets of Y, ν, R_2, χ_{nb} and S_0 were randomly generated with each parameter having a Gaussian distribution. Half of the sets physiologically represented grey matter with mean $\pm$ standard deviation being $Y = 60 \pm 30\,\%$, $\nu = 4 \pm 2\,\%$, $R_2 = 12 \pm 6\,\mathrm{Hz}$ and $\chi_{nb} = -40 \pm 40\,\mathrm{ppb}$; the other half represented white matter with $Y = 60 \pm 30\,\%$, $\nu = 4 \pm 2\,\%$, $R_2 = 17 \pm 4\,\mathrm{Hz}$ and $\chi_{nb} = -50 \pm 40\,\mathrm{ppb}$. These values were estimated from the results of Subsection 3.6.2. S_0 was calculated from Equation 3.40 so that $S(\mathrm{TE}_1) = 1$. The GRE signal decay was modelled for these parameter sets according to Equation 3.40 using the echo times $t = \mathrm{TE}$ from the in vivo sequence of the healthy volunteers (Subsection 3.1.3). Gaussian noise was added to the real and complex signal to obtain an SNR $= 100$ at the first echo, which corresponded to the in vivo data. The magnitude signal was then normalised to the first echo. Magnetic susceptibilities were estimated from Equation 3.34. 80 % of the parameter sets were used for training whereas 10 % each were utilised for validation and testing. The weights of the network were adjusted during training by minimising the sum-of-squares error between the parameter prediction and ground truth using a Levenberg-Marquardt optimisation. Training and reconstruction were carried out on a personal computer with an Intel Core i5 − 6500 3.20 GHz processor (Intel, Santa Clara, California, USA) and stopped when 100 iterations were reached.

3.7.3 *Network Input and Output*

After training, the artificial neural network took both the normalised GRE magnitude signal and the magnetic susceptibility from QSM as an input

$$\mathrm{input} = \begin{pmatrix} S(\mathrm{TE}_1)/S(\mathrm{TE}_1) \\ \vdots \\ S(\mathrm{TE}_8)/S(\mathrm{TE}_1) \\ \chi \end{pmatrix} \tag{3.41}$$

and returned

$$\text{output} = \left(Y, R_2, \nu, \chi_{\text{nb}}, S_0/S(\text{TE}_1)\right)^{\text{T}} \quad . \tag{3.42}$$

This was done for every voxel and final OEF maps were calculated according to Equation 3.31.

3.7.4 *Statistics*

Mean values and standard deviations of the reconstructed parameters OEF, ν, R_2, χ_{nb} and S_0 in grey and white matter were calculated for every subject. Intersubject means were used to determine significant differences ($p < 0.05$) between the ANN and QN reconstruction using a two-sample Student's t-test. Bland-Altman plots were used to visually assess correlation and agreement of the two methods.

3.7.5 *Simulation*

A simulation was used in order to assess the accuracy and precision of the ANN. Magnetic susceptibility and magnitude decay in 100 grey and white matter voxels each were simulated exactly as during training with $Y = 60\,\%$, $\nu = 4\,\%$, $R_2 = 12\,\text{Hz}$ and $\chi_{\text{nb}} = -40\,\text{ppb}$ representing grey matter and $Y = 60\,\%$, $\nu = 2\,\%$, $R_2 = 17\,\text{Hz}$ and $\chi_{\text{nb}} = -50\,\text{ppb}$ representing white matter. Additional 100 voxels were simulated with the grey matter parameters except that $Y = 80\,\%$ representing a generic lesion. Only for simulation purposes, two additional networks were trained in the same fashion as the first, yet, with uniform instead of Gaussian parameter distributions constrained by $(1 < Y < 98)\,\%$, $(0.1 < \nu < 10)\,\%$, $(1 < R_2 < 30)\,\text{Hz}$ and $(-100 < \chi_{\text{nb}} < 100)\,\text{ppb}$. One of the additional networks was trained on 10^7 parameter sets randomly chosen from each distribution. For the other one, each parameter range was divided into 60 equidistant steps and all possible combinations $\left(1.296 \cdot 10^7\right)$ were utilised for training. The parameters were reconstructed with all three ANNs and the QN approach and the relative deviation from the ground truth was compared.

3.8 TISSUE OXYGENATION IN HIGH-GRADE GLIOMAS

The brain tissue oxygenation parameters OEF, CBF and CMRO2 were quantified from the GRE data of the eight patients diagnosed with high-grade glioma and the results were compared between glioblastomas and astrocytomas. For this purpose, machine learning was incorporated into the QSM+qBOLD approach presented in Section 3.6 in order to make the reconstruction more robust still. The approach described in the following is a preliminary version of the technique proposed by Cho et al. [2019] and has been published as Hubertus et al. [2019a].

3.8.1 *QSM+qBOLD Analysis*

The GRE data was analysed with the QSM+qBOLD approach as described in Subsection 3.6.2 with ν being initialised according to Equation 3.2 and 3.5 respectively. An additional clustering step was introduced where voxels with similar magnitude decay were grouped together first using the X-means algorithm [Pelleg and Moore, 2000] to determine the number of clusters. The actual clustering was then carried out with the K-means algorithm. The Bayesian information criterion was used as discriminator in both cases. Only one value for Y, ν and R_2 was fitted per group in order to increase the SNR with the starting value being the average of the original starting values within the group. The results of this initial groupwise fit were then used as starting values for the final voxelwise fit. This voxelwise fit was stopped when the relative change of the objective function reached 1 % or after a maximum of 30 iterations. In order to circumvent the determination of the weighting factor in Equation 3.33, χ_{nb} was updated directly from Equation 3.34 and the other parameters from Equation 3.37 in each iteration. CBF was estimated according to Subsection 3.3.1 and 3.3.2 and OEF and CMRO2 were calculated using Equation 3.31 and 3.32 respectively.

3.8.2 *Statistics*

ROIs were drawn around the brain tumours by a neuroradiologist with 7 years of experience. These ROIs were mirrored at the central axis of the brain to also obtain contralateral ROIs. Mean values and standard deviations of the reconstructed oxygenation parameters OEF, CBF and CMRO2 were calculated in both ROIs for glioblastoma and astrocytoma patients separately. Intersubject means were used to determine significant differences ($p < 0.05$) between the tumour and contralateral side using a two-sample Student's t-test. In addition, ROIs were drawn outlining small parts of the contrast-enhancing tumour (CET), oedema (OED), normal appearing grey matter (nGM) and normal appearing white matter (nWM). OEF versus CBF was plotted within these tissue ROIs in order to illustrate possible trends and clusters.

4

RESULTS

This chapter lists and depicts the results of this thesis starting with the general QSM pipeline implemented for this work. Afterwards the results of the three main parts of this thesis are shown: The comparison of the GESSE and GRE sequence for QSM+qBOLD analysis, the application of an artificial neural network for QSM+qBOLD analysis of GRE data and finally the mapping of tissue oxygenation in high-grade glioma patients. The three parts have been published as Hubertus et al. [2019b], Hubertus et al. [2019c] and Hubertus et al. [2019a] respectively and the corresponding descriptions and illustrations are adapted from named publications.

4.1 QSM PIPELINE

Figure 4.1 illustrates one slice of the magnitude and phase images at three different echo times as manually reconstructed from the raw GRE data of one representative healthy volunteer. These images serve as input for the QSM pipeline. The results from each step of the pipeline for a single slice in a representative healthy volunteer are depicted in Figure 4.2. Only little phase wrapping is visible in the anterior left part of the brain, which is fully

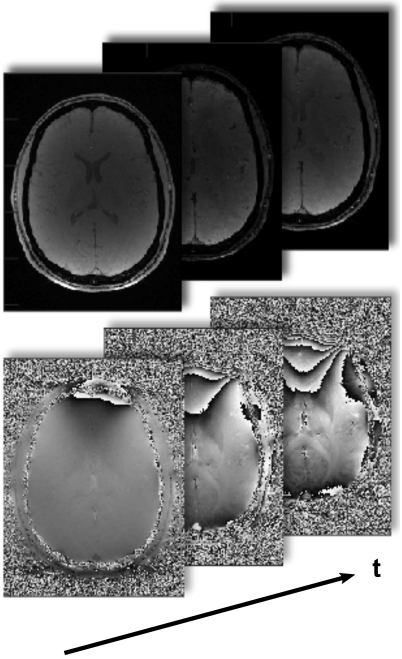

Figure 4.1: Representative slice of the GRE magnitude (top) and phase (bottom) images at three subsequent echo times from a representative healthy volunteer.

removed by the spatial unwrapping. Both the RDF and χ maps reveal grey-white matter contrast. The RDF map shows the non-local characteristics of the dipole, which are removed in the χ map by the field to source inversion.

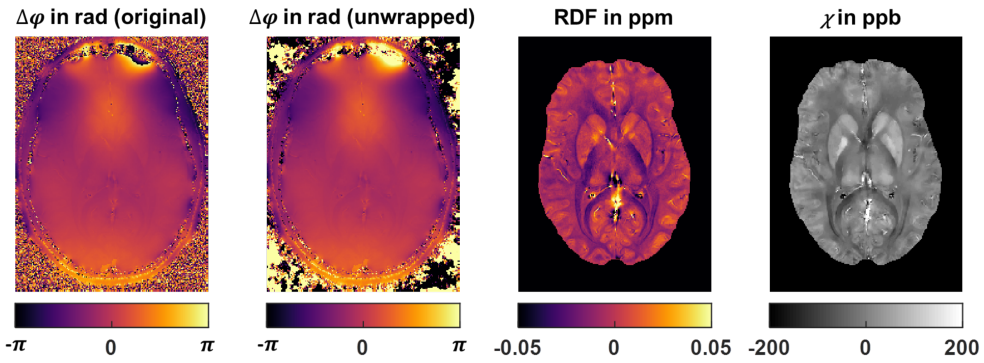

Figure 4.2: In vivo results of the QSM pipeline applied to the GRE data of a representative healthy volunteer. Depicted are the estimated frequency offset per echo $\Delta\varphi$ before and after spatial unwrapping as well as the relative difference field RDF $= \Delta\varphi_{\text{loc}}/(\omega_0 \Delta\text{TE})$ in ppm and the magnetic susceptibility χ referenced to CSF in ppb. The RDF and χ outside the brain mask are manually set to black.

4.2 COMPARISON OF GESSE AND GRE FOR QSM+qBOLD ANALYSIS

Figure 4.3 depicts the L-curve for one representative subject both for the GESSE and GRE sequence. The optimal weighting factor according to L-curve theory was either 1 or 10 for all subjects.

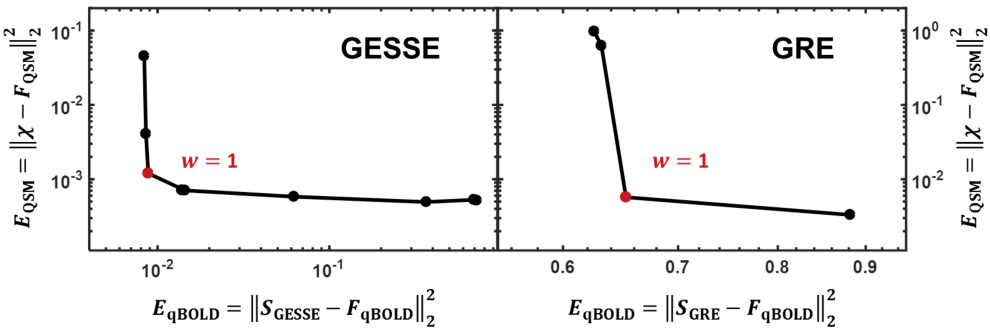

Figure 4.3: Choosing the weighting factor: L-curve analysis comparing QSM against qBOLD term for one representative subject for GESSE (left) and GRE (right). $w = 1$ (marked in red) was chosen as optimal weighting according to L-curve theory in both cases.

The ratio of the relative condition numbers $\text{rCN}_{\text{GESSE}}/\text{rCN}_{\text{GRE}}$ is illustrated in Figure 4.4. It is smaller than 1 for all tested OEF and ν with a mean of 0.69. The smallest ratio is reached for low OEF and high ν values.

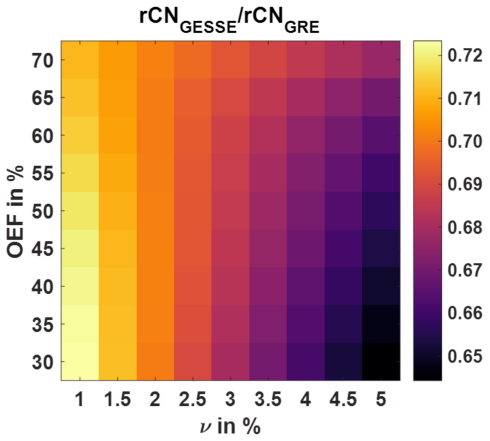

Figure 4.4: Ratio of the relative condition number rCN of the qBOLD function F_{qBOLD} from GESSE and GRE for a range of oxygen extraction fraction (OEF) and deoxygenated blood volume ν. The other parameters were set to $R_2 = 11.5\,\text{Hz}$, $\chi_{\text{nb}} = \chi_{\text{ba}} + 100\,\text{ppb}$, $S_0 = 1000\,\text{a.u.}$ and TE was adopted from the clinical sequence respectively.

A representative slice of the relative deviation of the reconstructed parameters OEF, deoxygenated blood volume ν and transverse relaxation rate R_2 from the GESSE and GRE single- and multi-compartment simulation is shown in Figure 4.5. For the single-compartment simulation, the OEF and ν from GESSE

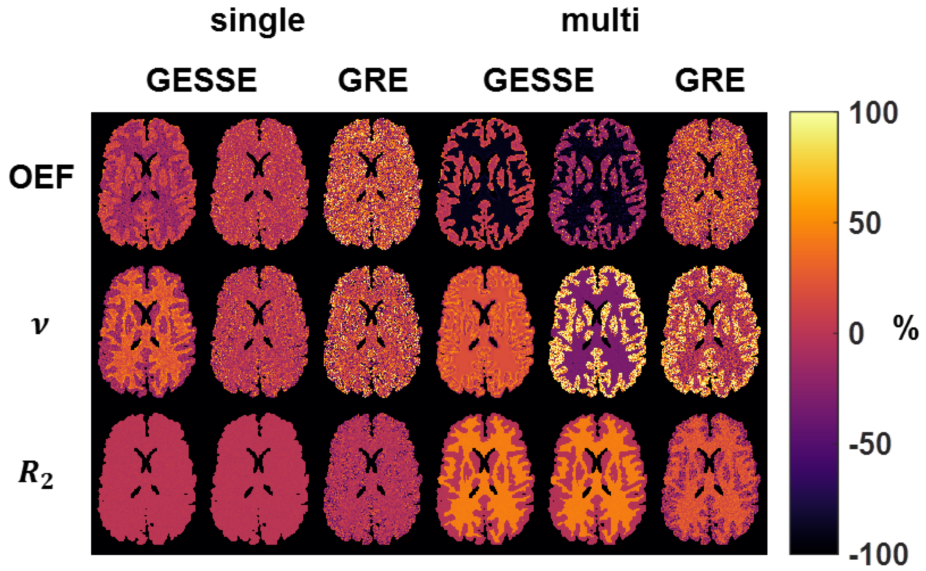

Figure 4.5: Relative deviation from ground truth $(x - x_{\text{true}})/x_{\text{true}} \cdot 100\,\%$ of reconstructed oxygen extraction fraction (OEF), deoxygenated blood volume ν and transverse relaxation rate R_2. Representative slice from GESSE and GRE for the single-compartment (left) and multi-compartment simulation (right). The GESSE reconstruction has been initialised with the single mean value of ground truth ν (first column) and the actual ground truth ν distribution (second column).

reveal less variation within one tissue type but stronger contrast between grey and white matter compared to GRE. When initialising the GESSE reconstruction with the ground truth ν distribution, the grey-white matter contrast is reduced. R_2 reconstructed from GESSE is more accurate in grey and white matter and shows no contrast in both cases. For the multi-compartment simulation, all three parameters from GESSE have again lower variation within one tissue type. OEF is slightly overestimated in grey and white matter for GRE and strongly underestimated in white matter for GESSE. Initialising the GESSE reconstruction with the ground truth ν distribution in this case increases the discrepancy between grey and white matter for ν.

Table 4.1: Mean relative squared error MRSE $= \overline{((x - x_{\text{true}})/x_{\text{true}})^2}$ of the reconstructed oxygen extraction fraction (OEF), deoxygenated blood volume ν, transverse relaxation rate R_2, non-blood magnetic susceptibility χ_{nb} and magnitude S_0 across the whole simulated grey matter (GM) and white matter (WM) for GESSE and GRE. The GESSE reconstruction has been initialised with the single mean value of ground truth ν (first column) and the actual ground truth ν distribution (second column). Upper half shows results for single-, lower half for multi-compartment simulation. The R_2 component of brain tissue was used as ground truth in the multi-compartment case.

MRSE in %		GM			WM		
		GESSE		GRE	GESSE		GRE
single	OEF	3	6	30	5	3	15
	ν	4	9	32	10	2	8
	R_2	0.04	0.04	7	0.05	0.04	0.8
	χ_{nb}	0.8	0.2	6	0.1	0.1	0.6
	S_0	0.00	0.00	0.03	0.00	0.00	0.01
multi	OEF	2	7	12	82	84	16
	ν	6	82	57	8	10	6
	R_2	0.08	0.1	7	19	19	5
	χ_{nb}	1	3	8	3	3	0.5
	S_0	0.00	0.00	0.03	0.01	0.01	0.03

Table 4.1 summarises the accuracy (MRSE) of all parameters reconstructed from GESSE and GRE across grey and white matter in the full brain for the single- and multi-compartment simulation. The accuracy of the GESSE parameters is generally higher than of the GRE parameters in the single-compartment case except for ν in white matter (10 % versus 8 %). Initialisation of the GESSE reconstruction with the ground truth ν distribution leads to a decreased accuracy of OEF and ν in grey matter but an increased accuracy in white matter compared to the single value initialisation. In the multi-compartment case, the GESSE accuracy of OEF (2 % versus 12 %), ν (6 % versus 57 %) and R_2 (0.08 % versus 7 %) in grey matter is higher than for GRE when the former is initial-

ised with single value ν. The opposite holds for white matter OEF (82 % versus 16 %), ν (8 % versus 6 %) and R_2 (19 % versus 5 %). Initialisation of the GESSE reconstruction with the ν distribution does not improve accuracy of OEF, ν and R_2 in white matter and lowers it in grey matter.

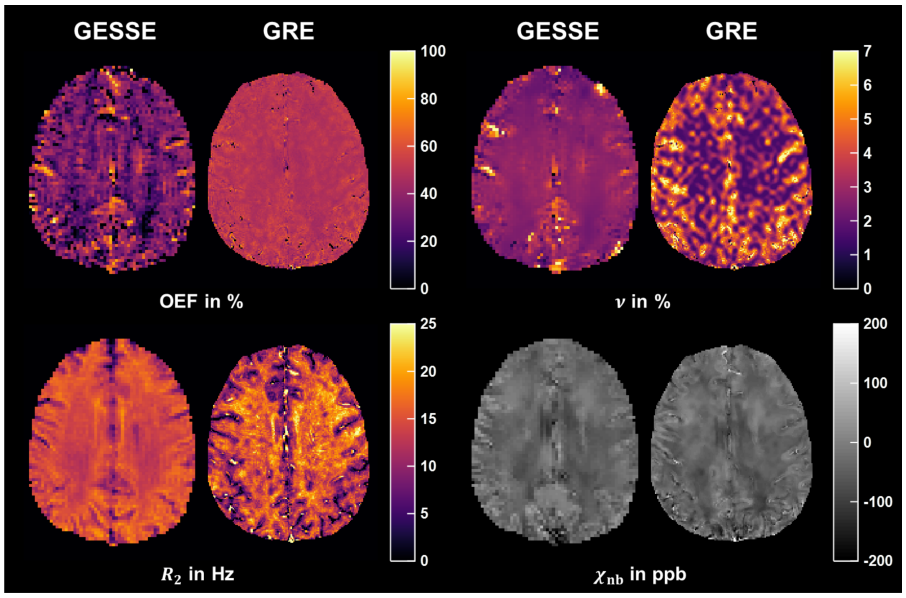

Figure 4.6: Similar representative slice of the reconstructed parameter maps from GESSE (left) and GRE (right) for subject 2: oxygen extraction fraction (OEF), deoxygenated blood volume ν, transverse relaxation rate R_2 and non-blood magnetic susceptibility χ_{nb}.

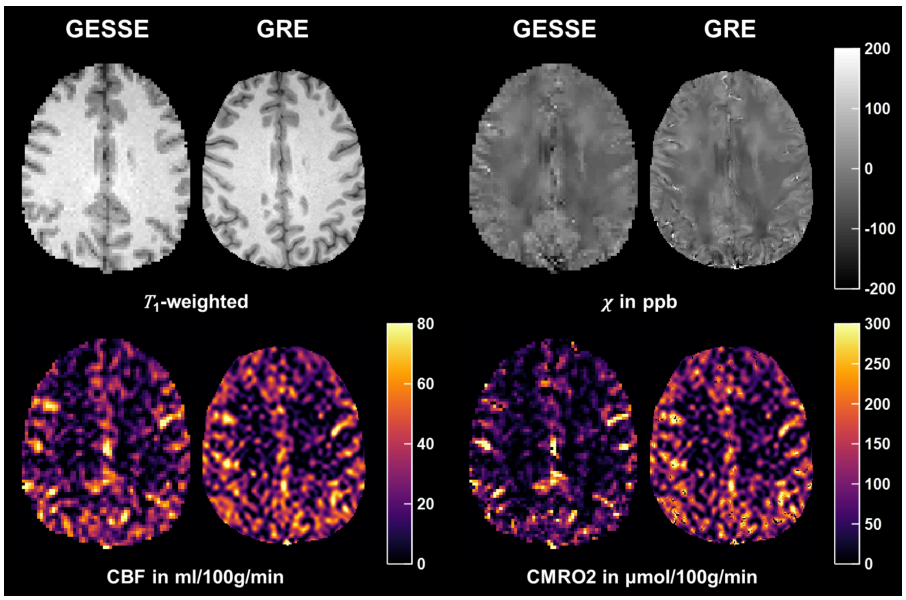

Figure 4.7: T_1-weighted image, map of the magnetic susceptibility χ, cerebral blood flow (CBF) and cerebral metabolic rate of oxygen (CMRO2) registered to the GESSE (left) and GRE data (right). Depicted is the same slice as in Figure 4.6.

Figure 4.6 illustrates a similar representative slice from GESSE and GRE of the reconstructed parameters OEF, ν, R_2 and χ_{nb}. Figure 4.7 shows the same two slices depicting the morphological reference T_1-weighted image, input parameter maps of χ and CBF as well as the resulting CMRO2 map.

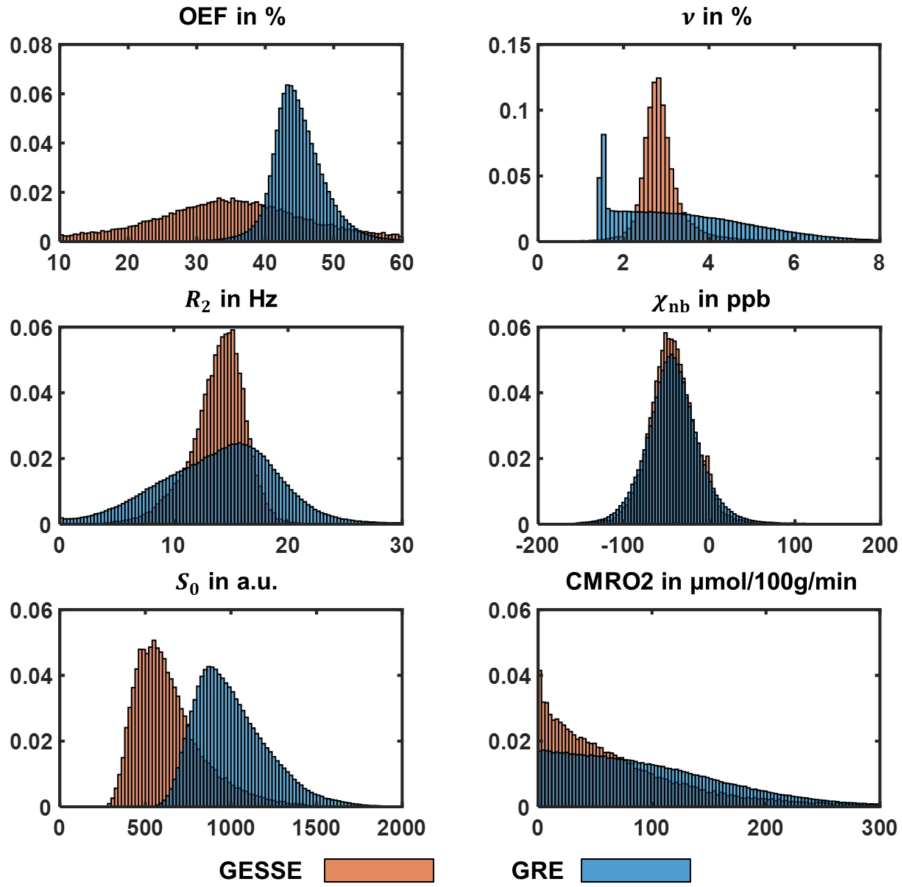

Figure 4.8: Histograms showing the parameter distribution across grey and white matter for both GESSE (orange) and GRE (blue) of subject 6. Shown are the oxygen extraction fraction (OEF), deoxygenated blood volume ν, transverse relaxation rate R_2, non-blood susceptibility χ_{nb}, signal magnitude at the spin echo and $t = 0$ respectively S_0 and cerebral metabolic rate of oxygen (CMRO2).

Histograms of the reconstructed GESSE and GRE parameters across GM+WM of subject 6 are depicted in Figure 4.8. Mean and standard deviation in this case are OEF $= 35.0 \pm 15.4\,\%$, $\nu = 2.8 \pm 0.5\,\%$ (median $\pm$ interquartile range), $R_2 = 13.8 \pm 2.5\,\mathrm{Hz}$, $\chi_{\mathrm{nb}} = -43 \pm 27\,\mathrm{ppb}$, $S_0 = 639 \pm 199\,\mathrm{a.u.}$ and CMRO2 $= 66 \pm 73\,\mu\mathrm{mol}/100\,\mathrm{g}/\mathrm{min}$ for GESSE and OEF $= 44.9 \pm 5.0\,\%$, $\nu = 3.2 \pm 2.4\,\%$ (median $\pm$ interquartile range), $R_2 = 14.1 \pm 6.2\,\mathrm{Hz}$, $\chi_{\mathrm{nb}} = -42 \pm 36\,\mathrm{ppb}$, $S_0 = 1006 \pm 216\,\mathrm{a.u.}$ and CMRO2 $= 89 \pm 82\,\mu\mathrm{mol}/100\,\mathrm{g}/\mathrm{min}$ for GRE. The OEF distribution is broader for GESSE than for GRE with the opposite being true for ν and R_2. χ_{nb}, S_0 and CMRO2 have similar distributions for GESSE and GRE. ν from GRE reveals a cutoff at roughly 1.2 %.

Table A.1 and A.2 in the Appendix A summarise the mean values and standard deviations of OEF, CMRO2, CBF, ν, R_2 and χ_{nb} for all seven subjects from GESSE and GRE respectively.

Table 4.2 highlights the intersubject variability by listing the mean and standard deviation of the individual means for the same six parameters from GESSE and GRE together with the p-value for the comparison of both sequences. Averaged over grey and white matter, there are significant differences ($p < 0.05$) between GESSE and GRE for the OEF (32.4 ± 1.6 versus 43.0 ± 5.4 %), CMRO2 (60 ± 15 versus 87 ± 13 µmol/100 g/min) and ν (2.9 ± 0.1 versus 3.5 ± 0.4 %). Looking at grey and white matter separately, there are also significant differences between GESSE and GRE for the OEF, R_2 and CMRO2 both in grey and white matter and for ν only in grey matter.

Table 4.2: Intersubject variability given by the mean $\pm$ standard deviation of the individual means for the oxygen extraction fraction (OEF), cerebral metabolic rate of oxygen (CMRO2), cerebral blood flow (CBF), deoxygenated blood volume ν, transverse relaxation rate R_2 and non-blood magnetic susceptibility χ_{nb} for GESSE and GRE. Means were calculated within combined grey and white matter (GM+WM) as well as in grey matter (GM) and white matter (WM) separately. p-values from Student's t-test are stated to determine significant differences ($p < 0.05$) between the values from GESSE and GRE.

	GM+WM	GM	WM	GM+WM	GM	WM
	OEF in %			CMRO2 in µmol/100 g/min		
GESSE	32.4 ± 1.6	35.0 ± 0.9	30.3 ± 2.1	60 ± 15	91 ± 24	36 ± 9
GRE	43.0 ± 5.4	43.8 ± 5.2	42.2 ± 5.6	87 ± 13	118 ± 21	56 ± 6
p	< 0.001	< 0.001	< 0.001	< 0.01	< 0.05	< 0.001
	CBF in ml/100 g/min			ν in %		
GESSE	23.8 ± 5.8	34.0 ± 9.0	15.7 ± 3.8	2.9 ± 0.1	3.0 ± 0.1	2.8 ± 0.1
GRE	27.3 ± 5.6	36.8 ± 8.5	17.7 ± 3.7	3.5 ± 0.4	4.3 ± 0.6	2.8 ± 0.3
p	0.27	0.56	0.34	< 0.01	< 0.001	0.81
	R_2 in Hz			χ_{nb} in ppb		
GESSE	14.2 ± 0.5	13.4 ± 0.5	14.8 ± 0.6	-43 ± 5	-36 ± 5	-49 ± 7
GRE	14.4 ± 0.7	12.0 ± 0.8	16.9 ± 0.7	-43 ± 8	-40 ± 8	-46 ± 9
p	0.53	< 0.01	< 0.001	0.87	0.28	0.43

Figure 4.9 depicts a boxplot of the subject means of OEF, CMRO2, ν, R_2 and χ_{nb} from GESSE and GRE across grey and white matter, and grey matter and white matter separately. Significant contrast ($p < 0.05$) between grey and white matter is present for all five parameters from GESSE but only for CMRO2, ν and R_2 from GRE.

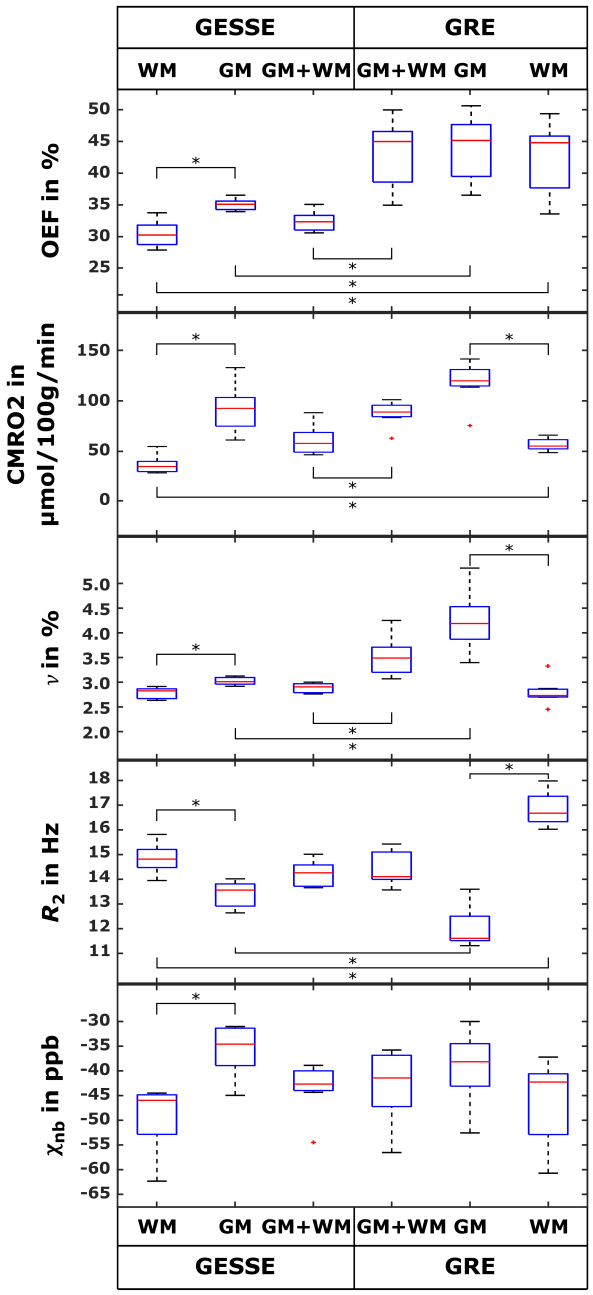

Figure 4.9: Boxplot illustrating intersubject variability for the oxygen extraction fraction (OEF), cerebral metabolic rate of oxygen (CMRO2), deoxygenated blood volume ν, transverse relaxation rate R_2 and non-blood magnetic susceptibility χ_{nb} for GESSE and GRE across combined grey and white matter (GM+WM) and grey matter (GM) and white matter (WM) separately. Depicted are median (red), first and third quartile (blue) and whiskers at 1.5 times the interquartile distance (black). Significant differences ($p < 0.05$) both between GM and WM within the same acquisition and between GESSE and GRE within the same tissue are marked with an asterisk.

The GESSE and GRE signal decay from a representative voxel in grey and white matter, together with the corresponding fit and residuals are illustrated in Figure 4.10. The residuals of the grey matter voxel seem randomly distributed. The white matter residuals show a peak at the spin echo for GESSE and a linear drop during the first four echoes for the GRE. Figure 4.11 shows a representative inferior slice of OEF and ν reconstructed from GESSE together with the corresponding magnitude image at the last echo and the magnetic susceptibility. Artefacts of increased OEF and ν are visible in the centre and left anterior part of the brain, which roughly coincide with the caudate nucleus, putamen, and globus pallidus outlined in blue and signal dropout in the magnitude image outlined in green.

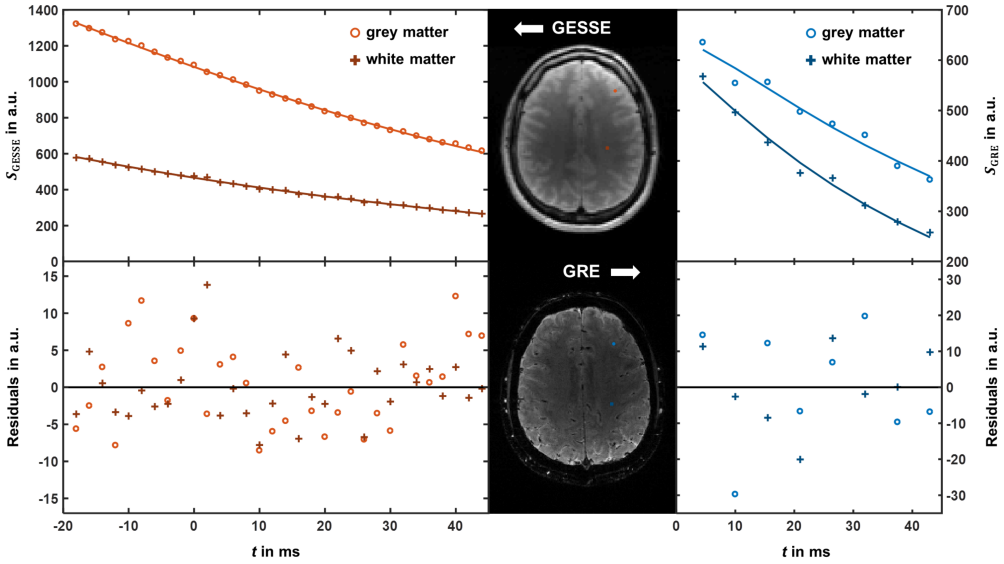

Figure 4.10: Comparison of two representative voxels in grey and white matter including signal decay, fit and residuals for GESSE (orange, left) and GRE (blue, right) signal in vivo.

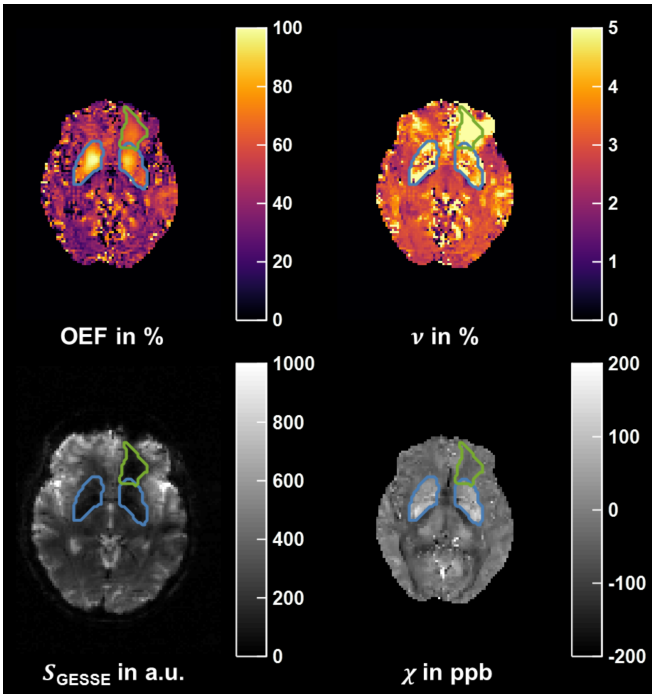

Figure 4.11: Representative inferior slice of the oxygen extraction fraction (OEF) and deoxygenated blood volume ν reconstructed from GESSE with the corresponding magnitude image at the last echo S_{GESSE} and magnetic susceptibility χ. The green ROI was drawn around the area of signal dropout in the magnitude image and the blue ROI outlines the caudate nucleus, putamen and globus pallidus on the magnetic susceptibility image. Artefacts of increased OEF and ν are visible in both areas.

4.3 ARTIFICIAL NEURAL NETWORKS FOR QSM+qBOLD ANALYSIS

The training of the ANN stopped after 100 iterations taking 62 minutes with the chosen hardware. The reconstruction time for a full in vivo data set with the ANN is approximately one second compared to approximately one hour with the QN approach even excluding the calculation of the L-curve.

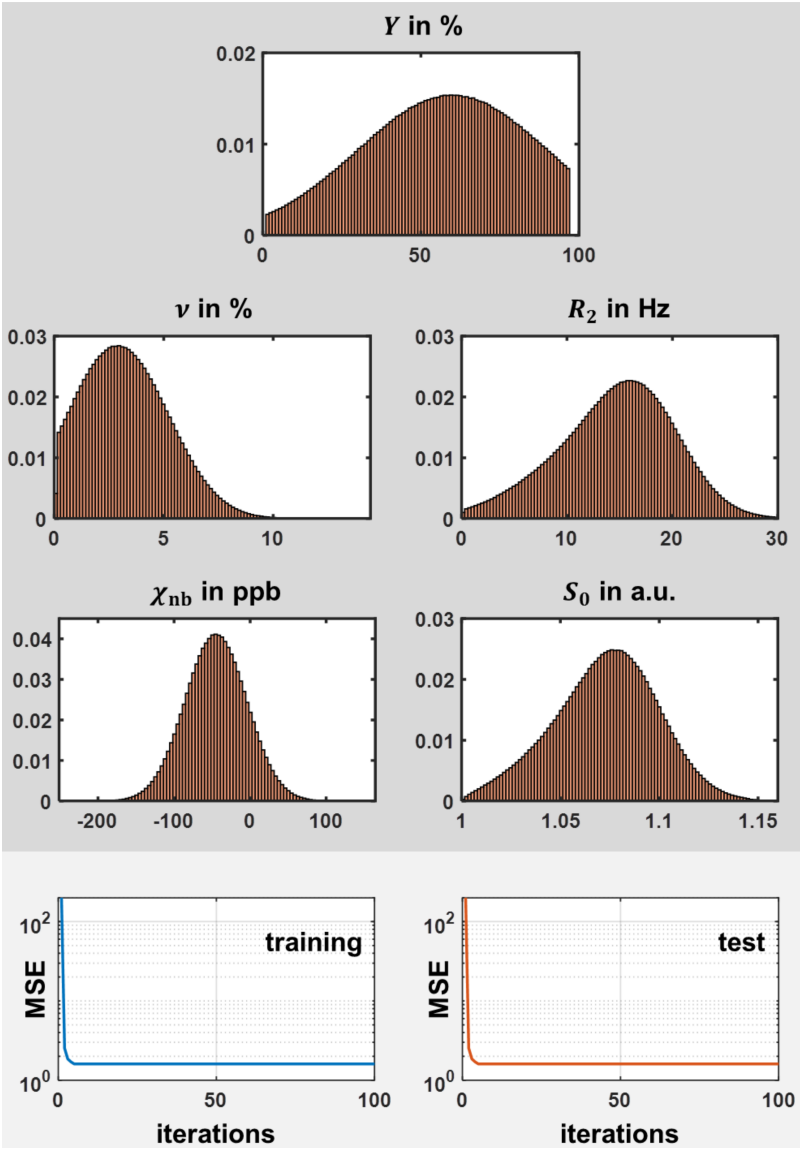

Figure 4.12: Normalised histograms of training parameters (top) and training performance of the network (bottom). The training distributions of the venous oxygen saturation Y, deoxygenated blood volume ν, transverse relaxation rate R_2, non-blood magnetic susceptibility χ_{nb} and magnitude after excitation S_0 comprise both grey and white matter. The maximum Y is cut off at the assumed arterial oxygen saturation $Y_{\mathrm{a}} = 98\,\%$. The performance of the network is measured by the mean squared error (MSE) and starts stagnating after approximately 10 iterations both for the training (left) and testing set (right).

Figure 4.12 depicts the distributions of the parameters Y, R_2, ν, χ_{nb} and S_0 that were used for training the ANN as normalised histograms and the evolution of the ANN performance during training.

The accuracy of the parameter reconstruction in the simulation for the three ANNs and the QN approach is displayed in Figure 4.13. Averaged over all simulated voxels, the ANN trained on normally distributed parameters is more accurate than the ones trained on uniformly distributed parameters and has lower variation than the QN approach. The uniformly trained ANNs specifically overestimate ν in simulated WM.

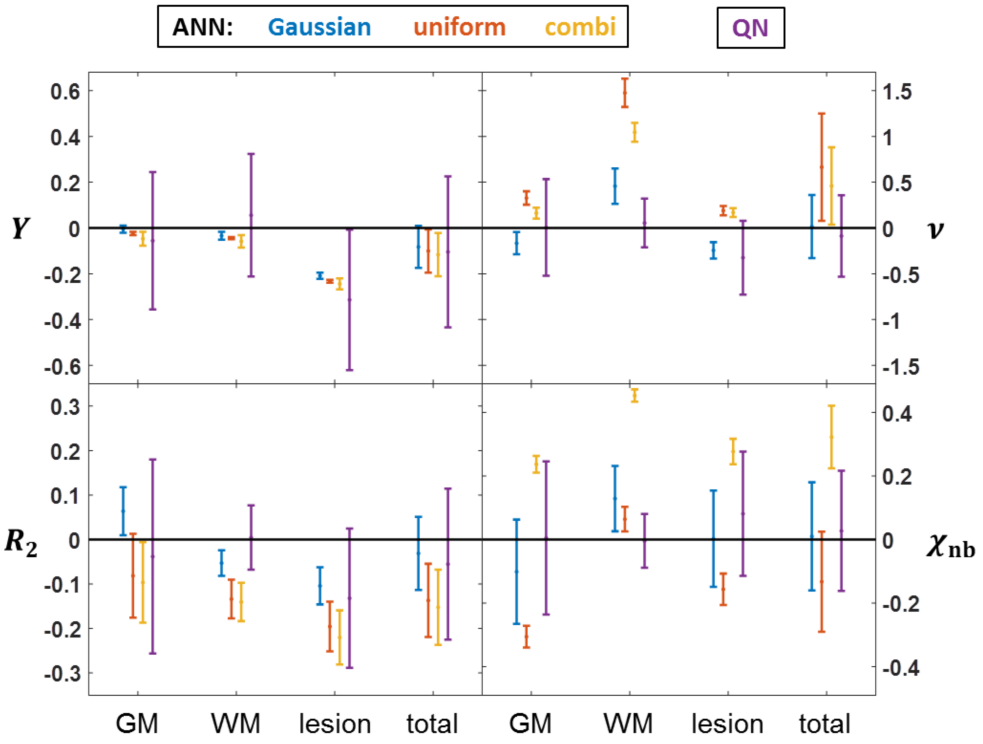

Figure 4.13: Mean and standard deviation of the relative accuracy $(x_{rec} - x_{true})/x_{true}$ for the reconstructed venous oxygen saturation Y, deoxygenated blood volume ν, transverse relaxation rate R_2 and non-blood magnetic susceptibility χ_{nb}. The performance of the ANN with the Gaussian (blue), uniform (orange) and combinatorial (yellow) training parameter distribution as well as of the QN approach (purple) is displayed within all simulated voxels (total) and within grey matter (GM), white matter (WM) and the lesion separately.

Figure 4.14 shows a representative axial, coronal and sagittal slice of the reconstructed OEF from the ANN and QN approach from one subject. The corresponding T_1-weighted image is given as morphological reference. Stronger contrast between grey and white matter is visible in the ANN reconstruction.

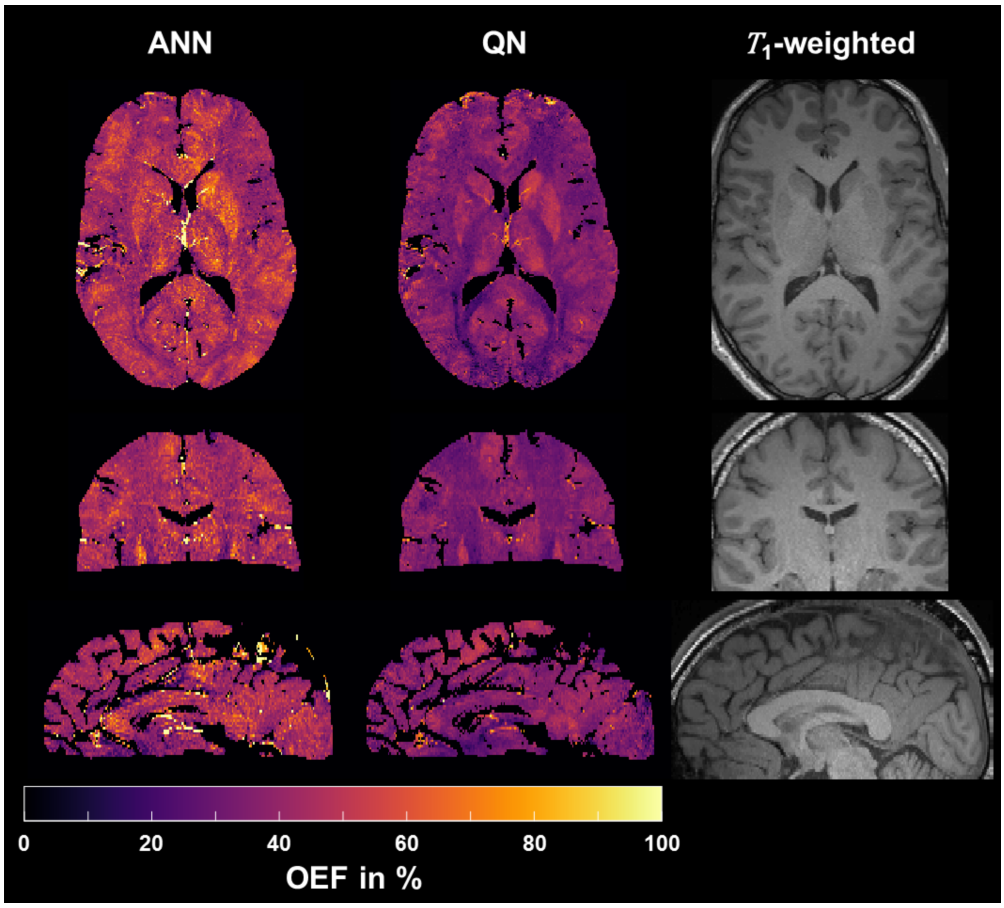

Figure 4.14: Representative axial, coronal and sagittal slice of the oxygen extraction fraction OEF $= 1 - Y/Y_a$ reconstructed with the artificial neural network (ANN) and quasi-Newton (QN) approach. The corresponding T_1-weighted morphological reference image is given on the right.

The same axial slice of the remaining parameters ν, R_2, χ_{nb} and S_0 for the ANN and QN reconstruction as well as the corresponding ν_{start} and χ map from QSM are illustrated in Figure 4.15. The parameter maps from the ANN generally appear noisier than the ones from the QN approach.

Figure 4.16 shows the distribution of all reconstructed parameters across the full brain of the same subject as normalised histograms. Mean values $\pm$ standard deviations in grey matter are OEF $= 44.1 \pm 9.9\,\%$, $\nu = 3.3 \pm 1.9\,\%$, $R_2 = 13.4 \pm 3.5\,\text{Hz}$, $\chi_{nb} = -17 \pm 38\,\text{ppb}$, $S_0 = 1234 \pm 286\,\text{a.u.}$ for the ANN and OEF $= 36.5 \pm 7.5\,\%$, $\nu = 5.2 \pm 2.1\,\%$, $R_2 = 12.2 \pm 5.1\,\text{Hz}$, $\chi_{nb} = -34 \pm 33\,\text{ppb}$, $S_0 = 1209 \pm 286\,\text{a.u.}$ for the QN approach. The values in white matter are OEF $= 46.8 \pm 9.1\,\%$, $\nu = 2.4 \pm 1.4\,\%$, $R_2 = 16.6 \pm 2.4\,\text{Hz}$, $\chi_{nb} = -34 \pm 28\,\text{ppb}$, $S_0 = 1136 \pm 236\,\text{a.u.}$ for the ANN and OEF $= 33.7 \pm 6.2\,\%$, $\nu = 3.4 \pm 1.6\,\%$, $R_2 = 16.6 \pm 3.1\,\text{Hz}$, $\chi_{nb} = -42 \pm 28\,\text{ppb}$, $S_0 = 1117 \pm 240\,\text{a.u.}$ for the QN approach.

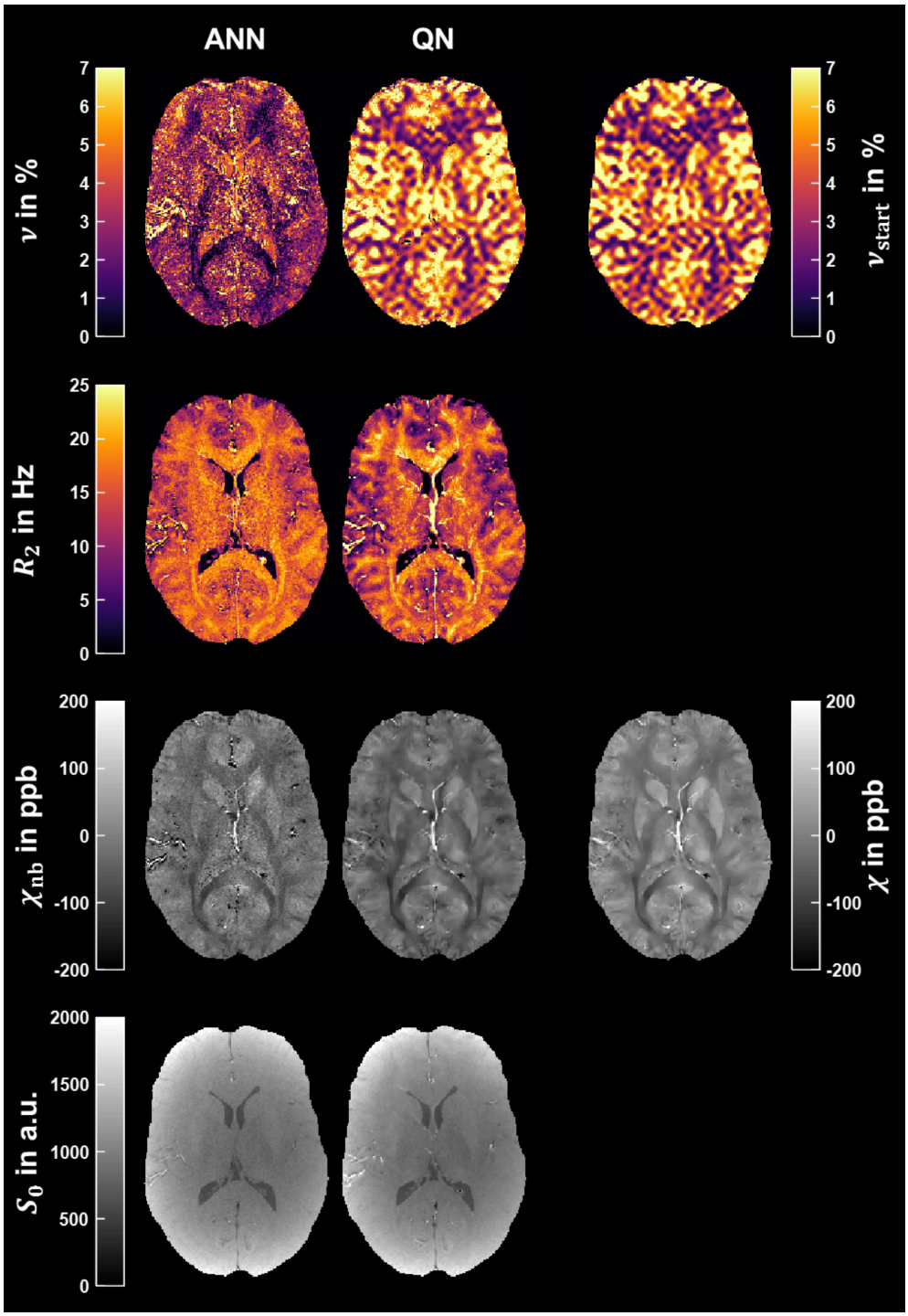

Figure 4.15: Representative axial slice of the deoxygenated blood volume ν, transverse relaxation rate R_2, non-blood magnetic susceptibility χ_{nb} and magnitude after excitation S_0 reconstructed using the artificial neural network (ANN) and quasi-Newton (QN) method. The corresponding slice of ν_{start} used for initialisation and the magnetic susceptibility χ from QSM used for the final QN fit are pictured on the right. The axial slice is the same as in Figure 4.14.

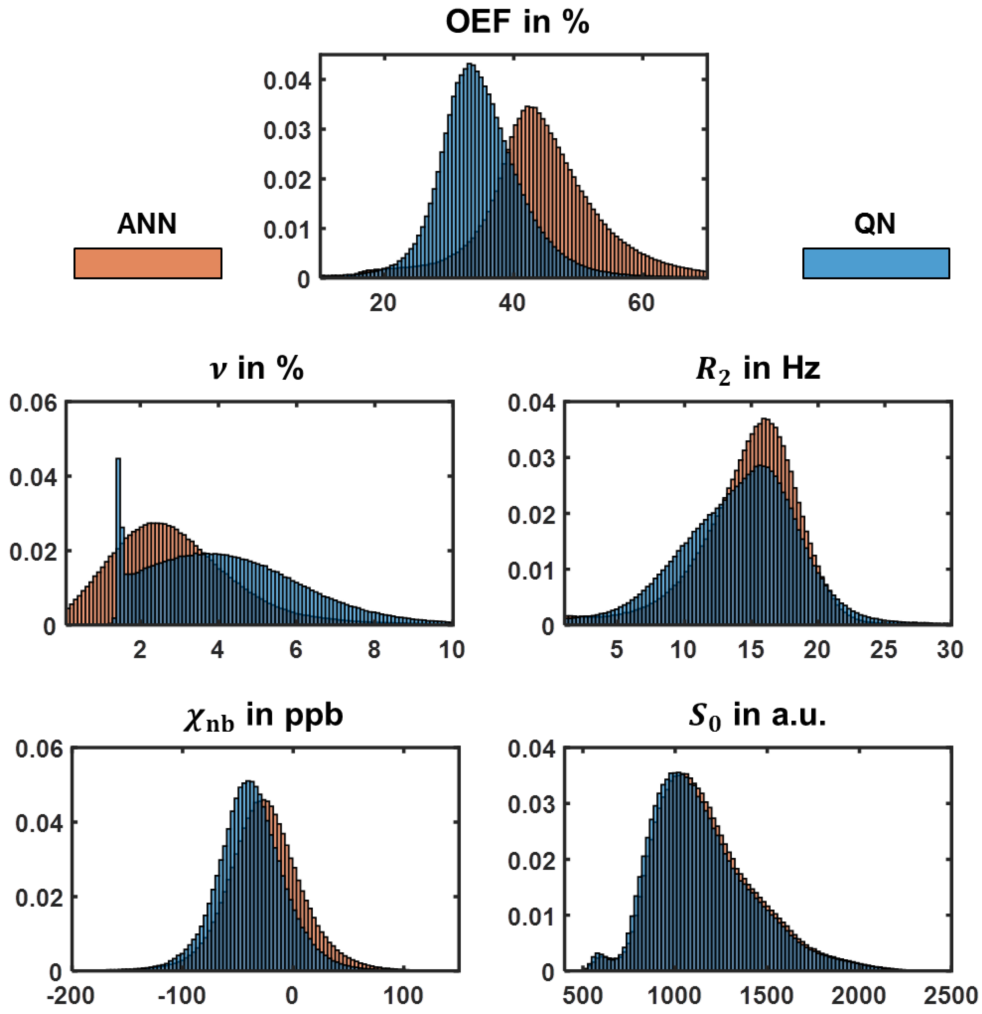

Figure 4.16: Normalised histograms across grey and white matter of the oxygen extraction fraction OEF $= 1 - Y/Y_a$, deoxygenated blood volume ν, transverse relaxation rate R_2, non-blood magnetic susceptibility χ_{nb} and magnitude after excitation S_0 reconstructed from a representative subject (Figure 4.14 and 4.15) using the artificial neural network (orange) and quasi-Newton (blue) approach.

Boxplots of the mean reconstructed parameter values for each subject are depicted in Figure 4.17. Mean $\pm$ standard deviation of the individual subject means in grey and white matter from the ANN and QN reconstruction together with the corresponding p-values are listed in Table 4.3. Significant differences ($p < 0.05$) between ANN and QN were detected for OEF in white matter, for R_2 in grey matter, for ν both in grey and white matter and for χ_{nb} in grey matter.

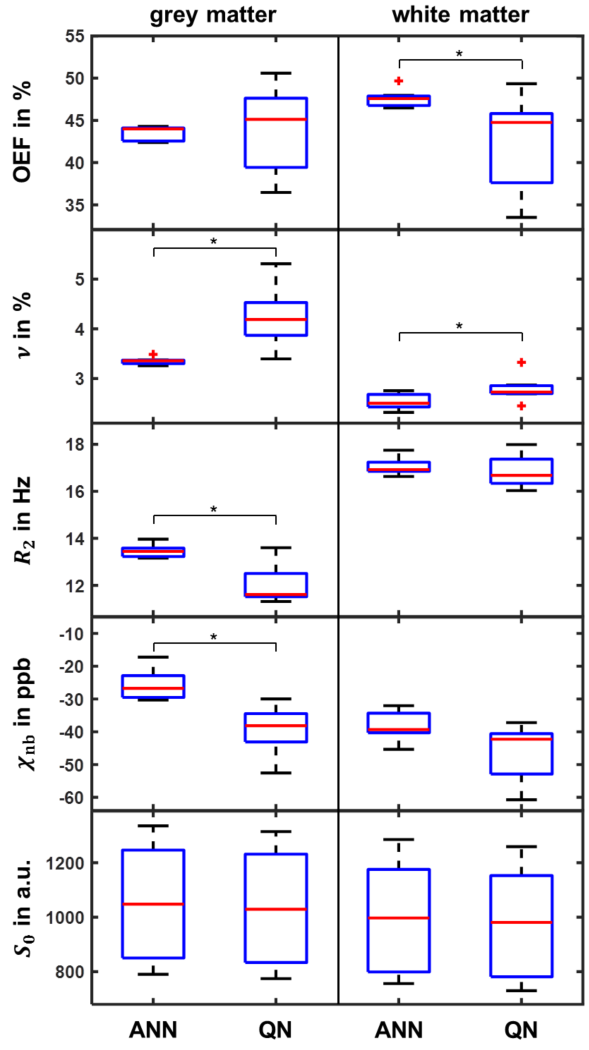

Figure 4.17: Boxplot illustrating intersubject variability within grey (left) and white matter (right) for the oxygen extraction fraction OEF $= 1 - Y/Y_a$, deoxygenated blood volume ν, transverse relaxation rate R_2, non-blood magnetic susceptibility χ_{nb} and magnitude after excitation S_0 reconstructed using the artificial neural network (ANN) and quasi-Newton (QN) method. Depicted are median (red), first and third quartile (blue) and whiskers at 1.5 times the interquartile distance (black). Significant differences ($p < 0.05$) between the ANN and QN approach are marked with an asterisk.

Bland-Altman plots comparing the ANN and QN approach for all reconstructed parameters in grey and white matter from all subjects are illustrated in Figure 4.18. A negative linear trend and distinct grey and white matter cluster are visible for OEF, ν and R_2. The mean difference is compatible with 0 within $\pm 1.96 \cdot$ standard deviations for all parameters except S_0.

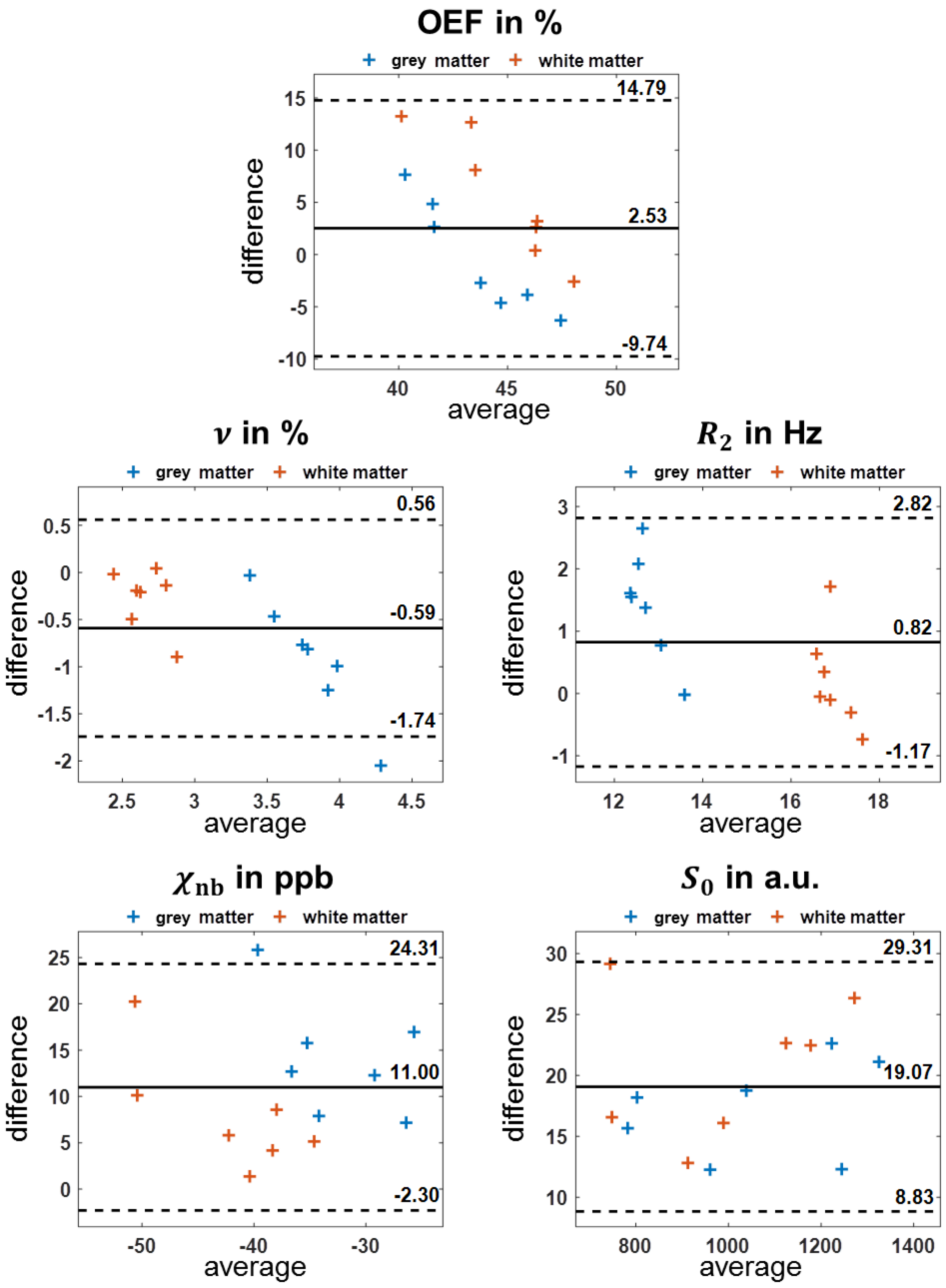

Figure 4.18: Bland-Altman plots comparing artificial neural network (ANN) and quasi-Newton (QN) approach for the oxygen extraction fraction OEF $= 1 - Y/Y_a$, deoxygenated blood volume ν, transverse relaxation rate R_2, non-blood magnetic susceptibility χ_{nb} and magnitude after excitation S_0 within grey (blue) and white matter (orange) in all seven subjects. Plotted are difference $= x_{ANN} - x_{QN}$ over average $= (x_{ANN} + x_{QN})/2$ as well as the mean (solid black line) and mean $\pm\, 1.96 \cdot$ standard deviation (dashed black lines).

Table 4.3: Intersubject variability given by the mean ± standard deviation of the individual means for the oxygen extraction fraction OEF $= 1 - Y/Y_a$, deoxygenated blood volume ν, transverse relaxation rate R_2, initial magnitude S_0 and non-blood magnetic susceptibility χ_{nb} reconstructed with the ANN and QN approach. Means were calculated within grey matter (GM) and white matter (WM) separately. p-values from Student's t-test are stated to determine significant differences ($p < 0.05$) between the values from ANN and QN.

	GM	WM	GM	WM	GM	WM
	OEF in %		ν in %		R_2 in Hz	
ANN	43.5 ± 0.8	47.5 ± 1.1	3.4 ± 0.1	2.5 ± 0.2	13.5 ± 0.3	17.1 ± 0.4
QN	43.8 ± 5.2	42.2 ± 5.6	4.3 ± 0.6	2.8 ± 0.3	12.0 ± 0.8	16.9 ± 0.7
p	0.87	< 0.05	< 0.001	0.48	< 0.01	< 0.05
	S_0 in a.u.		χ_{nb} in ppb			
ANN	1062 ± 218	1006 ± 207	-25 ± 5	-38 ± 5		
QN	1045 ± 217	985 ± 206	-40 ± 8	-46 ± 9		
p	0.88	0.85	< 0.01	0.05		

4.4 TISSUE OXYGENATION IN HIGH-GRADE GLIOMAS

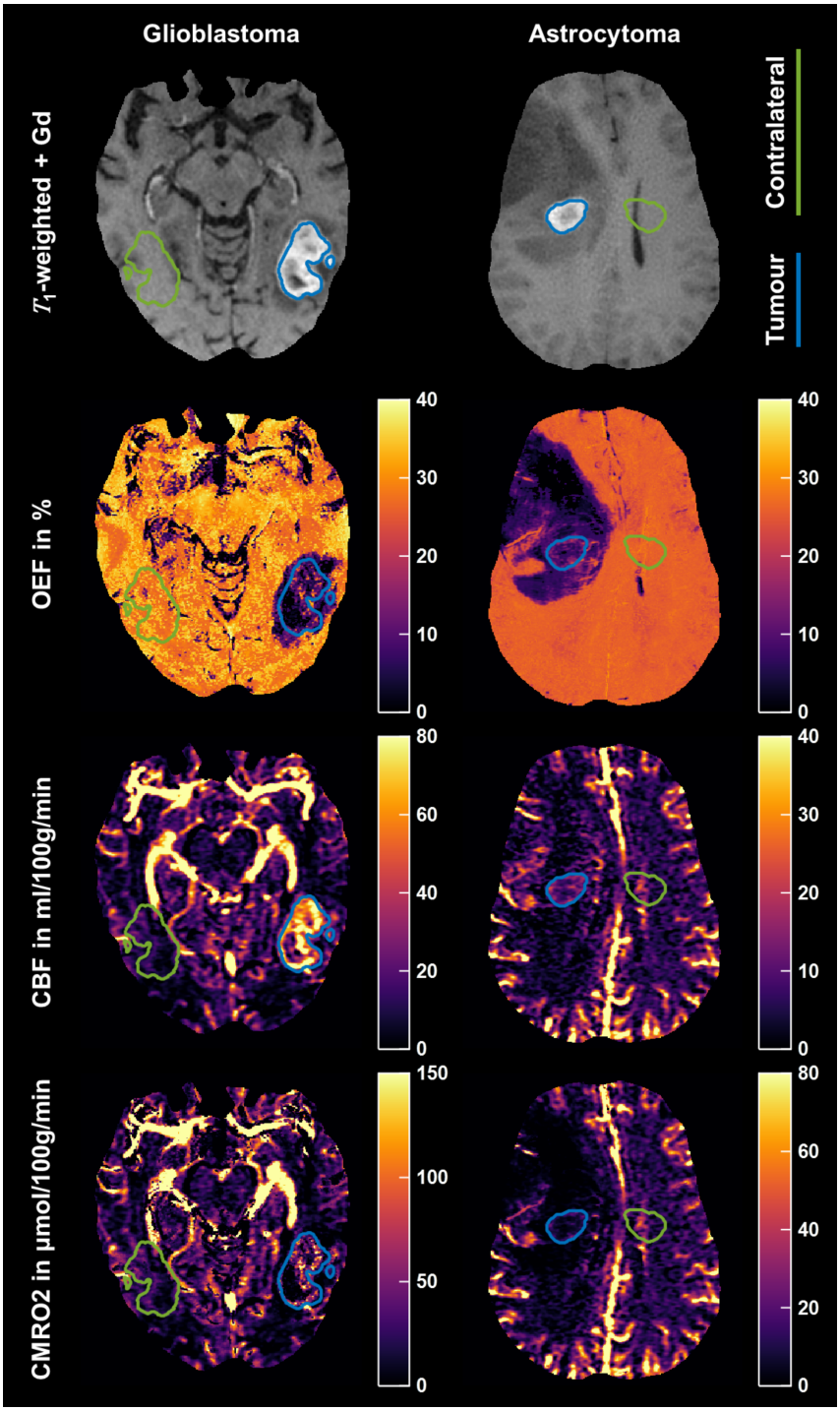

Figure 4.19: Representative slice of the oxygen extraction fraction (OEF), cerebral blood flow (CBF) and cerebral metabolic rate of oxygen (CMRO2) for one glioblastoma (left) and astrocytoma patient (right) together with the corresponding T_1-weighted image with gadolinium (Gd) contrast agent. The tumour ROI and its contralateral side are outlined in blue and green respectively.

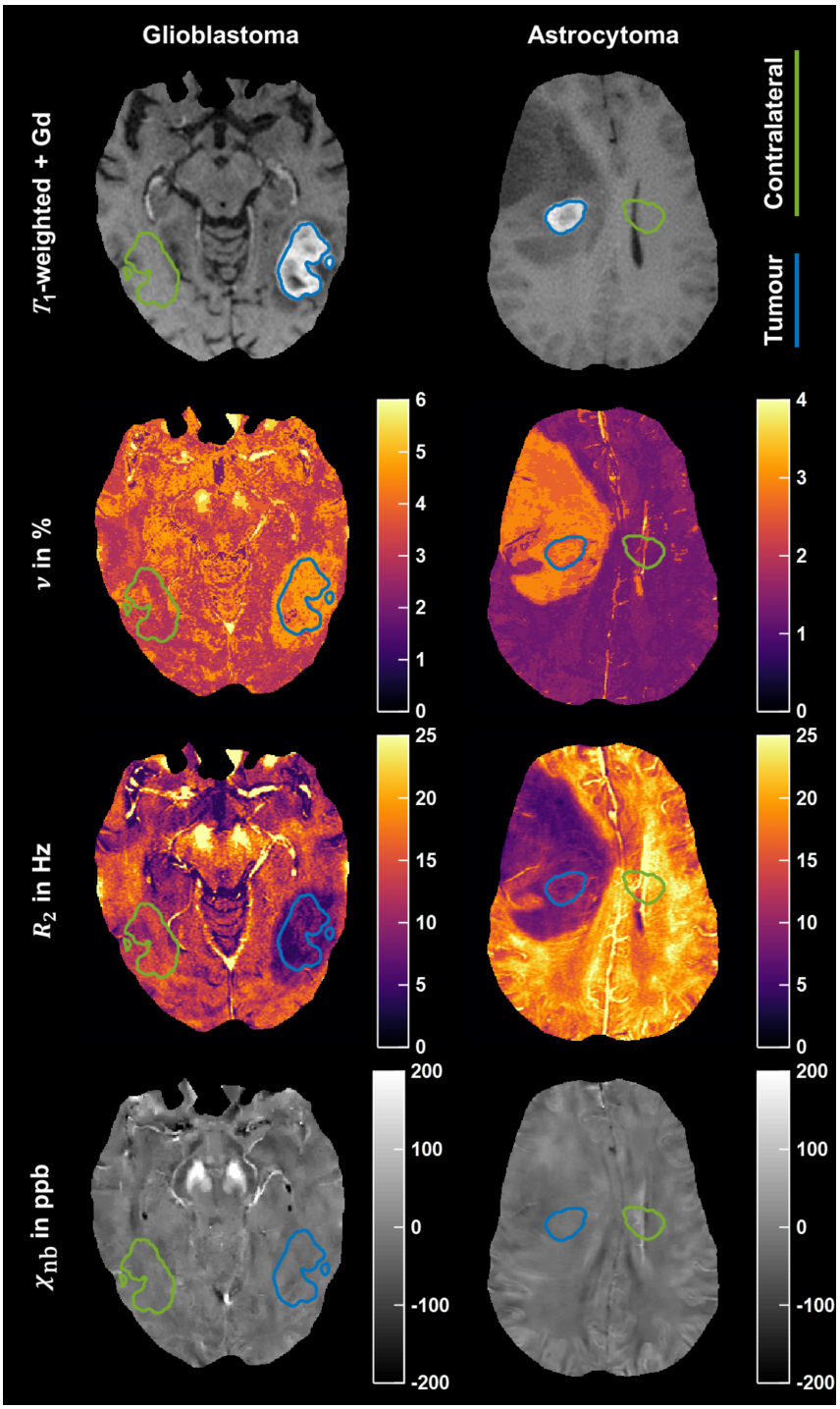

Figure 4.20: Maps of the deoxygenated blood volume ν, transverse relaxation rate R_2 and non-blood magnetic susceptibility χ_{nb} in the same representative slice of the glioblastoma (left) and astrocytoma patient (right) from Figure 4.19. The T_1-weighted image with gadolinium (Gd) contrast agent and the tumour (blue) and contralateral ROI (green) are also depicted.

A representative slice of the reconstructed OEF, CBF and CMRO2 for one glioblastoma and astrocytoma patient is shown in Figure 4.19. In addition, it depicts the corresponding T_1-weighted image with gadolinium (Gd) contrast

agent with the tumour outlined in blue as well as the mirrored ROI on the contralateral side outlined in green. The OEF maps in both patients reveal a uniform distribution in the healthy appearing tissue with values between 20 % and 40 %. In contrast, the OEF inside the tumour and also in the surrounding oedema is lower with values around 10 %. The CBF is visibly increased in the periphery of the glioblastoma; no contrast is obvious in the astrocytoma. CMRO2 does also not reveal an obvious contrast neither in the glioblastoma nor in the astrocytoma.

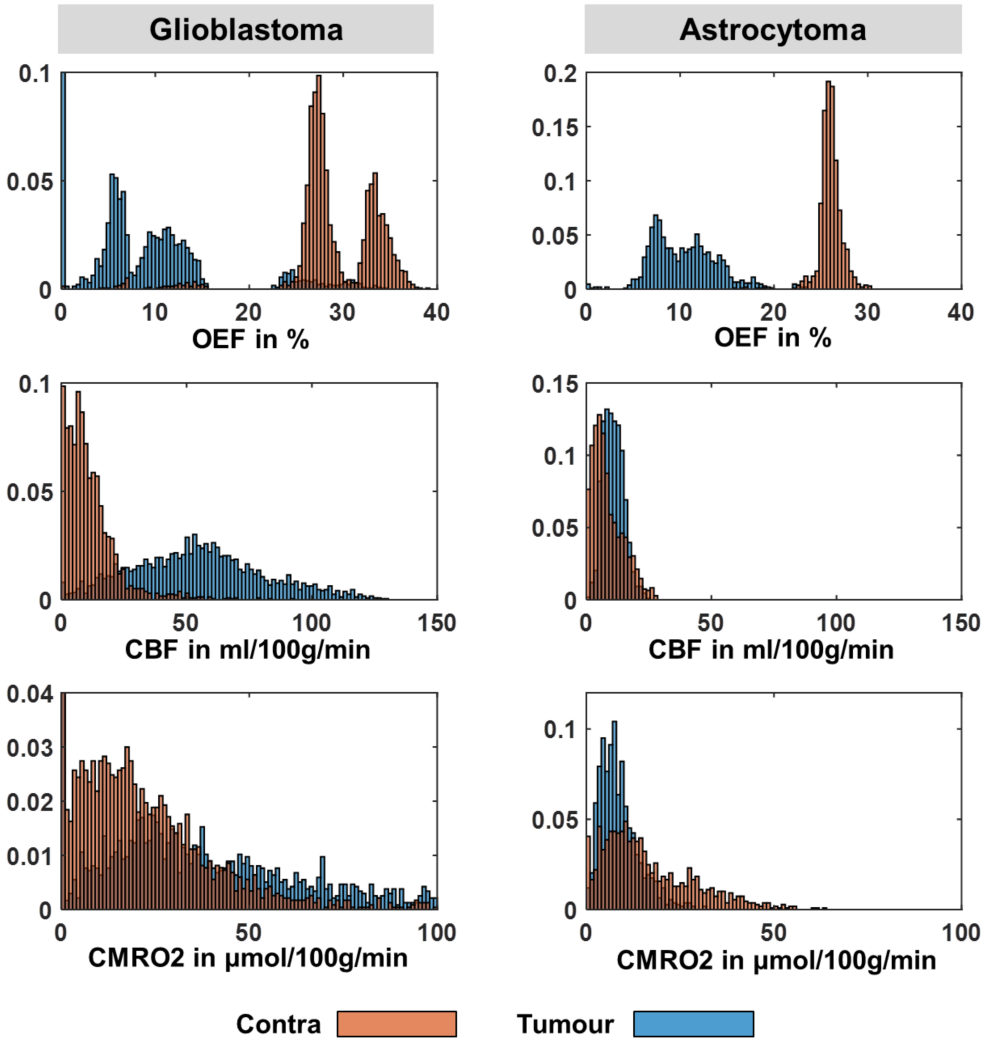

Figure 4.21: Normalised histograms of the oxygen extraction fraction (OEF), cerebral blood flow (CBF) and cerebral metabolic rate of oxygen (CMRO2) within the tumour (blue) and contralateral ROI (orange) of the glioblastoma (left) and astrocytoma patient (right) as depicted in Figure 4.19.

Figure 4.20 illustrates the deoxygenated blood volume ν, transverse relaxation rate R_2 and non-blood magnetic susceptibility χ_{nb} for the same representative slice of the glioblastoma and astrocytoma patient as in Figure 4.19. Con-

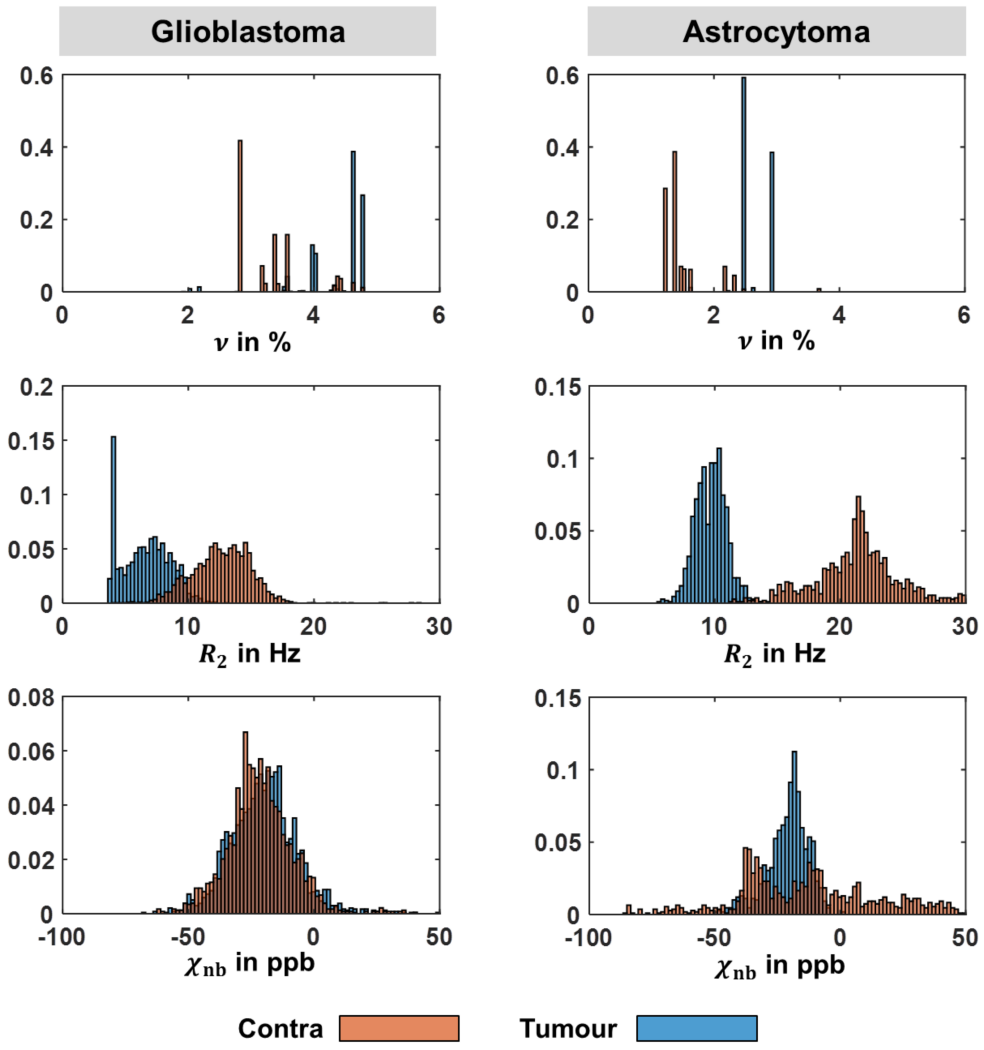

Figure 4.22: Normalised histograms of the deoxygenated blood volume ν, transverse relaxation rate R_2 and non-blood magnetic susceptibility χ_{nb} within the tumour (blue) and contralateral ROI (orange) of the glioblastoma (left) and astrocytoma patient (right) as depicted in Figure 4.20.

trast between the tumour including the surrounding oedema and the healthy appearing tissue is visible for ν and R_2.

The distributions of OEF, CBF and CMRO2 within the tumour and contralateral ROI of the glioblastoma and astrocytoma are shown in Figure 4.21. Similarly, Figure 4.22 depicts the distributions of ν, R_2 and χ_{nb}. Distinct contrast between the two regions is visible for the OEF, ν and R_2 in both tumour types and for the CBF but only in the glioblastoma. Two separate peaks are present in the distribution of the OEF within both tissue ROIs for the glioblastoma but merely within the tumour for the astrocytoma. The distribution of ν consists of only a few almost discrete values in both tissue ROIs and for both glioblastoma and astrocytoma.

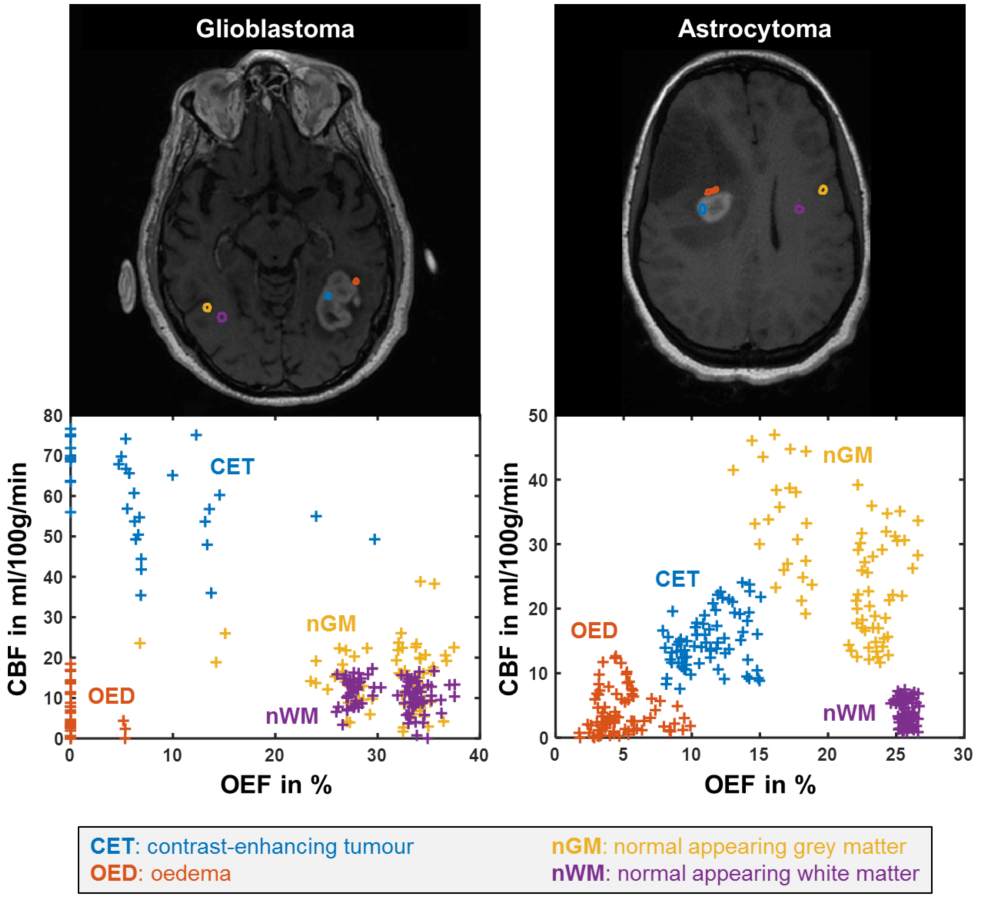

Figure 4.23: Plot of the oxygen extraction fraction (OEF) versus cerebral blood flow (CBF) for ROIs inside the contrast-enhancing tumour (CET), oedema (OED), normal appearing grey matter (nGM) and normal appearing white matter (nWM) for the same representative glioblastoma (left) and astrocytoma patient (right) as in Figure 4.19. The corresponding T_1-weighted image plus gadolinium contrast agent is depicted at the top with the ROIs for CET (blue), OED (orange), nGM (yellow) and nWM (purple) outlined.

Figure 4.23 plots the OEF versus CBF within a ROI in the contrast-enhancing tumour (CET), oedema (OED), normal appearing grey matter (nGM) and normal appearing white matter (nWM) again for the representative glioblastoma and astrocytoma patient. Distinct clustering of the tissue types is visible with low OEF and CBF values especially in the oedema. Yet, two groups of OEF values are also detectable in the CET, nGM and nWM of the glioblastoma and the nGM of the astrocytoma.

The intersubject variation of the OEF, CBF and CMRO2 within the tumour and contralateral ROI of all six glioblastoma and both astrocytoma patients is depicted in the boxplot in Figure 4.24. Mean and standard deviation of the individual means inside the tumour are OEF $= 17.2 \pm 6.1\,\%$, CBF $= 108.1 \pm 83.3\,\mathrm{ml/100\,g/min}$, CMRO2 $= 146 \pm 123\,\mu\mathrm{mol/100\,g/min}$ for the glioblastoma and OEF $= 12.5 \pm 0.5\,\%$, CBF $= 9.2 \pm 3.9\,\mathrm{ml/100\,g/min}$, CMRO2 $= 9 \pm 4\,\mu\mathrm{mol/}$

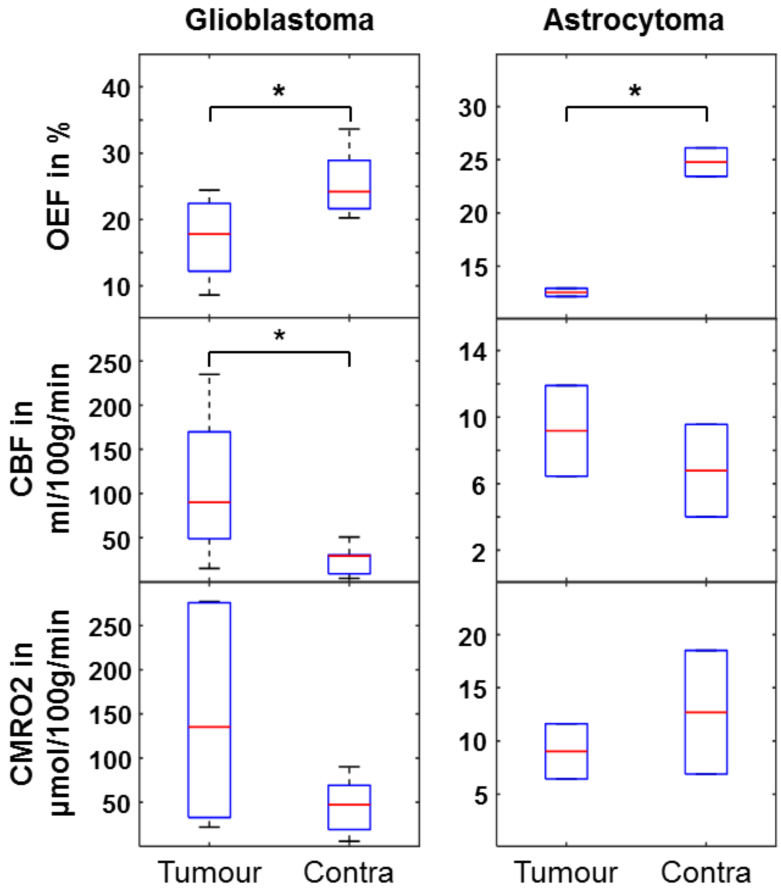

Figure 4.24: Boxplot illustrating intersubject variability for all six glioblastoma (left) and two astrocytoma patients (right) with regard to the oxygen extraction fraction (OEF), cerebral blood flow (CBF) and cerebral metabolic rate of oxygen (CMRO2) inside the tumour and its contralateral ROI. Depicted are median (red), first and third quartile (blue) and whiskers at 1.5 times the interquartile distance (black). Significant differences ($p < 0.05$) between the tumour and its contralateral ROI are marked with an asterisk.

100 g/min for the astrocytoma. Inside the contralateral ROI it is OEF $= 24.8 \pm 4.5\,\%$, CBF $= 29.1 \pm 21.0$ ml/100 g/min, CMRO2 $= 51 \pm 36$ µmol/100 g/min for the glioblastoma and OEF $= 24.5 \pm 2.3\,\%$, CBF $= 6.9 \pm 3.6$ ml/ 100 g/min, CMRO2 $= 13 \pm 8$ µmol/100 g/min for the astrocytoma. The OEF is significantly ($p < 0.05$) lower in the tumour compared to the contralateral side for both tumour types. The CBF on the other hand is significantly ($p < 0.05$) higher inside the tumour but only in the glioblastoma. The CMRO2 does not show a significant difference.

5 DISCUSSION

This chapter discusses the findings of the three main parts of this thesis: The comparison of the GESSE and GRE sequence for QSM+qBOLD analysis, the application of an artificial neural network for QSM+qBOLD analysis of GRE data and finally the mapping of tissue oxygenation in high-grade glioma patients. The first and second part have been published as Hubertus et al. [2019b] and Hubertus et al. [2019c] respectively and the corresponding descriptions are replicated from named publications. The third part has been published as Hubertus et al. [2019a].

5.1 COMPARISON OF GESSE AND GRE FOR QSM+qBOLD ANALYSIS

In this part, a GESSE sequence for OEF reconstruction from combined QSM and qBOLD was implemented and compared to the approach of Cho et al. [2018], which relies on GRE data, using simulations and seven healthy volunteers. The GRE data was still utilised for QSM in this initial comparison as the GESSE sequence employed here does not yet allow sampling of the FID prior to the refocusing pulse.

The relative condition number of F_{qBOLD} with the chosen sequence timings was generally lower for GESSE than GRE for a wide range of OEF and ν. This indicates that the extensive sampling of the short- and long-term regime possible with GESSE allows for a more robust separation of these two parameters in theory.

Moreover, this fact is underlined by the higher accuracy of the reconstructed parameters for GESSE in the single-compartment brain simulation except for white matter ν. However, the relative residuals of OEF and ν from GESSE showed an obvious grey-white matter contrast in the single-compartment simulation, which is due to the different initialisation. The GRE reconstruction is initialised with the correct ν contrast and uses this to fit for the initial R_2. The GESSE fit on the other hand assumes a single value for ν and seems not to reach the optimal solution for the stopping criteria chosen here. Employing the GRE initialisation also for the GESSE reconstruction removes this grey-white matter bias and even further increases the parameter accuracy.

The multi-compartment simulation on the other hand paints a different picture and yields higher accuracy of the GESSE parameters only in grey matter. Although the echo times of GESSE mainly sample the relaxation of the tissue compartment in white matter, the prolonged sampling duration seems to make it more susceptible to the compartmentalisation than the GRE. This leads to an overestimation of R_2 in white matter entailing a strong underestimation of OEF. Yet, one has to keep in mind that the simulated white matter here represents a simplification as it does not include the orientation-dependent

effects of the myelin sheaths [Bouvier et al., 2103] and, thus, the results have to be treated with caution. Surprisingly, the initialisation of the GESSE reconstruction with the ground truth ν distribution does not improve the accuracy of OEF and ν but rather lowers it both in grey and white matter by promoting even stronger grey-white matter contrast in ν. The relative residuals of the GRE simulation show less contrast between grey and white matter especially for the OEF; however, the OEF seems slightly overestimated in grey and white matter as well as ν in grey matter.

The in vivo brain parameter maps and histograms also illustrate a distinct difference between GESSE and GRE. Whereas the OEF has a broad distribution with strong grey and white matter contrast for the former, it has a narrower distribution with little contrast for the latter. Moreover, the mean OEF over grey and white matter is lower for GESSE, being reduced by 4.2 % from its starting value, compared to GRE where it is increased by 15.5 % from its initialisation. The latter is in accordance with the multi-compartment simulation results. ν reveals the opposite behaviour having a narrower distribution for GESSE compared to GRE with GRE showing a stronger grey and white matter contrast. The median value from GESSE deviates by 0.2 % from the mean starting value; yet, the median value and even the distribution of ν remains the same as the initial guess for GRE making it strongly dependent on this first estimate. This feature is most prominent in the histogram of ν, which seems to be cut off at roughly 1.2 %. Quantification of blood flow in white matter from ASL is challenging due to poor SNR resulting in very low estimations that yield an initial guess of approximately 1.2 % for ν according to Equation 3.2. Hence, there might well be biases in the initial guess for ν, also due to the empirical nature of Equation 3.2, that will propagate into the final parameter maps. Using the single value initialisation and prior low resolution fit as implemented for GESSE, might therefore be advantageous. Similar to ν, R_2 displays a broader distribution with more noticeable grey and white matter contrast for GRE. This actually contradicts the findings of the multi-compartment simulation that predicted stronger contrast for GESSE. Yet, again the simplified representation of white matter used for simulation here might cause this inconsistency.

The intersubject mean of OEF across grey and white matter from GESSE in vivo is significantly lower than from GRE, mirroring the trend seen in the multi-compartment simulation. Moreover, it has lower intersubject variability. However, both values are still within the physiological range of $30 - 45$ % reported in literature [Bolar et al., 2011; He and Yablonskiy, 2007; Leenders et al., 1990; Carpenter et al., 1991; Yamauchi et al., 1999; Diringer et al., 2000; An and Lin, 2000; Bulte et al., 2012; Gauthier and Hoge, 2012; Wise et al., 2013; Ito et al., 2004] with the former being at the lower and the latter at the upper end. One possible explanation could be a general overestimation of the OEF by the GRE sequence as seen in the multi-compartment simulation. On the other hand, neglecting diffusion has shown to lead to an underestimation of OEF when applying the qBOLD model to a GESSE sequence [Dickson et al., 2010]. Accordingly, CMRO2 from GESSE is significantly lower

than from GRE for grey and white matter and white matter alone. In contrast to the OEF, however, the mean values are below the physiological range of $120 - 180\,\mu mol/100\,g/min$ found in literature [Bolar et al., 2011; Cho et al., 2018; Leenders et al., 1990; Bulte et al., 2012; Gauthier and Hoge, 2012; Wise et al., 2013; Ito et al., 2004; Zhang et al., 2015, 2017]. This seems mainly owing to a general underestimation of the perfusion from ASL especially in grey matter. Possible reasons could be imperfect labelling [Alsop et al., 2015], varying arrival times of the inflowing blood [Bokkers et al., 2012] and partial volume effects due to low resolution in the ASL sequence. Yet, this issue could be overcome by employing alternative ASL techniques in future studies [Wells et al., 2010; von Samson-Himmelstjerna et al., 2016; Dai et al., 2013], which would also highly benefit the initial guess for ν. Moreover, the intersubject mean of ν is significantly lower for GESSE than for GRE. Since this only holds for grey matter and combined grey and white matter however, this could be due to the lower resolution of the GESSE acquisition. Still, it is also in accordance with the multi-compartment simulation that indicated an overestimation of ν in grey matter for GRE. Nonetheless, the value within combined grey and white matter from both sequences is in good agreement with the literature values from the studies of An and Lin [2002a,b] and Bulte et al. [2007] varying between 2.46 and 3.77 %. Although the mean R_2 in combined grey and white matter demonstrated no significant difference between GESSE and GRE, the value in grey matter alone was significantly higher for GESSE, whereas the value in white matter was significantly lower. This reduced intersubject R_2 contrast for GESSE found in vivo agrees with the visual impression gained from the representative subject mentioned above.

Generally, the GESSE and GRE reconstructions seem to distribute the inherent grey and white matter contrast differently to the underlying parameters in vivo. The intersubject means within grey matter and white matter from GESSE were significantly different for OEF, ν, R_2, χ_{nb} and CMRO2, whereas significant contrast was restricted to ν, R_2 and CMRO2 for GRE. Uniform OEF without grey-white matter contrast, as produced by the GRE reconstruction, is in accordance with earlier findings from PET [Gusnard and Raichle, 2001]. The main source of grey-white matter contrast in the magnetic susceptibility is not the deoxygenated blood volume ν but the abundance of diamagnetic myelin in white matter [Langkammer et al., 2012; Wisnieff et al., 2015]; hence, contrast should also be present in χ_{nb}. Both GESSE and GRE reveal more negative susceptibility in white matter with the contrast being significant only for GESSE however.

There are also general limitations to the approach of combined qBOLD and QSM reconstruction. For example, the large susceptibilities in deep grey matter due to iron accumulation [Zheng et al., 2013] cannot be attributed entirely to χ_{nb} both for the GESSE and GRE reconstruction. Moreover, it relies on the proper removal of macroscopic field inhomogeneities. Using the background field calculated during the QSM process as presented here, seems to be sufficient for the GRE data; the GESSE data, however, still suffers from signal dropout in large areas in inferior slices close to air-tissue interfaces. These

artefacts lead to unreliable estimations, particularly of OEF and ν. Similarly, the GESSE signal underestimation around the spin echo in white matter might hint at a possible remaining background field. This is an inherent disadvantage of the GESSE sequence. Despite the inclusion of the spin echo, the 2D acquisition and longer echo times make it more sensitive to field inhomogeneities facilitating additional signal dropout. The GRE sequence on the other hand allows for shorter echo times and higher resolution in 3D, making it more robust towards field inhomogeneities.

It is difficult to say which sequence is better for combined QSM+qBOLD at this point, especially due to the lack of a comparison to a gold standard in vivo. It is therefore that the appropriate sequence should be chosen depending on the application. On the one hand, the GESSE sequence has proven to be more accurate in simulated grey matter. Despite the grey-white matter contrast of OEF in vivo, it theoretically allows for an extension to the multi-compartment qBOLD model [He and Yablonskiy, 2007] to account for tissue compartmentalisation due to its extensive sampling of the signal decay. Moreover, it revealed lower intersubject variability of OEF. Yet, it requires extensive shimming and background field correction and produces lower resolution images with longer acquisition times. On the other hand, GRE has a more efficient sampling and acquisition, produces fewer artefacts and is easier to implement as it is commonly available on all scanners. All this would greatly facilitate a clinical implementation. Possible remaining biases, such as overestimation of the OEF or inaccurate initialisation of ν, could be overcome by additional postprocessing steps, for example by including regularisation [Zhang et al., 2018] or a reconstruction based on artificial neural networks [Domsch et al., 2018]. Furthermore, whether the precision of both sequences is sufficient to determine subtle changes in oxygenation in diseases, such as stroke and brain tumours, remains to be investigated.

5.2 ARTIFICIAL NEURAL NETWORKS FOR QSM+qBOLD ANALYSIS

In this part, an ANN was successfully implemented to quantify the OEF with QSM+qBOLD.

Training the ANN with normally, in contrast to uniformly, distributed parameters generates more accurate results in simulation. For Y, R_2 and χ_{nb} this is even true when the ground truth Y deviates from the mean training value. In case of the simulated lesion, the ANN actually even introduces a smaller bias than the QN method. Moreover, the ANN generally has a regularising effect on the reconstructed parameters producing a lower standard deviation for the relative reconstructed error compared to QN. This can be interpreted as having higher precision. However, one has to keep in mind that the amount of regularisation is determined by the chosen standard deviation of the training parameters. For example, the ANN will lose its sensitivity to subtle changes of a parameter if the parameter distribution for training is too narrow. The training parameters used here were chosen to have an appropriate tradeoff between sensitivity and increased robustness of the reconstruction.

Moreover, choosing two distinct training parameter distributions for grey and white matter in contrast to an equal consideration of both tissue types, allows the ANN to more easily disentangle the contributions of the parameters of the qBOLD model. Accurate separation of the parameters, especially of OEF and ν, is a general problem of qBOLD [Hubertus et al., 2019b] and is also prominent for the ANN used by Domsch et al. [2018].

In vivo, the representative slice of the OEF reconstructed with the ANN reveals stronger contrast between grey and white matter, which contradicts earlier findings of uniform OEF in the resting brain using PET [Gusnard and Raichle, 2001]. Moreover, the mean OEF value from ANN is higher than from QN. The R_2 map from the ANN seems to have a similar, albeit less strong, grey-white matter contrast compared to the QN reconstruction whereas the ν maps are distinctively different. No obvious differences in contrast are visible in the representative slice of χ_{nb} and S_0 between the ANN and QN reconstruction. In general however, the maps from the ANN seem noisier, which is most probably due to the voxelwise reconstruction compared to the full brain minimisation used in the QN approach.

The differences present in the OEF distribution of the representative subject are also reflected in the intersubject mean in white matter, which is significantly higher for the ANN than for the QN reconstruction. The mean OEF in grey and white matter in both cases is at the higher end of the range of 30 % to 45 % found in literature [Bolar et al., 2011; He and Yablonskiy, 2007; Leenders et al., 1990; An and Lin, 2003; Bulte et al., 2012; Gauthier and Hoge, 2012]. However, the ANN produces a lower intersubject variability compared to least-squares approaches [Christen et al., 2012; Cho et al., 2018; He and Yablonskiy, 2007; Leenders et al., 1990; An and Lin, 2003; Zhang et al., 2018]. Taking into account the negative linear trend displayed in the Bland-Altman plot and the mean difference that is compatible with 0, the ANN implemented here seems to have a regularising effect also on the intersubject mean OEF. A similar trend is present in the Bland-Altman plot for R_2 and ν. Two distinct clusters for grey and white matter are visible in all three plots indicating contrast between the two tissue types. The ANN method reconstructs generally higher mean χ_{nb} and S_0 values; yet, only the former shows a significant difference for the intersubject mean within grey matter, probably due to the large intersubject variation of the latter.

In order to determine how the ANN compares to QN approaches in dealing with possible biases and artefacts in the underlying χ maps and GRE magnitude images in vivo, a full sensitivity analysis is required. In addition, the training parameters of the ANN presented here mainly represent healthy tissue. Further studies, for instance examining a cohort of stroke patients where the OEF can be assumed to deviate from 40 % in large brain areas, are necessary to decide whether the chosen training parameters are also appropriate for these cases.

One general disadvantage of neural networks for curve-fitting is the lower flexibility of the approach. If the SNR of the data significantly changes due to alterations of acquisition parameters for example, the network will have to

be retrained in order to correctly account for the noise. Nonetheless, several networks could be trained with varying SNR so that networks for a wide range of possible noise levels are available. This makes the ANN approach even more efficient than the least-squares QN fitting as the weighting factor actually also needs to be adapted if the SNR changes. Similarly, if the number or spacing of the acquired echoes is modified, the ANN also has to be retrained. However, minimum spacing and maximum number of echoes profits both QSM and qBOLD analysis so that alterations of these two parameters are seldom needed after they have been optimised.

One major benefit of the ANN compared to the QN method is that it removes the necessity of an additional ASL acquisition for initialisation of ν. The QN reconstruction strongly depends on this first estimate as the final ν does not deviate much from the starting value maps. Thus, any bias in ν_{start} due to improper labelling, partial volume effects or a different relation between CBF and ν [Ciris et al., 2014] for instance, would directly propagate into the final ν and all other parameter maps. This is most prominent in the lower cutoff of the ν distribution for the representative subject. The measured CBF values in many white matter voxels are close to 0 due to the actually low white matter perfusion combined with the low SNR of the pCASL sequence. According to the empirical relationship in Equation 3.2 [Leenders et al., 1990], this results in $\nu_{\text{start}} \approx 1.2\,\%$ for all these voxels introducing a bias that remains in the final ν maps. The ANN on the other hand does not require initialisation and still generates contrast between grey and white matter and a rather Gaussian distribution for ν. Another advantage of the ANN method is its speed. The reconstruction time of approximately one second would allow for an online reconstruction; thus, favouring a possible implementation in the clinical routine.

Which method is more accurate in vivo can only be determined by a comparison to a ground truth, possibly from ^{15}O-PET, in the end. Nonetheless, the ANN approach presented here is a faster and, with regard to initialisation, more robust alternative for OEF mapping from QSM+qBOLD than the traditional QN approach. Whether this increased speed and robustness comes at the cost of lower sensitivity to subtle OEF changes in diseases, such as stroke and brain tumours, still remains to be investigated in future clinical studies.

5.3 TISSUE OXYGENATION IN HIGH-GRADE GLIOMAS

In this part, machine learning-based clustering was successfully incorporated into the least-squares fitting procedure for QSM+qBOLD and applied to six glioblastoma and two astrocytoma patients.

The clustering as an intermediate processing step allowed for the reconstruction of a uniform OEF in the healthy appearing tissue with values between 20 % and 40 % as predicted for the healthy, resting brain by PET [Gusnard and Raichle, 2001]. On the other hand, the tumour and the surrounding area of apparent oedema also revealed rather uniform OEF, however, with lower values between 10 % and 25 %. Similarly, contrast between the tumour plus surround-

ing apparent oedema and the healthy appearing tissue is visible for ν and R_2 especially for the astrocytoma. ν is higher and R_2 is lower inside the tumour plus surrounding apparent oedema compared to the healthy appearing tissue. The increased water content in the oedema would lead to a decrease in R_2; yet, there is no physiological explanation for the homogeneously increased ν. This is most likely caused by a combination of the clustering and the fact that it is difficult to properly disentangle the microscopic and mesoscopic effects in the qBOLD model when the signal is slowly decaying, i. e. when R_2 is low. Generally, the higher the water content inside the tissue, the less accurate the qBOLD model becomes.

Remnants of the intermediate clustering are also visible in the histograms of the OEF and ν. The OEF reveals two separate distributions both within the tumour ROI and the contralateral side. Even more prominently, ν shows rather discrete values in both cases. This is in accordance with earlier findings [Hubertus et al., 2019b,c] that the final ν maps from QSM+qBOLD do not deviate much from their starting values. Hence, the introduction of clustering into the QSM+qBOLD reconstruction seems to increase the robustness of the method; yet, it might also introduce biases especially for ν. It is therefore that a comparison to a ground truth, for example from ^{15}O-PET is crucial in order to determine whether the contrast seen in the tumour is actually owing to physiology and not to a failure of the model for instance.

Distinct groups for the separate tissue ROIs can be detected in the OEF versus CBF plot. The plot indicates a negative correlation among contrast-enhancing tumour, normal appearing grey matter and normal appearing white matter, especially for the glioblastoma, which is in accordance with the study by Preibisch et al. [2017] that used a multi-parametric qBOLD approach [Christen et al., 2011]. In contrast to Preibisch et al. [2017] however, the method implemented here is able to reconstruct the actual OEF in % rather than a 'relative' OEF. Moreover, some voxels in the contrast-enhancing tumour and especially oedema revealed both low OEF and CBF, which might allow for a possible distinction between still viable and non-viable tissue.

The intersubject comparison of the oxygenation parameters found a significantly reduced OEF inside the tumour compared to the contralateral ROI both for the glioblastoma and astrocytoma. This is in accordance with the study of Stadlbauer et al. [2017] that also used a multi-parametric qBOLD approach. However, the technique presented here, enables the reconstruction of a more uniform OEF in the healthy appearing tissue as predicted by physiology [Gusnard and Raichle, 2001]. In addition, a significantly increased CBF inside the tumour was found but only for the glioblastoma. This also agrees with physiology as glioblastomas are known to promote extensive angiogenesis and are considered to be among the most vascularised solid tumour types [Hardee and Zagzag, 2012; Wen and Kesari, 2008]. The product of OEF and CBF, the CMRO2 revealed no significant contrast. This contradicts the findings from Stadlbauer et al. [2017] who measured a significantly increased CMRO2 inside the tumour for high-grade glioma. One possible explanation

could be the much smaller patient cohort (8 versus 62) employed in the study presented here.

Using machine learning in cooperation with QSM+qBOLD to map the tissue oxygenation in high-grade glioma as implemented here is a promising approach. It not only reproduces the findings of earlier multi-parametric qBOLD studies [Preibisch et al., 2017; Stadlbauer et al., 2017] but also enables the reconstruction of an absolute OEF that is uniform and in a physiologically meaningful range in healthy appearing tissue. Moreover, as the underlying GRE sequence is a highly efficient standard MRI sequence, the approach might facilitate a wider clinical implementation. This is critical since further clinical studies with larger patient cohorts of varying tumour grades and especially a comparison to a ground truth from ^{15}O-PET for instance is mandatory to establish the approach presented here as valuable addition to the diagnosis, treatment planning and response assessment of glioma patients.

6 CONCLUSION AND OUTLOOK

The objective of this thesis was to include QSM into an optimised MRI-based reconstruction of the brain tissue oxygenation and to evaluate its application especially to patients suffering from high-grade glioma.

In the first part of this work, a comparison between the GESSE and GRE sequence for quantification of the OEF with a QSM+qBOLD analysis was carried out. GESSE outperformed GRE at accurate parameter estimation in grey matter simulations. Yet, it produced unphysiological grey-white matter contrast in the OEF in vivo. GRE revealed slight biases in the reconstructed parameters in simulation; however, it provided uniform OEF maps in vivo with higher spatial and temporal resolution. Hence, which sequence is better for QSM+qBOLD reconstruction, should be decided based on the desired application. Nonetheless, the GRE sequence is favourable with regard to a clinical implementation. As a standard MRI sequence it is readily available on every scanner and furthermore allows for higher resolution images in a shorter scan time. Utmost effort should be put into removing background inhomogeneities when using GESSE and obtaining accurate parameter initialisation maps when using GRE.

The second part focused on implementing an artificial neural network to map the OEF from a QSM+qBOLD approach. Compared to the least-squares fitting using quasi-Newton optimisation from the first part, the ANN was much faster, did not require parameter initialisation from additional acquisitions and generated OEF maps with lower intersubject variability. Hence, the inclusion of machine learning is a further promising step towards a clinical implementation of QSM+qBOLD.

Lastly, machine learning-based clustering was incorporated into the least-squares fitting QSM+qBOLD approach in order to further increase its robustness. This technique was then applied to six glioblastoma and two astrocytoma patients. A significantly reduced OEF was found in the tumours compared to the contralateral side for both tumour types as well as a significantly increased CBF, however only for the glioblastoma. The CMRO2 revealed no significant differences. The QSM+qBOLD method proposed here was able to reproduce some findings of previous multi-parametric qBOLD studies; yet, in addition, it generated uniform OEF maps in the healthy appearing tissue with physiologically sound values.

Exploiting the full information, i. e. the phase and magnitude, of a GESSE or GRE sequence for reconstruction of the OEF inside the brain with a QSM+qBOLD approach is remarkably promising. The incorporation of machine learning techniques further increases the robustness and speed of the highly sensitive qBOLD reconstruction, which could particularly facilitate a clinical implementation. Nevertheless, additional studies with a larger cohort of glioma patients are necessary to determine the optimal tradeoff between robustness

and sensitivity to subtle changes of the underlying oxygenation parameters for the QSM+qBOLD approaches presented here. Similarly, a comparison to a gold standard, for example ^{15}O-PET is vital to determine the accuracy and sensitivity of the method. After such a validation, the technique could be included into radio- and chemotherapy treatment planning and also utilised for assessment of treatment response. Moreover, the general method might also be applicable to any pathology affecting the brain metabolism including stroke or addiction for instance.

A

APPENDIX

A.1 PUBLICATIONS

The studies in the first, second and third part of this thesis have been published separately and are referred to as Hubertus et al. [2019b], Hubertus et al. [2019c] and Hubertus et al. [2019a] respectively throughout.

Peer-Reviewed Journal Articles

Hubertus, S., Thomas, S., Cho, J., Zhang, S., Wang, Y., and Schad, L. R. (2019b). Comparison of gradient echo and gradient echo sampling of spin echo sequence for the quantification of the oxygen extraction fraction from a combined quantitative susceptibility mapping and quantitative BOLD (QSM+ qBOLD) approach. *Magnetic Resonance in Medicine*, `https://doi.org/10.1002/mrm.27804`.

Hubertus, S., Thomas, S., Cho, J., Zhang, S., Wang, Y., and Schad, L. R. (2019c). Using an artificial neural network for fast mapping of the oxygen extraction fraction with combined QSM and quantitative BOLD. *Magnetic Resonance in Medicine*, `https://doi.org/10.1002/mrm.27882`.

Schulz, V., Straub, M., Mahlke, M., Hubertus, S., Lammers, T., and Kiessling, F. (2015). A Field Cancellation Signal Extraction Method for Magnetic Particle Imaging. *IEEE Transactions on Magnetics*, 51(2):1–4.

Conference Contributions

Hubertus, S., Thomas, S., Cho, J., Zhang, S., Kovanlikaya, I., Wang, Y., and Schad, L. R. (2019a). MRI-based oxygen extraction fraction and cerebral metabolic rate of oxygen mapping in high-grade glioma using a combined quantitative susceptibility mapping and quantitative blood oxygenation level-dependent approach. In *Proceedings of International Society for Magnetic Resonance in Medicine*, volume 27, page 0391. Montréal, Canada.

Hubertus, S., Thomas, S., Cho, J., Zhang, S., Wang, Y., and Schad, L. R. (2019d). Comparison of Gradient Echo and Gradient Echo Sampling of Spin Echo Sequence for the Quantification of the Oxygen Extraction Fraction by Combining Quantitative Susceptibility Mapping and Blood Oxygenation Level Dependency. In *Proceedings of International Society for Magnetic Resonance in Medicine*, volume 27, page 2721. Montréal, Canada.

Hubertus, S., Thomas, S., Domsch, S. and Schad, L. R. (2017). How do the number of echoes and the echo spacing affect the quality of non-linear field

estimates in QSM? In *Proceedings of European Society for Magnetic Resonance in Medicine and Biology*, volume 34, page 105. Barcelona, Spain.

Thomas, S., Hubertus, S., Skampardoni, I., Hartig, N., Vollstaedt-Klein, S., and Schad, L. R. (2019). The Acute Effects of Cigarette Smoking on Brain Oxygenation and Perfusion Measured by Multi-Parametric Quantitative BOLD and Arterial Spin Labeling MRI: Preliminary Results. In *Proceedings of International Society for Magnetic Resonance in Medicine*, volume 27, page 2925. Montréal, Canada.

Chacon-Caldera, J., Hatz, L., Kruse, A., Uhrig, T., Zimmer, F., Hubertus, S., Hermann, I., Schad, L. R., and Zöllner, F. (2019). Investigating Variability Sources in Kidney Perfusion Measurements with Pulsed ASL: A Phantom and In Vivo Pilot Study. In *Proceedings of International Society for Magnetic Resonance in Medicine*, volume 27, page 5020. Montréal, Canada.

Thomas, S., Hubertus, S., Domsch, S., and Schad, L. R. (2018a). How does the weighting factor in a regularized quantitative BOLD approach affect the estimated oxygen extraction fraction? In *Proceedings of International Society for Magnetic Resonance in Medicine*, volume 26, page 2093. Paris, France.

Thomas, S., Hubertus, S., Förster, A., and Schad, L. R. (2018b). Messung des Sauerstoffverbrauchs im Gehirn einer Glioblastom-Patientin mittels regularisierter qBOLD-Auswertung. In *Proceedings of Jahrestagung der Deutschen Gesellschaft für Medizinische Physik*, volume 21, page 102. Nürnberg, Germany.

Uhrig, T., Hubertus, S., Chacon-Caldera, J., Schad, L. R., and Zöllner, F. (2018). Entwicklung eines Phantoms für DCE und ASL Messungen zur Quantifizierung von Perfusionsparametern. In *Proceedings of Jahrestagung der Deutschen Gesellschaft für Medizinische Physik*, volume 21, page 19. Nürnberg, Germany.

Rea, M., Hubertus, S., Mcrobbie, D., and Young, I. (2015). Phase Encoded Artefact Suppression for imaging near metal implants. In *Proceedings of European Society for Magnetic Resonance in Medicine and Biology*, volume 32, page 122. Edinburgh, UK.

Straub, M., Hubertus, S., Kiessling, F., and Schulz, V. (2015). MPI Field Generator Design for an FFL Based Image Acquisition. In *Proceedings of International Workshop on Magnetic Particle Imaging*, volume 5, page 29. Istanbul, Turkey.

A.2 TABLES

The following two tables summarise the mean values and standard deviations of OEF, CMRO2, CBF, ν, R_2 and χ_{nb} for all seven subjects reconstructed from the GESSE and GRE sequence respectively as mentioned in Section 4.2.

Table A.1: Mean ± standard deviation of the oxygen extraction fraction (OEF), cerebral metabolic rate of oxygen (CMRO2), cerebral blood flow (CBF), deoxygenated blood volume ν, transverse relaxation rate R_2 and non-blood magnetic susceptibility χ_{nb} in combined grey and white matter (GM+WM) and in grey matter (GM) and white matter (WM) separately for all seven subjects examined with the GESSE sequence. Intersubject variability is given by the mean ± standard deviation of the individual means.

#	GM+WM	GM	WM	GM+WM	GM	WM	GM+WM	GM	WM
	OEF in %			CMRO2 in µmol/100 g/min			CBF in ml/100 g/min		
1	30.6 ± 17.4	34.1 ± 18.4	27.8 ± 16.0	57 ± 67	92 ± 78	30 ± 38	23.5 ± 18.9	35.6 ± 18.3	14.0 ± 13.1
2	30.5 ± 16.7	33.9 ± 19.1	28.2 ± 14.4	49 ± 62	79 ± 79	29 ± 36	20.1 ± 17.3	29.6 ± 18.1	13.6 ± 13.2
3	32.6 ± 19.2	35.7 ± 22.0	30.0 ± 16.2	69 ± 78	105 ± 92	40 ± 46	27.1 ± 20.3	39.0 ± 19.5	17.5 ± 15.0
4	32.3 ± 14.1	35.1 ± 16.3	30.2 ± 11.7	88 ± 88	133 ± 102	54 ± 56	34.7 ± 25.4	50.0 ± 24.6	23.2 ± 19.2
5	32.1 ± 16.2	34.5 ± 18.3	30.2 ± 14.2	46 ± 56	61 ± 66	34 ± 42	18.4 ± 16.2	22.6 ± 17.2	15.1 ± 14.5
6	35.0 ± 15.4	36.5 ± 17.4	33.7 ± 13.3	66 ± 73	96 ± 86	38 ± 43	24.3 ± 20.5	34.5 ± 21.3	15.2 ± 14.6
7	33.5 ± 14.0	35.0 ± 15.2	32.3 ± 12.8	48 ± 67	73 ± 81	28 ± 42	18.3 ± 20.0	26.8 ± 22.6	11.2 ± 14.1
mean	32.4 ± 1.6	35.0 ± 0.9	30.3 ± 2.1	60 ± 15	91 ± 24	36 ± 9	23.8 ± 5.8	34.0 ± 9.0	15.7 ± 3.8
#	ν in %			R_2 in Hz			χ_{nb} in ppb		
1	2.8 ± 1.3	3.0 ± 1.6	2.7 ± 0.8	14.7 ± 2.4	13.9 ± 2.7	15.3 ± 1.8	−44 ± 32	−32 ± 32	−54 ± 27
2	2.8 ± 1.2	3.0 ± 1.7	2.6 ± 0.6	14.3 ± 2.0	13.7 ± 2.5	14.8 ± 1.5	−40 ± 31	−31 ± 35	−46 ± 25
3	2.8 ± 2.2	2.9 ± 3.0	2.7 ± 1.2	15.0 ± 2.4	14.0 ± 2.7	15.8 ± 1.8	−40 ± 27	−35 ± 30	−45 ± 24
4	2.9 ± 0.8	3.0 ± 1.0	2.8 ± 0.4	13.7 ± 1.9	13.3 ± 2.1	14.0 ± 1.7	−39 ± 26	−31 ± 28	−45 ± 22
5	3.0 ± 1.5	3.1 ± 2.1	2.8 ± 0.7	14.3 ± 2.2	13.6 ± 2.5	14.8 ± 1.8	−43 ± 32	−35 ± 33	−49 ± 29
6	3.0 ± 1.4	3.1 ± 1.8	2.9 ± 0.9	13.8 ± 2.5	12.6 ± 2.6	14.9 ± 1.8	−43 ± 27	−40 ± 30	−45 ± 24
7	3.0 ± 1.0	3.1 ± 1.3	2.9 ± 0.5	13.7 ± 2.2	12.8 ± 2.3	14.4 ± 1.8	−54 ± 29	−45 ± 30	−62 ± 25
mean	2.9 ± 0.1	3.0 ± 0.1	2.8 ± 0.1	14.2 ± 0.5	13.4 ± 0.5	14.8 ± 0.6	−43 ± 5	−36 ± 5	−49 ± 7

Table A.2: Mean ± standard deviation of the oxygen extraction fraction (OEF), cerebral metabolic rate of oxygen (CMRO2), cerebral blood flow (CBF), deoxygenated blood volume ν, transverse relaxation rate R_2 and non-blood magnetic susceptibility χ_{nb} in combined grey and white matter (GM+WM) and in grey matter (GM) and white matter (WM) separately for all seven subjects examined with the GRE sequence. Intersubject variability is given by the mean ± standard deviation of the individual means.

#	GM+WM	GM	WM	GM+WM	GM	WM	GM+WM	GM	WM
	OEF in %			CMRO2 in µmol/100 g/min			CBF in ml/100 g/min		
1	46.5 ± 5.1	47.8 ± 5.4	45.0 ± 4.1	96 ± 76	132 ± 73	57 ± 57	27.4 ± 21.5	37.4 ± 21.3	16.4 ± 15.7
2	50.0 ± 5.9	50.5 ± 7.0	49.3 ± 4.5	94 ± 80	129 ± 82	62 ± 62	25.1 ± 20.0	34.3 ± 20.8	16.6 ± 15.8
3	38.1 ± 7.0	39.1 ± 7.6	37.0 ± 6.2	87 ± 71	118 ± 72	55 ± 53	29.9 ± 22.5	40.6 ± 22.2	18.9 ± 16.7
4	34.9 ± 6.9	36.5 ± 7.4	33.5 ± 6.1	101 ± 82	142 ± 83	66 ± 63	38.1 ± 27.9	52.5 ± 27.4	25.5 ± 21.4
5	39.9 ± 4.9	40.3 ± 5.4	39.5 ± 4.2	62 ± 63	75 ± 71	48 ± 49	20.8 ± 20.3	25.1 ± 22.7	16.0 ± 15.8
6	44.9 ± 5.0	45.1 ± 5.9	44.8 ± 3.7	89 ± 82	120 ± 88	54 ± 57	26.3 ± 23.2	35.8 ± 24.5	15.8 ± 16.1
7	46.6 ± 6.6	47.0 ± 8.1	46.1 ± 4.6	83 ± 94	113 ± 107	51 ± 64	23.4 ± 24.3	31.9 ± 26.9	14.4 ± 17.1
mean	43.0 ± 5.4	43.8 ± 5.2	42.3 ± 5.6	87 ± 13	118 ± 21	56 ± 6	27.3 ± 5.6	36.8 ± 8.5	17.7 ± 3.7
#	ν in %			R_2 in Hz			χ_{nb} in ppb		
1	3.7 ± 1.8	4.5 ± 1.9	2.8 ± 1.3	13.6 ± 4.9	11.3 ± 5.1	16.0 ± 3.2	−49 ± 38	−43 ± 41	−55 ± 34
2	3.4 ± 1.7	4.1 ± 1.9	2.7 ± 1.2	14.0 ± 5.7	11.5 ± 6.1	16.3 ± 4.2	−36 ± 42	−30 ± 45	−41 ± 39
3	3.7 ± 1.8	4.5 ± 1.8	2.9 ± 1.3	15.3 ± 5.3	12.7 ± 5.4	18.0 ± 3.7	−36 ± 33	−35 ± 35	−37 ± 31
4	4.3 ± 2.1	5.3 ± 2.1	3.3 ± 1.6	14.5 ± 4.6	12.0 ± 4.8	16.7 ± 3.0	−39 ± 30	−34 ± 33	−42 ± 28
5	3.1 ± 1.5	3.4 ± 1.7	2.7 ± 1.2	15.4 ± 5.4	13.6 ± 5.9	17.5 ± 3.8	−41 ± 38	−38 ± 41	−45 ± 35
6	3.5 ± 1.8	4.2 ± 1.9	2.7 ± 1.2	14.1 ± 6.2	11.6 ± 6.5	16.9 ± 4.4	−42 ± 36	−43 ± 40	−40 ± 32
7	3.1 ± 2.1	3.8 ± 2.5	2.5 ± 1.3	14.0 ± 5.7	11.6 ± 6.1	16.6 ± 3.8	−57 ± 33	−53 ± 36	−61 ± 28
mean	3.5 ± 0.4	4.3 ± 0.6	2.8 ± 0.3	14.4 ± 0.7	12.0 ± 0.8	16.9 ± 0.7	−43 ± 8	−40 ± 8	−46 ± 9

BIBLIOGRAPHY

Alsop, D. C., Detre, J. A., Golay, X., Günther, M., Hendrikse, J., Hernandez-Garcia, L., Lu, H., Macintosh, B. J., Parkes, L. M., Smits, M., Van Osch, M. J. P., Wang, D. J. J., Wong, E. C., and Zaharchuk, G. (2015). Recommended implementation of arterial spin-labeled perfusion MRI for clinical applications: A consensus of the ISMRM perfusion study group and the European consortium for ASL in dementia. *Magnetic Resonance in Medicine*, 73(1):102–116.

American Association of Neurological Surgeons (2019a). Brain tumors. `https://www.aans.org/en/Patients/Neurosurgical-Conditions-and-Treatments/Brain-Tumors`. Accessed: June 24, 2019.

American Association of Neurological Surgeons (2019b). Classification of brain tumors. `https://www.aans.org/en/Media/Classifications-of-Brain-Tumors`. Accessed: June 24, 2019.

An, H., Ford, A. L., Vo, K. D., Liu, Q., Chen, Y., Lee, J.-M., and Lin, W. (2014). Imaging oxygen metabolism in acute stroke using MRI. *Current Radiology Reports*, 2(3):39.

An, H. and Lin, W. (2000). Quantitative measurements of cerebral blood oxygen saturation using magnetic resonance imaging. *Journal of Cerebral Blood Flow & Metabolism*, 20(8):1225–1236.

An, H. and Lin, W. (2002a). Cerebral oxygen extraction fraction and cerebral venous blood volume measurements using MRI: Effects of magnetic field variation. *Magnetic Resonance in Medicine*, 47(5):958–966.

An, H. and Lin, W. (2002b). Cerebral venous and arterial blood volumes can be estimated separately in humans using magnetic resonance imaging. *Magnetic Resonance in Medicine*, 48(4):583–588.

An, H. and Lin, W. (2003). Impact of intravascular signal on quantitative measures of cerebral oxygen extraction and blood volume under normo- and hypercapnic conditions using an asymmetric spin echo approach. *Magnetic Resonance in Medicine*, 50(4):708–716.

Aslan, S., Xu, F., Wang, P. L., Uh, J., Yezhuvath, U. S., van Osch, M., and Lu, H. (2011). Estimation of labeling efficiency in pseudo-continuous arterial spin labeling. *Magnetic Resonance in Medicine*, 63(3):765–771.

Barnes, S. R., Ng, T. S., Santa-Maria, N., Montagne, A., Zlokovic, B. V., and Jacobs, R. E. (2015). ROCKETSHIP: a flexible and modular software tool for the planning, processing and analysis of dynamic MRI studies. *BMC Medical Imaging*, 15(1):19.

Bertleff, M., Domsch, S., Weingärtner, S., Zapp, J., O'Brien, K., Barth, M., and Schad, L. R. (2017). Diffusion parameter mapping with the combined intravoxel incoherent motion and kurtosis model using artificial neural networks at 3T. *NMR in Biomedicine*, 30(12):e3833.

Bishop, C. M. (1995). *Neural Networks for Pattern Recognition*. Oxford University Press, Inc., New York, NY, USA.

Bishop, C. M. and Roach, C. M. (1992). Fast curve fitting using neural networks. *Review of Scientific Instruments*, 63(10):4450–4456.

Bloch, F. (1946). Nuclear induction. *Physical Review*, 70(7-8):460–474.

Bloembergen, N., Purcell, E. M., and Pound, R. V. (1948). Relaxation effects in nuclear magnetic resonance absorption. *Physical Review*, 73(7):679–712.

Bokkers, R. P. H., Hernandez, D. A., Merino, J. G., Mirasol, R. V., van Osch, M. J., Hendrikse, J., Warach, S., Latour, L. L., and On behalf of the, N. (2012). Whole-brain arterial spin labeling perfusion MR imaging in patients with acute stroke. *Stroke*, 43(5):1290–1294.

Bolar, D. S., Rosen, B. R., Sorensen, A. G., and Adalsteinsson, E. (2011). Quantitative imaging of extraction of oxygen and tissue consumption (QUIXOTIC) using venular-targeted velocity-selective spin labeling. *Magnetic Resonance in Medicine*, 66:1550–1562.

Bollmann, S., Rasmussen, K. G. B., Kristensen, M., Blendal, R. G., Østergaard, L. R., Plocharski, M., O'Brien, K., Langkammer, C., Janke, A., and Barth, M. (2019). DeepQSM - using deep learning to solve the dipole inversion for quantitative susceptibility mapping. *NeuroImage*, 195:373–383.

Bouvier, J., Castellani, S., Debacker, C. S., Pannetier, N., Troprès, I., Krainik, A., and Barbier, E. L. (2103). Evaluation of multiparametric qBOLD in white matter: A simulation study. In *Proceedings of International Society for Magnetic Resonance in Medicine*, volume 21, page 2492, Salt Lake City, UT, USA.

Buatti, J., Ryken, T. C., Smith, M. C., Sneed, P., Suh, J. H., Mehta, M., and Olson, J. J. (2008). Radiation therapy of pathologically confirmed newly diagnosed glioblastoma in adults. *Journal of Neuro-Oncology*, 89(3):313–337.

Bulte, D., Chiarelli, P., Wise, R., and Jezzard, P. (2007). Measurement of cerebral blood volume in humans using hyperoxic MRI contrast. *Journal of Magnetic Resonance Imaging*, 26(4):894–899.

Bulte, D. P., Kelly, M., Germuska, M., Xie, J., Chappell, M. A., Okell, T. W., Bright, M. G., and Jezzard, P. (2012). Quantitative measurement of cerebral physiology using respiratory-calibrated MRI. *NeuroImage*, 60(1):582–591.

Carpenter, D. A., Grubb, R. L., Tempel, L. W., and Powers, W. J. (1991). Cerebral oxygen metabolism after aneurysmal subarachnoid hemorrhage. *Journal of Cerebral Blood Flow & Metabolism*, 11(5):837–844.

Cho, J., Kee, Y., Spincemaille, P., Nguyen, T. D., Zhang, J., Gupta, A., Zhang, S., and Wang, Y. (2018). Cerebral metabolic rate of oxygen (CMRO2) mapping by combining quantitative susceptibility mapping (QSM) and quantitative blood oxygenation level-dependent imaging (qBOLD). *Magnetic Resonance in Medicine*, 80(4):1595–1604.

Cho, J., Zhang, S., Kee, Y., Spincemaille, P., Nguyen, T., Hubertus, S., Gupta, A., and Wang, Y. (2019). Data-driven regularized inversion (DRI) for improved QSM+qBOLD based CMRO2 mapping: A feasibility study in healthy subjects and ischemic stroke patients. In *Proceedings of International Society for Magnetic Resonance in Medicine*, volume 27, page 2724, Montréal, Canada.

Christen, T., Lemasson, B., Pannetier, N., Farion, R., Segebarth, C., Rémy, C., and Barbier, E. L. (2011). Evaluation of a quantitative blood oxygenation level-dependent (qBOLD) approach to map local blood oxygen saturation. *NMR in Biomedicine*, 24(4):393–403.

Christen, T., Schmiedeskamp, H., Straka, M., Bammer, R., and Zaharchuk, G. (2012). Measuring brain oxygenation in humans using a multiparametric quantitative blood oxygenation level dependent MRI approach. *Magnetic Resonance in Medicine*, 68(3):905–911.

Ciris, P. A., Qiu, M., and Constable, R. T. (2014). Noninvasive MRI measurement of the absolute cerebral blood volume–cerebral blood flow relationship during visual stimulation in healthy humans. *Magnetic Resonance in Medicine*, 72(3):864–875.

Cusack, R. and Papadakis, N. (2002). New robust 3-D phase unwrapping algorithms: Application to magnetic field mapping and undistorting echoplanar images. *NeuroImage*, 16(3):754–764.

Dai, W., Garcia, D., de Bazelaire, C., and Alsop, D. C. (2008). Continuous flow-driven inversion for arterial spin labeling using pulsed radio frequency and gradient fields. *Magnetic Resonance in Medicine*, 60(6):1488–1497.

Dai, W., Shankaranarayanan, A., and Alsop, D. C. (2013). Volumetric measurement of perfusion and arterial transit delay using hadamard encoded continuous arterial spin labeling. *Magnetic Resonance in Medicine*, 69(4):1014–1022.

De Rochefort, L., Brown, R., Prince, M. R., and Wang, Y. (2008). Quantitative MR susceptibility mapping using piece-wise constant regularized inversion of the magnetic field. *Magnetic Resonance in Medicine*, 60(4):1003–1009.

De Rochefort, L., Liu, T., Kressler, B., Liu, J., Spincemaille, P., Lebon, V., Wu, J., and Wang, Y. (2010). Quantitative susceptibility map reconstruction from MR phase data using bayesian regularization: Validation and application to brain imaging. *Magnetic Resonance in Medicine*, 63(1):194–206.

Detre, J. A., Leigh, J. S., Williams, D. S., and Koretsky, A. P. (1992). Perfusion imaging. *Magnetic Resonance in Medicine*, 23(1):37–45.

Dickson, J. D., Ash, T. W. J., Williams, G. B., Harding, S. G., Carpenter, T. A., Menon, D. K., and Ansorge, R. E. (2010). Quantitative BOLD: The effect of diffusion. *Journal of Magnetic Resonance Imaging*, 32(4):953–61.

Diringer, M. N., Yundt, K., Videen, T. O., Adams, R. E., Zazulia, A. R., Deibert, E., Aiyagari, V., Dacey, R. G., Grubb, R. L., and Powers, W. J. (2000). No reduction in cerebral metabolism as a result of early moderate hyperventilation following severe traumatic brain injury. *Journal of Neurosurgery*, 92(1):7–13.

Domsch, S., Mürle, B., Weingärtner, S., Zapp, J., Wenz, F., and Schad, L. R. (2018). Oxygen extraction fraction mapping at 3 Tesla using an artificial neural network: A feasibility study. *Magnetic Resonance in Medicine*, 79(2):890–899.

Durrant, C. J., Hertzberg, M. P., and Kuchel, P. W. (2003). Magnetic susceptibility: Further insights into macroscopic and microscopic fields and the sphere of Lorentz. *Concepts in Magnetic Resonance Part A*, 18A(1):72–95.

Edelman, R. R., Siewert, B., Darby, D. G., Thangaraj, V., Nobre, A. C., Mesulam, M. M., and Warach, S. (1994). Qualitative mapping of cerebral blood flow and functional localization with echo-planar MR imaging and signal targeting with alternating radio frequency. *Radiology*, 192(2):513–520.

Fan, A. P., Govindarajan, S. T., Kinkel, R. P., Madigan, N. K., Nielsen, a. S., Benner, T., Tinelli, E., Rosen, B. R., Adalsteinsson, E., and Mainero, C. (2014). Quantitative oxygen extraction fraction from 7-Tesla MRI phase: Reproducibility and application in multiple sclerosis. *Journal of Cerebral Blood Flow & Metabolism*, 35(1):131–139.

Farrell, T. J., Wilson, B. C., and Patterson, M. S. (1992). The use of a neural network to determine tissue optical properties from spatially resolved diffuse reflectance measurements. *Physics in Medicine and Biology*, 37(12):2281.

Feinberg, D. A., Hale, J. D., Watts, J. C., Kaufman, L., and Mark, A. (1986). Halving MR imaging time by conjugation: Demonstration at 3.5 kG. *Radiology*, 161(2):527–531.

Feng, X., Deistung, A., and Reichenbach, J. R. (2018). Quantitative susceptibility mapping (QSM) and R2* in the human brain at 3T: Evaluation of intra-scanner repeatability. *Zeitschrift für Medizinische Physik*, 28(1):36–48.

Ferlay, J., Soerjomataram, I., Dikshit, R., Eser, S., Mathers, C., Rebelo, M., Parkin, D. M., Forman, D., and Bray, F. (2015). Cancer incidence and mortality worldwide: Sources, methods and major patterns in GLOBOCAN 2012. *International Journal of Cancer*, 136(5):E359–386.

Furnari, F. B., Fenton, T., Bachoo, R. M., Mukasa, A., Stommel, J. M., Stegh, A., Hahn, W. C., Ligon, K. L., Louis, D. N., Brennan, C., Chin, L., DePinho, R. A., and Cavenee, W. K. (2007). Malignant astrocytic glioma: Genetics, biology, and paths to treatment. *Genes and Development*, 21(21):2683–2710.

Gauthier, C. J. and Hoge, R. D. (2012). Magnetic resonance imaging of resting OEF and CMRO2 using a generalized calibration model for hypercapnia and hyperoxia. *NeuroImage*, 60(2):1212–1225.

Griswold, M. A., Jakob, P. M., Heidemann, R. M., Nittka, M., Jellus, V., Wang, J., Kiefer, B., and Haase, A. (2002). Generalized autocalibrating partially parallel acquisitions (GRAPPA). *Magnetic Resonance in Medicine*, 47(6):1202–1210.

Günther, M., Oshio, K., and Feinberg, D. A. (2005). Single-shot 3D imaging techniques improve arterial spin labeling perfusion measurements. *Magnetic Resonance in Medicine*, 54(2):491–498.

Gusnard, D. A. and Raichle, M. E. (2001). Searching for a baseline: Functional imaging and the resting human brain. *Nature*, 2(10):685–694.

Haacke, E. M., Brown, R. W., Thompson, M. R., and Venkatesan, R. (1999). *Magnetic Resonance Imaging: Physical Principles and Sequence Design*. John Wiley and Sons, Inc., Hoboken, NJ, USA.

Haase, A., Frahm, J., Matthaei, D., Hanicke, W., and Merboldt, K.-D. (1986). FLASH imaging. Rapid NMR imaging using low flip-angle pulses. *Journal of Magnetic Resonance (1969)*, 67(2):258–266.

Hammernik, K., Klatzer, T., Kobler, E., Recht, M. P., Sodickson, D. K., Pock, T., and Knoll, F. (2018). Learning a variational network for reconstruction of accelerated MRI data. *Magnetic Resonance in Medicine*, 79(6):3055–3071.

Hansen, P. C. and O'Leary, D. P. (1993). The use of the L-curve in the regularization of discrete ill-posed problems. *SIAM Journal on Scientific Computing*, 14(6):1487–1503.

Hardee, M. E. and Zagzag, D. (2012). Mechanisms of glioma-associated neovascularization. *The American Journal of Pathology*, 181(4):1126–1141.

He, X. and Yablonskiy, D. A. (2007). Quantitative BOLD: Mapping of human cerebral deoxygenated blood volume and oxygen extraction fraction: Default state. *Magnetic Resonance in Medicine*, 57(1):115–126.

Hernando, D., Vigen, K. K., Shimakawa, A., and Reeder, S. B. (2012). R2* mapping in the presence of macroscopic Bo field variations. *Magnetic Resonance in Medicine*, 68(3):830–840.

Herscovitch, P. and Raichle, M. E. (1985). What is the correct value for the brain-blood partition coefficient for water? *Journal of Cerebral Blood Flow & Metabolism*, 5(1):65–69.

Hockel, M., Schlenger, K., Mitze, M., Schaffer, U., and Vaupel, P. (1996). Hypoxia and radiation response in human tumors. *Seminars in Radiation Oncology*, 6(1):3–9.

Hornik, K. (1991). Approximation capabilities of multilayer feedforward networks. *Neural Networks*, 4(2):251–257.

Hu, B. Y.-K. (2000). Averages of static electric and magnetic fields over a spherical region: A derivation based on the mean-value theorem. *American Journal of Physics*, 68(11):1058.

Hubertus, S., Thomas, S., Cho, J., Zhang, S., Kovanlikaya, I., Wang, Y., and Schad, L. R. (2019a). MRI-based oxygen extraction fraction and cerebral metabolic rate of oxygen mapping in high-grade glioma using a combined quantitative susceptibility mapping and quantitative blood oxygenation level-dependent approach. In *Proceedings of International Society for Magnetic Resonance in Medicine*, volume 27, page 0391, Montréal, Canada.

Hubertus, S., Thomas, S., Cho, J., Zhang, S., Wang, Y., and Schad, L. R. (2019b). Comparison of gradient echo and gradient echo sampling of spin echo sequence for the quantification of the oxygen extraction fraction from a combined quantitative susceptibility mapping and quantitative BOLD (QSM+qBOLD) approach. *Magnetic Resonance in Medicine*. https://doi.org/10.1002/mrm.27804.

Hubertus, S., Thomas, S., Cho, J., Zhang, S., Wang, Y., and Schad, L. R. (2019c). Using an artificial neural network for fast mapping of the oxygen extraction fraction with combined QSM and quantitative BOLD. *Magnetic Resonance in Medicine*. https://doi.org/10.1002/mrm.27882.

Ibaraki, M., Shimosegawa, E., Miura, S., Takahashi, K., Ito, H., Kanno, I., and Hatazawa, J. (2004). PET measurements of CBF, OEF, and CMRO2 without arterial sampling in hyperacute ischemic stroke: Method and error analysis. *Annals of Nuclear Medicine*, 18(1):35–44.

Ingrisch, M. and Sourbron, S. (2013). Tracer-kinetic modeling of dynamic contrast-enhanced MRI and CT: A primer. *Journal of Pharmacokinetics and Pharmacodynamics*, 40(3):281–300.

Ito, H., Kanno, I., Kato, C., Sasaki, T., Ishii, K., Ouchi, Y., and Iida, A. (2004). Database of normal human cerebral blood flow, cerebral blood volume, cerebral oxygen extraction fraction and cerebral metabolic rate of oxygen measured by positron emission tomography with 15 O-labelled carbon dioxide or water, carbon monoxide and oxygen: A multicentre study in Japan. *European Journal of Nuclear Medicine and Molecular Imaging*, 31(5):635–643.

Jain, V., Abdulmalik, O., Propert, K. J., and Wehrli, F. W. (2012). Investigating the magnetic susceptibility properties of fresh human blood for noninvasive oxygen saturation quantification. *Magnetic Resonance in Medicine*, 68(3):863–867.

Keil, V. C., Madler, B., Gieseke, J., Fimmers, R., Hattingen, E., Schild, H. H., and Hadizadeh, D. R. (2017). Effects of arterial input function selection on kinetic parameters in brain dynamic contrast-enhanced MRI. *Magnetic Resonance Imaging*, 40:83–90.

Kressler, B., De Rochefort, L., Liu, T., Spincemaille, P., Jiang, Q., and Wang, Y. (2010). Nonlinear regularization for per voxel estimation of magnetic susceptibility distributions from MRI field maps. *IEEE Transactions on Medical Imaging*, 29(2):273–281.

Kudo, K., Liu, T., Murakami, T., Goodwin, J., Uwano, I., Yamashita, F., Higuchi, S., Wang, Y., Ogasawara, K., Ogawa, A., and Sasaki, M. (2016). Oxygen extraction fraction measurement using quantitative susceptibility mapping: Comparison with positron emission tomography. *Journal of Cerebral Blood Flow & Metabolism*, 36(8):1424–1433.

Kwong, K. K., Belliveau, J. W., Chesler, D. A., Goldberg, I. E., Weisskoff, R. M., Poncelet, B. P., Kennedy, D. N., Hoppel, B. E., Cohen, M. S., and Turner, R. (1992). Dynamic magnetic resonance imaging of human brain activity during primary sensory stimulation. *Proceedings of the National Academy of Sciences of the USA*, 89(12):5675–5679.

Lakhani, P. and Sundaram, B. (2017). Deep learning at chest radiography: Automated classification of pulmonary tuberculosis by using convolutional neural networks. *Radiology*, 284(2):574–582.

Langkammer, C., Schweser, F., Krebs, N., Deistung, A., Goessler, W., Scheurer, E., Sommer, K., Reishofer, G., Yen, K., Fazekas, F., Ropele, S., and Reichenbach, J. R. (2012). Quantitative susceptibility mapping (QSM) as a means to measure brain iron? A post mortem validation study. *NeuroImage*, 62(3):1593–1599.

Leenders, K. L., Perani, D., Lammertsma, A. A., Heather, J. D., Buckingham, P., Healy, M. J., Gibbs, J. M., Wise, R. J., Hatazawa, J., Herold, S., Beaney, R. P., Brooks, D. J., Spinks, T., Rhodes, C., Frackowiak, R. S. J., and Jones, T. (1990). Cerebral blood flow, blood volume and oxygen utilization. Normal values and effect of age. *Brain*, 113(1):27–47.

Liu, F., Zhou, Z., Jang, H., Samsonov, A., Zhao, G., and Kijowski, R. (2018). Deep convolutional neural network and 3D deformable approach for tissue segmentation in musculoskeletal magnetic resonance imaging. *Magnetic Resonance in Medicine*, 79(4):2379–2391.

Liu, J., Liu, T., De Rochefort, L., Ledoux, J., Khalidov, I., Chen, W., Tsiouris, A. J., Wisnieff, C., Spincemaille, P., Prince, M. R., and Wang, Y. (2012). Morphology enabled dipole inversion for quantitative susceptibility mapping using structural consistency between the magnitude image and the susceptibility map. *NeuroImage*, 59(3):2560–2568.

Liu, T., Khalidov, I., de Rochefort, L., Spincemaille, P., Liu, J., Tsiouris, A. J., and Wang, Y. (2011). A novel background field removal method for MRI using projection onto dipole fields (PDF). *NMR in Biomedicine*, 24(9):1129–1136.

Liu, T., Spincemaille, P., De Rochefort, L., Kressler, B., and Wang, Y. (2009). Calculation of susceptibility through multiple orientation sampling (cosmos): A method for conditioning the inverse problem from measured magnetic field map to susceptibility source image in MRI. *Magnetic Resonance in Medicine*, 61(1):196–204.

Liu, T., Wisnieff, C., Lou, M., Chen, W., Spincemaille, P., and Wang, Y. (2013). Nonlinear formulation of the magnetic field to source relationship for robust quantitative susceptibility mapping. *Magnetic Resonance in Medicine*, 69(2):467–476.

Louis, D. N., Ohgaki, H., Wiestler, O. D., Cavenee, W. K., Burger, P. C., Jouvet, A., Scheithauer, B. W., and Kleihues, P. (2007). The 2007 WHO classification of tumours of the central nervous system. *Acta Neuropathologica*, 114(2):97–109.

Louis, D. N., Perry, A., Reifenberger, G., von Deimling, A., Figarella-Branger, D., Cavenee, W. K., Ohgaki, H., Wiestler, O. D., Kleihues, P., and Ellison, D. W. (2016). The 2016 world health organization classification of tumors of the central nervous system: A summary. *Acta Neuropathologica*, 131(6):803–820.

Lu, H., Clingman, C., Golay, X., and van Zijl, P. C. M. (2004). Determining the longitudinal relaxation time (T1) of blood at 3.0 Tesla. *Magnetic Resonance in Medicine*, 52(3):679–682.

Lundervold, A. S. and Lundervold, A. (2019). An overview of deep learning in medical imaging focusing on MRI. *Zeitschrift für Medizinische Physik*, 29(2):102–127.

Maier, A., Syben, C., Lasser, T., and Riess, C. (2019). A gentle introduction to deep learning in medical image processing. *Zeitschrift für Medizinische Physik*, 29(2):86–101.

Mugler III, J. P. and Brookeman, J. R. (1990). Three-dimensional magnetization-prepared rapid gradient-echo imaging (3D MP RAGE). *Magnetic Resonance in Medicine*, 15(1):152–157.

Nasrabadi, N. M. (2007). Pattern recognition and machine learning. *Journal of Electronic Imaging*, 16(4).

Ostrom, Q. T., Gittleman, H., Liao, P., Vecchione-Koval, T., Wolinsky, Y., Kruchko, C., and Barnholtz-Sloan, J. S. (2017). CBTRUS statistical report: Primary brain and other central nervous system tumors diagnosed in the United States in 2010–2014. *Neuro-Oncology*, 19(suppl_5):v1–v88.

Pelleg, D. and Moore, A. (2000). X-means: Extending k-means with efficient estimation of the number of clusters. In *Proceedings of the 17th International Conference on Machine Learning*, pages 727–734.

Preibisch, C., Shi, K., Kluge, A., Lukas, M., Wiestler, B., Göttler, J., Gempt, J., Ringel, F., Al Jaberi, M., Schlegel, J., Meyer, B., Zimmer, C., Pyka, T., and Förster, S. (2017). Characterizing hypoxia in human glioma: A simultaneous multimodal MRI and PET study. *NMR in Biomedicine*, 30(11):e3775.

Purcell, E. M., Torrey, H. C., and Pound, R. V. (1946). Resonance absorption by nuclear magnetic moments in a solid. *Physical Review*, 69(1-2):37–38.

Ramalho, J., Semelka, R., Ramalho, M., Nunes, R., AlObaidy, M., and Castillo, M. (2016). Gadolinium-based contrast agent accumulation and toxicity: An update. *American Journal of Neuroradiology*, 37(7):1192–1198.

Robinson, S. D., Bredies, K., Khabipova, D., Dymerska, B., Marques, J. P., and Schweser, F. (2017). An illustrated comparison of processing methods for MR phase imaging and QSM: Combining array coil signals and phase unwrapping. *NMR in Biomedicine*, 30(4):e3601.

Rodgers, Z. B., Leinwand, S. E., Keenan, B. T., Kini, L. G., Schwab, R. J., and Wehrli, F. W. (2016). Cerebral metabolic rate of oxygen in obstructive sleep apnea at rest and in response to breath-hold challenge. *Journal of Cerebral Blood Flow & Metabolism*, 36(4):755–767.

Rofstad, E. K., Sundfør, K., Lyng, H., and Tropé, C. G. (2000). Hypoxia-induced treatment failure in advanced squamous cell carcinoma of the uterine cervix is primarily due to hypoxia-induced radiation resistance rather than hypoxia-induced metastasis. *British Journal of Cancer*, 83(3):354–359.

Sakai, F., Nakazawa, K., Tazaki, Y., Ishii, K., Hino, H., Igarashi, H., and Kanda, T. (1985). Regional cerebral blood volume and hematocrit measured in normal human volunteers by single-photon emission computed tomography. *Journal of Cerebral Blood Flow & Metabolism*, 5(2):207–213.

Savicki, J. P., Lang, G., and Ikeda-Saito, M. (1984). Magnetic susceptibility of oxy- and carbonmonoxyhemoglobins. *Proceedings of the National Academy of Sciences of the USA*, 81(17):5417–5419.

Schenck, J. F. (1996). The role of magnetic susceptibility in magnetic resonance imaging: MRI magnetic compatibility of the first and second kinds. *Medical Physics*, 23(6):815–850.

Schmidt, M. (2008). minConf: Projection methods for optimization with simple constraints in Matlab. `http://www.cs.ubc.ca/~schmidtm/Software/minConf.html`. Accessed: September 8, 2018.

Schmidt, M., Berg, E., Friedlander, M., and Murphy, K. (2009). Optimizing costly functions with simple constraints: A limited-memory projected quasi-Newton algorithm. In *Proceedings of the Twelth International Conference*

on Artificial Intelligence and Statistics, volume 5, pages 456–463, Clearwater Beach, FL, USA.

Schnurr, A.-K., Chung, K., Russ, T., Schad, L. R., and Zöllner, F. G. (2019). Simulation-based deep artifact correction with convolutional neural networks for limited angle artifacts. *Zeitschrift für Medizinische Physik*, 29(2):150–161.

Schofield, M. a. and Zhu, Y. (2003). Fast phase unwrapping algorithm for interferometric applications. *Optics Letters*, 28(14):1194–1196.

Schweser, F., Deistung, A., and Reichenbach, J. R. (2016). Foundations of MRI phase imaging and processing for quantitative susceptibility mapping (QSM). *Zeitschrift für Medizinische Physik*, 26(1):6–34.

Shen, Y., Goerner, F. L., Snyder, C., Morelli, J. N., Hao, D., Hu, D., Li, X., and Runge, V. M. (2015). T1 relaxivities of gadolinium-based magnetic resonance contrast agents in human whole blood at 1.5, 3, and 7T. *Investigative Radiology*, 50(5):330–338.

Smith, S. M. (2002). Fast robust automated brain extraction. *Human Brain Mapping*, 17(3):143–155.

Sourbron, S. P. and Buckley, D. L. (2011). Tracer kinetic modelling in MRI: Estimating perfusion and capillary permeability. *Physics in Medicine and Biology*, 57(2):R1–R33.

Spees, W. M. W., Yablonskiy, D. A. D., Oswood, M. C., and Ackerman, J. J. H. (2001). Water proton MR properties of human blood at 1.5 Tesla: Magnetic susceptibility, T1, T2, T2*, and non Lorentzian signal behavior. *Magnetic Resonance in Medicine*, 45(4):533–542.

Stadlbauer, A., Zimmermann, M., Kitzwogerer, M., Oberndorfer, S., Rossler, K., Dorfler, A., Buchfelder, M., and Heinz, G. (2017). MR imaging-derived oxygen metabolism and neovascularization characterization for grading and IDH gene mutation detection of gliomas. *Radiology*, 283(3):799–809.

Stewart, B. W. and Wild, C. P. (2014). *World Cancer Report 2014*. International Agency for Research on Cancer, WHO.

Strickland, M. and Stoll, E. A. (2017). Metabolic reprogramming in glioma. *Frontiers in Cell and Developmental Biology*, 5:43.

Sukstanskii, A. L. and Yablonskiy, D. A. (2001). Theory of FID NMR signal dephasing induced by mesoscopic magnetic field inhomogeneities in biological systems. *Journal of Magnetic Resonance*, 151(1):107–117.

Søvik, A., Malinen, E., and Olsen, D. R. (2009). Strategies for biologic image-guided dose escalation: A review. *International Journal of Radiation Oncology*Biology*Physics*, 73(3):650–658.

Ulrich, X. and Yablonskiy, D. A. (2016). Separation of cellular and BOLD contributions to T2* signal relaxation. *Magnetic Resonance in Medicine*, 75(2):606–615.

Vaupel, P. and Mayer, A. (2007). Hypoxia in cancer: Significance and impact on clinical outcome. *Cancer and Metastasis Reviews*, 26(2):225–39.

von Samson-Himmelstjerna, F., Madai, V. I., Sobesky, J., and Günther, M. (2016). Walsh-ordered Hadamard time-encoded pseudocontinuous ASL (WH pCASL). *Magnetic Resonance in Medicine*, 76(6):1814–1824.

Wang, J. Z., Li, X. A., and Mayr, N. A. (2006). Dose escalation to combat hypoxia in prostate cancer: A radiobiological study on clinical data. *The British Journal of Radiology*, 79(947):905–911.

Wang, Y. and Liu, T. (2015). Quantitative susceptibility mapping (QSM): Decoding MRI data for a tissue magnetic biomarker. *Magnetic Resonance in Medicine*, 73(1):82–101.

Weisskoff, R. M. and Kiihne, S. (1992). MRI susceptometry: Image-based measurement of absolute susceptibility of MR contrast agents and human blood. *Magnetic Resonance in Medicine*, 24(2):375–383.

Wells, J. A., Lythgoe, M. F., Gadian, D. G., Ordidge, R. J., and Thomas, D. L. (2010). In vivo Hadamard encoded continuous arterial spin labeling (H-CASL). *Magnetic Resonance in Medicine*, 63(4):1111–1118.

Wen, P. Y. and Kesari, S. (2008). Malignant gliomas in adults. *New England Journal of Medicine*, 359(5):492–507.

Whittall, K. P., MacKay, A. L., Graeb, D. A., Nugent, R. A., Li, D. K., and Paty, D. W. (1997). In vivo measurement of T2 distributions and water contents in normal human brain. *Magnetic Resonance in Medicine*, 37(1):34–43.

Williams, D. S., Detre, J. A., Leigh, J. S., and Koretsky, A. P. (1992). Magnetic resonance imaging of perfusion using spin inversion of arterial water. *Proceedings of the National Academy of Sciences of the USA*, 89(1):212–216.

Wise, R. G., Harris, A. D., Stone, A. J., and Murphy, K. (2013). Measurement of OEF and absolute CMRO2: MRI-based methods using interleaved and combined hypercapnia and hyperoxia. *NeuroImage*, 83:135–147.

Wisnieff, C., Ramanan, S., Olesik, J., Gauthier, S., Wang, Y., and Pitt, D. (2015). Quantitative susceptibility mapping (QSM) of white matter multiple sclerosis lesions: Interpreting positive susceptibility and the presence of iron. *Magnetic Resonance in Medicine*, 74(2):564–570.

Wu, W.-C., Fernández-Seara, M., Detre, J. A., Wehrli, F. W., and Wang, J. (2007). A theoretical and experimental investigation of the tagging efficiency of pseudocontinuous arterial spin labeling. *Magnetic Resonance in Medicine*, 58(5):1020–1027.

Yablonskiy, D. A. (1998). Quantitation of intrinsic magnetic susceptibility-related effects in a tissue matrix. Phantom study. *Magnetic Resonance in Medicine*, 39(3):417–428.

Yablonskiy, D. A. and Haacke, E. M. (1994). Theory of NMR signal behavior in magnetically inhomogeneous tissues: The static dephasing regime. *Magnetic Resonance in Medicine*, 32(6):749–763.

Yablonskiy, D. A. and Haacke, E. M. (1997). An MRI method for measuring T2 in the presence of static and rf magnetic field inhomogeneities. *Magnetic Resonance in Medicine*, 37(6):872–876.

Yablonskiy, D. A., Sukstanskii, A. L., and He, X. (2013). Blood oxygenation level-dependent (BOLD)-based techniques for the quantification of brain hemodynamic and metabolic properties - theoretical models and experimental approaches. *NMR in Biomedicine*, 26(8):963–986.

Yamauchi, H., Fukuyama, H., Nagahama, Y., Nabatame, H., and Shio, H. (1999). Cerebral hemodynamics and risk for recurrent stroke in symptomatic internal carotid artery occlusion. *Rinsho Shinkeigaku = Clinical Neurology*, 39(5):513–519.

Yoon, J., Gong, E., Chatnuntawech, I., Bilgic, B., Lee, J., Jung, W., Ko, J., Jung, H., Setsompop, K., Zaharchuk, G., Kim, E. Y., Pauly, J., and Lee, J. (2018). Quantitative susceptibility mapping using deep neural network: QSMnet. *NeuroImage*, 179:199–206.

Young, G. S. (2007). Advanced MRI of adult brain tumors. *Neurologic Clinics*, 25(4):947–973.

Zhang, J., Cho, J., Zhou, D., Nguyen, T. D., Spincemaille, P., Gupta, A., and Wang, Y. (2018). Quantitative susceptibility mapping-based cerebral metabolic rate of oxygen mapping with minimum local variance. *Magnetic Resonance in Medicine*, 79(1):172–179.

Zhang, J., Liu, T., Gupta, A., Spincemaille, P., Nguyen, T. D., and Wang, Y. (2015). Quantitative mapping of cerebral metabolic rate of oxygen (CMRO2) using quantitative susceptibility mapping (QSM). *Magnetic Resonance in Medicine*, 74(4):945–952.

Zhang, J., Zhou, D., Nguyen, T. D., Spincemaille, P., Gupta, A., and Wang, Y. (2017). Cerebral metabolic rate of oxygen (CMRO2) mapping with hyperventilation challenge using quantitative susceptibility mapping (QSM). *Magnetic Resonance in Medicine*, 77(5):1762–1773.

Zheng, W., Nichol, H., Liu, S., Cheng, Y.-C. N., and Haacke, E. M. (2013). Measuring iron in the brain using quantitative susceptibility mapping and X-ray fluorescence imaging. *NeuroImage*, 78:68–74.

Zhou, D., Liu, T., Spincemaille, P., and Wang, Y. (2014). Background field removal by solving the laplacian boundary value problem. *NMR in Biomedicine*, 27(3):312–319.

Zöllner, F. G., Emblem, K. E., and Schad, L. R. (2010). Support vector machines in DSC-based glioma imaging: suggestions for optimal characterization. *Magnetic Resonance in Medicine*, 64(4):1230–1236.

Zubal, I. G., Harrell, C. R., Smith, E. O., Rattner, Z., Gindi, G., and Hoffer, P. B. (1994). Computerized three-dimensional segmented human anatomy. *Medical Physics*, 21(2):299–302.